Universidad de Cádiz

Departamento de Ciencia de los Materiales
e Ingeniería Metalúrgica y Química Inorgánica

Nanoscale characterization of InSb/InAs novel functional semiconductor nanostructures for LEDs

Caracterización a nanoescala de nanoestructuras funcionales novedosas de InSb/InAs para LEDs

Atif Alam Khan

A Thesis submitted for the degree of Doctor

Universidad de Cádiz

Departamento de Ciencia de los Materiales
e Ingeniería Metalúrgica y Química Inorgánica

Nanoscale characterization of InSb/InAs novel functional semiconductor nanostructures for LEDs

Caracterización a nanoescala de nanoestructuras funcionales novedosas de InSb/InAs para LEDs

Atif Alam Khan

Supervisors:

Prof. Dr. Sergio Ignacio Molina Rubio

Catedrático de Universidad
Departamento de Ciencia de los Materiales e Ingeniería Metalúrgica y Química Inorgánica

Dr. Miriam Herrera Collado

Profesora Titular de Universidad
Departamento de Ciencia de los Materiales e Ingeniería Metalúrgica y Química Inorgánica

Departamento de Ciencia de los Materiales
e Ingeniería Metalúrgica y Química Inorgánica

Tribunal de tesis

Presidente: **Prof. Dr. Carlos Algora del Valle**

Catedrático de Universidad
Instituto de Energía Solar
Universidad Politécnica de Madrid

Secretario: **Dr. David Sales Lérida**

Profesor Titular de Universidad
Departamento de Ciencia de los Materiales
e Ingeniería Metalúrgica y Química Inorgánica
Universidad de Cádiz

Vocal: **Prof. Dr. Fernando B. Naranjo Vega**

Catedrático de Universidad
Departamento de Electrónica
Universidad de Alcalá

As the supervisors, Prof. Dr. Sergio Ignacio Molina Rubio and Associate Prof. Dr. Miriam Herrera Collado, from the Area of Materials Science and Metallurgical Engineering in the University of Cádiz AUTHORIZE the presentation of the Doctoral Thesis of Atif Alam Khan, entitled *Nanoscale Characterization of InSb/InAs novel functional semiconductor nanostructures for LEDs.*

El Prof. Dr. Sergio Ignacio Molina Rubio, Catedrático de Universidad del Área de Conocimiento de Ciencia de los Materiales e Ingeniería Metalúrgica, y la Dra. Miriam Herrera Collado, Profesora Titular de Universidad de la misma Área de Conocimiento, en calidad de Directores, AUTORIZAN la presentación a trámite de la Tesis Doctoral de Atif Alam Khan titulada *Caracterización a nanoescala de nanoestructuras funcionales novedosas de InSb/InAs para LEDs.*

Puerto Real, November 11, 2019

V^{o}. B^{o}.

Dr. Sergio Ignacio Molina Rubio

Dr. Miriam Herrera Collado

উৎসর্গ:

আমার প্রিয় পরিবার, আমার অনুপ্রেরণা

Acknowledgements

First of all, I would like to express my gratitudes to my PhD supervisors in the University of Cádiz (UCA), Prof. Dr. Sergio I. Molina, the head of the research group of INNANOMAT (*Materials and Nanotechnology for Innovation*) for selecting me as an early stage researcher (ESR) in the European Union (EU) supported prestigious Horizon 2020 Marie-Sklodowska Curie ITN (*Initial training network*) associated PROMIS (*Postgraduate research on dilute metamorphic nanostructures and metamaterials in semiconductor photonics*) network and Dr. Miriam Herrera for guiding me in every step in this Doctoral Program. I really appreciate all the supports and helps they have provided me to persevere in the field of Nanomaterials research.

Sincere thanks to all of my current and former colleagues from UCA: Jesús, Natalia, Fran, Relinque, María, Fernando, Juan Jesús and Otman for helping me in every aspect throughout my PhD years. My heartfelt gratitude to Dani and Vero for their valuable guidances and suggestions whenever I had faced difficulties. I would also like to mention other PROMIS ESRs: Eva, Denise, Julie, Stefano, Davide, Lucas, Mayank, Shalini, Salman, Mario, Flavio, Shumithira, Saeed, Emna and Reza for their great supports and friendship all along the PROMIS years.

Special thanks to PROMIS coordinator Prof. Dr. Anthony Krier, PROMIS administrator Pamela Forster and as well as, Susan Krier from Lancaster University (UK) for assisting me throughout the PROMIS project and all the people in Prof. Krier's group during my research stay in Lancaster. I would also like to express my gratitude to Prof. Dr. Eric Tournié and his group in University of Montpellier (France) for their great supports during my research stay in Montpellier.

I would like to acknowledge the contribution of following institutions for the successful completion of this Doctoral Thesis:

- EU PROMIS Horizon 2020 ITN project with Grant agreement no. 641899.
- The Spanish MINECO (projects TEC2014-53727-C2-2-R and TEC2017-86102-C2-2-R) and the Junta de Andalucía (PAI research groups TEP-946

INNANOMAT and TIC-145). Co-financing from UE-FEDER is also acknowledged.

- The Institute of Electron Microscopy and Materials (IMEyMAT) and the Electron Microscopy Division of the Scientific and Technological Research Central Services (SC-ICYT) in UCA.

Finally, special thanks to my parents, brother, sister-in-law, nephew and nieces for their continuous encouragement that kept me focused during my Doctoral degree.

The present Doctoral Thesis entitled *Nanoscale characterization of InSb/InAs novel functional semiconductor nanostructures for LEDs (Caracterización a nanoescala de nanoestructuras funcionales novedosas de InSb/InAs para LEDs)* fulfills all the requirements to obtain the PhD title under the modality of *Thesis by Compendium of Publications* regulated by the regulations of UCA/CG06/2012, June 27, 2012.

The compendium of publications of this Thesis is constituted by the following articles:

1. Atif A. Khan, M. Herrera, J. Pizarro, P. L. Galindo, P. J. Carrington, H. Fujita, A. Krier, S. I. Molina. *Modified qHAADF method for atomic column-by-column compositional quantification of semiconductor heterostructures,* Journal of Materials Science 54: 3230 (2019).

2. Atif A. Khan, M. Herrera, N. Fernández-Delgado, D. F. Reyes, J. Pizarro, E. Repiso, A. Krier, S. I. Molina. *Investigation on Sb distribution for InSb/InAs sub-monolayer heterostructure using TEM techniques,* Nanotechnology 31: 025706 (2020).

3. Atif A. Khan, E. Repiso, M. Herrera, P. J. Carrington, M. de la Mata, J. Pizarro, A. Krier, S. I. Molina. *Effect of the cap layer growth temperature on the Sb distribution in InAs/InSb/InAs sub-monolayer heterostructures for mid-infrared devices,* accepted in Nanotechnology 31:105702 (2020).

The format used in the present Doctoral Thesis is in agreement with the indications published in the item 6 of the article 23 of the regulations of UCA/CG06/2012, where the following chapters are required: a) Abstract, b) Introduction and Justification of the theme of the Thesis, c) Hypotheses and Objectives, d) Critical analysis of the state of the art, e) Joint discussion of the results analyzed in various articles, f) Conclusions and g) Prospects. The corresponding references and the appendices which contain information of the participated congresses/workshops during this PhD and the corroborating publications of this Thesis have been added at the end of the manuscript.

List of Acronyms

Acronyms	Descriptions
0D	0-dimensional
1D	1-dimensional
2D	2-dimensional
3D	3-dimensional
BW	Bandwidth
CB	Conduction band
CC	Cold cap
CD	Compact Disk
CE	Conventional epitaxy
CFL	Compact fluorescent lights
CTEM	Conventional transmission electron microscopy
CW	Continuous-wave
DF	Dark field
DOS	Density of states
DVD	Digital versatile disk
EDX	Energy-dispersive X-ray
EELS	Electron energy loss spectroscopy

EL	Electroluminescence
EQE	External quantum efficiency
FEG	Field-emission gun
FFT	Fast Fourier transform
FIB	Focused ion beam
Gbps	Gigabits per second
GI	Growth interruption
GPA	Geometrical phase analysis
HAADF-STEM	High angle annular dark field – Scanning transmission electron microscopy
HRTEM	High resolution transmission electron microscopy
ITN	Initial training network
IQE	Internal quantum efficiency
LED	Light emitting diode
Li-Fi	Light fidelity
LPE	Liquid-phase epitaxy
LT	Low temperature
MBE	Molecular beam epitaxy
MEE	Migration enhanced epitaxy

Mbps	Megabits per second
MIR	Mid infrared
ML	Monolayer
MONITOR	Methane observation networks with innovative technology to obtain reductions
MOVPE	Metal-organic vapor-phase epitaxy
PL	Photoluminescence
PPA	Peak pairs analysis
PROMIS	Postgraduate research on dilute metamorphic nanostructures and metamaterials in semiconductor photonics
Qbits	Quantum bits
QCL	Quantum-cascade laser
QD	Quantum dot
QDIP	Quantum dot infrared photodetector
qHAADF	Quantitative high angle annular dark field
QW	Quantum well
QWire	Quantum wire
RHEED	Reflection high-energy electron diffraction
ROI	Region of interest

RT	Room temperatura
SAE	Selective area epitaxy
SK	Stranski-Krastanov
SL	Superlattice
SML	Sub-monolayer
TEM	Transmission electron microscopy
VB	Valence band
VOC	Volatile organic compounds
Wi-Fi	Wireless fidelity
WL	Wetting layer
ZLP	Zero-loss peak

Abstract

Light emitting diodes (LEDs) are becoming increasingly popular day-by-day for lighting applications as they require low maintenance and low fabrication costs, and have long lifetime and low energy consumption. As a result, extensive research and funding have been dedicated in the last years in order to obtain superior LED fabrication techniques and designs which may maximize their optical performances. III-V epitaxial quantum dots (QDs) have been considered to design the active layers of these LEDs as these QDs offer the highest level of optoelectronic efficiency. Among various III-V epitaxial QDs, InSb/InAs QDs emit light at the mid-infrared (MIR) range (3-5 μm) through the tuning of Sb composition and as a result, these QDs can be used to detect various hazardous gases with MIR signatures, among other applications. In this framework, the objective of the present Thesis is to explore the applicability of the migration enhanced epitaxy (MEE) growth technique to fabricate these InSb/InAs QDs, as an alternative to the conventional Stranski-Krastranov (SK) QDs, in order to configure optimum design parameters for highly efficient gas and bio-sensing LEDs at MIR range.

The optoelectronic properties of the MEE grown InSb/InAs QDs highly depend on corresponding Sb distribution. Because of this, atomic column resolved high angle annular dark field (HAADF) – scanning transmission electron microscopy (STEM) characterization technique has been considered, where Sb compositions are realized through HAADF-STEM atomic column intensities. In order to interpret the Sb composition through HAADF-STEM intensities, the quantitative HAADF (qHAADF) method can be used that quantifies Sb induced intensity through the intensity ratio of a Sb-containing region to a Sb-absent region. However, this tool requires both regions to be present in the same micrograph. As a result, the application of this tool becomes limited if InSb/InAs QDs exist in a complex heterostructure where locating a reference area is complicated. Consequently, a modified version of the qHAADF tool has been developed in this Thesis that allows locating the reference region from a second micrograph and hence, the aforementioned limitation could be overcome. The specimen thickness variation between these two areas imposes complications in the Sb compositional analysis by the either qHAADF tool. Therefore, a corresponding thickness

variation compensation process has also been discussed in this Thesis to assure atomic column resolved precise Sb compositional analysis.

The MEE grown InSb/InAs QDs associated to sub-monolayer (SML) insertion of InSb may offer increased maximum gain and a larger modulation bandwidth (BW) than its conventional SK counterpart as these QDs are surrounded by a thin/no wetting layer (WL) underneath. However, it has been demonstrated through this PhD Thesis that a high growth temperature facilitates a high Sb segregation into the InAs capping layer. As a result, continuous InSbAs WL form with nm thickness encapsulating a few random InSbAs agglomerates, realized through the corresponding HAADF-STEM and 002 dark field (DF) conventional TEM (CTEM) analyses. The corresponding high Sb segregation seems to induce relatively low average Sb composition in the InSbAs agglomerates.

Typically, Sb segregation from InSb/InAs heterostructures is reduced by decreasing the corresponding growth temperature. However, this PhD Thesis illustrates that Sb segregation can also be reduced from the MEE grown InSb/InAs heterostructures by reducing only InAs cap growth temperature. This results in an increase in Sb composition in the InSbAs agglomerates observed through both HAADF-STEM and 002 DF CTEM analyses. As a result, the random InSbAs agglomerates become bigger or more continuous within the InSbAs WLs. This InAs cap temperature associated compositional variation in Sb composition allows tuning the InSb emission wavelength in the MIR range, realized through the corresponding photoluminescence (PL) emission spectra.

Resumen

Los diodos emisores de luz (LEDs) son cada vez más populares para aplicaciones relacionadas con la iluminación debido a que requieren poco mantenimiento, un bajo consumo de energía y bajos costes de fabricación, y a que tienen un largo tiempo de vida. Debido a esto, en los últimos años se han dedicado crecientes esfuerzos de investigación y económicos para obtener técnicas de fabricación de LEDs y diseños mejorados que maximicen su funcionalidad óptica. Los puntos cuánticos (QDs) epitaxiales III-V se han utilizado para diseñar las capas activas de estos LEDs debido a que ofrecen una alta eficiencia en aplicaciones optoelectrónicas. De entre los varios tipos de QDs epitaxiales III-V, los QDs de InSb/InAs pueden emiten luz en el rango del infra-rojo medio (MIR) (3-5 μm) mediante la modificación en su composición en Sb y, gracias a esto, se pueden utilizar para detectar gases peligrosos en el rango MIR, entre otras aplicaciones. En este marco, el objetivo de la presente Tesis consiste en explorar la aplicabilidad de la técnica de crecimiento *epitaxia por migración mejorada* (MEE) para fabricar estos QDs de InSb/InAs, como alternativa a los QDs obtenidos por crecimiento Stranski-Krastanov (SK), para configurar parámetros de diseño óptimos para obtener LEDs con aplicaciones en sensores de gases en el rango MIR.

Las propiedades optoelectrónicas de los QDs de InSb/InAs crecidos por MEE dependen, en gran medida, de la distribución de Sb en el material. Para analizar dicha distribución de Sb, en esta Tesis se ha utilizado la técnica de microscopía electrónica de transmisión en modo barrido (STEM) utilizando el detector anular de alto ángulo en campo oscuro (HAADF), ya que permite cuantificar la composición a través de la relación de intensidades de regiones que contienen Sb respecto a regiones de referencia sin Sb. Sin embargo, esta herramienta requiere que ambas regiones estén presentes en la misma micrografía. Debido a esto, la aplicación de esta herramienta se ve limitada si los QDs de InSb/InAs existen en heteroestructuras complejas donde encontrar una región de referencia sea complicada. Para solucionar esta limitación, en la presente Tesis se ha desarrollado una versión modificada del qHAADF que permite seleccionar la región de referencia en una micrografía diferente. Sin embargo, la variación de espesor entre estas dos regiones tiene un gran efecto en el análisis de la composición mediante esta técnica. Debido a esto, en la

presente Tesis se incluye un proceso de compensación de las variaciones de espesor para asegurar un análisis de la composición en Sb con resolución atómica más preciso.

Los QDs de InSb/InAs crecidos mediante MEE por deposición de sub-monocapas (SML) de InSb podrían ofrecer mejor ganancia máxima y un ancho de banda de modulación (BW) mayor que los obtenidos mediante crecimiento SK, ya que podrían no estar rodeados de la típica capa de mojado (WL) presente en QDs SK. Sin embargo, en la presente Tesis Doctoral se demuestra que una alta temperatura de crecimiento durante el proceso MEE produce la segregación del Sb en estas estructuras hacia la capa de recubrimiento de InAs. Debido a esto, se forma una capa continua de InSbAs con espesor de pocos nanómetros que rodea algunos aglomerados de InSbAs, como se ha observado mediante HAADF-STEM y por contraste de difracción 002 en campo oscuro (DF). La alta segregación de Sb observada parece introducir una composición de Sb relativamente baja en los aglomerados.

En general, la segregación de Sb en heteroestructuras de InSb/InAs se reduce mediante la reducción en la temperatura de crecimiento de las capas activas. Sin embargo, en la presente Tesis se muestra que la segregación de Sb en heteroestructuras InSb/InAs crecidas mediante MEE también se puede reducir disminuyendo la temperatura de la capa de recubrimiento de InAs. Esto produce un aumento en la composición de Sb en los aglomerados de InSbAs, como se ha observado mediante HAADF-STEM y 002 DF. Como resultado, los aglomerados de InSbAs aumentan de tamaño y/o aparecen de manera más continua en la WL de InSbAs. Esta variación de composición en Sb asociada a la variación en la temperatura de crecimiento de la capa de recubrimiento permite modificar la longitud de onda de emisión del InSb en el rango MIR, como se ha observado mediante el análisis por fotoluminescencia (PL).

Index

Chapter 1

Introduction and Justification of the theme of the Thesis

Semiconductors have revolutionized our current way of life through the developments in the fields of renewable energy, medical applications, modern communication, electronics and optoelectronic devices. Among various semiconductors, III-V semiconductors and their ternary and quaternary alloys generally possess direct band gap alignment and hence, these are predominantly used to fabricate epitaxial optoelectronic devices, in particular light emitting diodes (LEDs). LEDs are increasingly used in various optoelectronic applications as they are environment friendly, can be manufactured in miniature sizes with large volume and offer low power consumption, low maintenance cost, long lifetime and large color palette during lighting. In particular, when the active layer of a LED contains epitaxial quantum dots (QDs), the LEDs demonstrate advanced optoelectronic performance due to the superior quantum confinement of the QDs. However, the optoelectronic properties of these epitaxial QDs are highly dependent on their growth conditions, which generally control the material distribution between the QDs and their surrounding materials. Specifically, the amount of Sb within epitaxial InSb/InAs QDs, which is the material considered in the present Thesis, can be controlled by the corresponding growth parameters which eventually tune the band gap energy (E_g) of the QDs and, as a result, the corresponding LEDs emit light in the mid infrared (MIR) range of 3-5 μm. MIR LEDs in general are used designing MIR sensors utilized in various applications, such as toxic gas detection, medical diagnosis, free space optical communication, etc. In order to design the MIR LEDs using InSb/InAs QDs with improved efficiency, it is necessary to correlate the morphology and compositional distribution of the InSb/InAs QDs with nano/atomic scale resolution to their functional properties and growth conditions. In this regard, transmission electron microscopy (TEM) analyses could be helpful as the nano/atomic scale characterization tool, as it has been greatly utilized in the development of semiconductor heterostructures in the recent years.

Based on the aforementioned realizations, this chapter has been organized as follows. A brief introduction to the epitaxial III-V semiconductors in terms of optoelectronic applications is included in section 1.1. After this, as this PhD is focused on the analysis of epitaxial InSb/InAs QDs for LED applications, the functional properties of III-V LED structures, the epitaxial growth techniques forming QDs in the active layer of these LEDs and the significance of InSb/InAs QDs are discussed in sections 1.2, 1.3 and 1.4, respectively. Then, the importance of TEM as a powerful nanoscale characterization tool often used in the

semiconductor technology is described in section 1.5. Finally, the thematic unit of this Thesis is justified in section 1.6.

1.1 Introduction to III-V epitaxial semiconductors

Direct band gap III-V semiconductors such as InSb, GaAs, InP, GaN, GaSb, etc. and their corresponding alloys are the primary choice to design optoelectronic devices. These devices include photo detectors, LEDs, laser diodes, optical modulators, optical amplifiers, etc. which detect, modulate, generate and switch photons in a similar way as the electrons within an electrical circuit. The physical interaction between photons and electrons within these III-V optoelectronic devices has been used to construct wide varieties of complex optoelectronic systems those we use in our day-to-day lives. For example, arrays of LEDs are used to manufacture modern day televisions, computers, solid state lighting, etc. Moreover, other complex optoelectronic systems include the construction of compact disk (CD), blue-ray systems, digital versatile disk (DVD) used at home, bar code scanner at the supermarket, laser printer at the office, various internet enabled devices such as smartphones, tablet computers, etc.

The development of III-V optoelectronic devices initiated with the progression of LEDs in the early 1960s, followed by the development of semiconductor lasers. Holonyak *et. al.* [1] were the first to produce visible (red) LEDs associated to spontaneous emission while experimenting on GaAsP. Later on, independent groups (Holonyak *et. al.* [1], Nathan *et. al.* [2] and Hall *et. al.* [3]) published their works on GaAs based lasers in 1962. These devices contained simplistic single p-n homojunction and functioned only under pulsed conditions at very high threshold current densities. This facilitated rigorous research to fabricate more practical continuous-wave (CW) room-temperature semiconductor-based lasers. Later on, because of the development of the growth technology of liquid-phase epitaxy (LPE) [4], high quality lasers could be developed which contained double heterojunction of AlGaAs/GaAs/AlGaAs [5]. This double heterojunction facilitated two major advantages over the homojunction, which are: 1) the lower band gap GaAs region provided carrier confinement that enabled recombination across the band gap, and 2) a better optical field confinement could be obtained as GaAs possessed higher refractive index than of AlGaAs.

Due to the continuous development in the semiconductor growth technology, molecular beam epitaxy (MBE) [6] and metal-organic vapor-phase epitaxy (MOVPE) [7,8] techniques were established at the late 1960s which enabled reproducibility of thin films of the order of less than 100 Å, termed as the quantum well (QW) structures.

The aforementioned epitaxial techniques enable layer-by-layer deposition of two or more different semiconducting materials on a substrate forming a heterostructure. An epitaxial growth mode generally depends on the corresponding thermodynamic driving force and the level of misfit between the substrate and the overgrown layer(s). The typical atomistic processes which occur during an epitaxial growth include (a) adsorption, (b) diffusion, (c) growth of step-edge, (d) atomic terraces, (e) cluster nucleation and (f) desorption, which have been demonstrated in Figure 1. The quality of the heterojunction(s) within a heterostructure is dependent of these atomistic processes, which eventually influences the electrical, optical and thermal properties of the grown heterostructure. However, the determination of application-specific growth conditions and a semiconductor material arrangement for epitaxial growth are not straightforward. As a result, significant research and development has been performed to obtain optimum heterojunctions within semiconductor heterostructures inducing high quality optoelectronic applications.

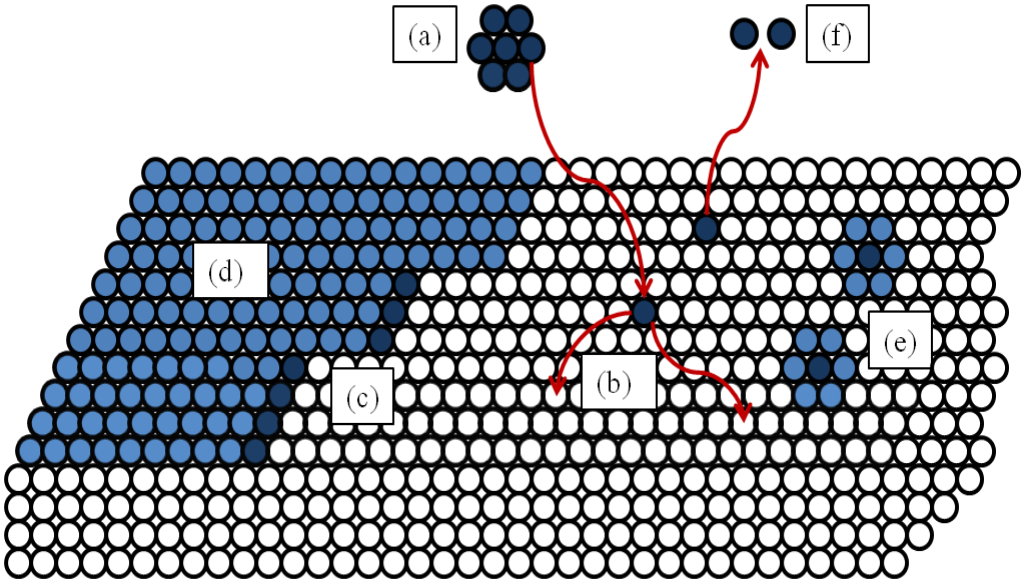

Figure 1: Typical atomistic processes during epitaxial growth: (a) adsorption, (b) diffusion, (c) growth of step-edge, (d) atomic terraces, (e) cluster nucleation and (f) desorption. Adapted from [9].

It must be highlighted that the sophisticated epitaxial growth techniques, i.e., MBE, MOVPE and their variants have higher technological costs than their simpler counterpart like LPE, but these costs are highly justified in many instances as these techniques offer favorable distinct properties of the materials obtained. These sophisticated techniques facilitate the growth of high quality materials at short growth time with relatively low growth temperatures which sometimes allows avoiding thermodynamic limitations. In addition to the growth of multilayer heterostructures, MBE and MOVPE can also be used to grow periodically abrupt heterojunctions containing superlattice (SL) structures which induce special properties in optoelectronic applications [10,11]. Moreover, with the help of suitable growth parameters and material arrangements, the heterojunctions in both heterostructure and SL structures can facilitate confinement areas with unique sizes where the carriers (electron and/or holes) become quantum confined and these unique sizes are comparable to the carriers' de Broglie wavelengths. This quantum confinement is obtained with the help of composition or doping variation in the materials which induce suitable potential barriers around the carriers. Based on the type of quantum confinement, generally three different types of quantum structures can be defined:

i) QWs, where the electrons (holes) can move in two directions but face optical confinement in the third direction. Because of this 1-dimension (1D) confinement, the QWs structures are called 2-dimensional (2D) structures. This unique type of confinement creates a greater potential barrier than of the bulk counterpart. Here, thinner the film, higher the E_g levels.

ii) In contrast to a QW structure, a semiconductor quantum wire (QWire) is optically confined in two directions but the electron (hole) can move in one dimension only. Due to the 2D confinement, QWires possess even greater E_g than of a QW. The QWires are also called nanowires.

iii) Electrons (holes) are confined in all three directions in a QD structure (3-dimensional (3D) confinement) and hence, they are called 0-dimenisonal (0D) structures. Highest E_g can be achieved in a QD comparing to the other two types. Similar to an atom, smaller QDs possesses discrete energy levels. Therefore, they are also called 'Artificial Atoms'. A QD can be of different shapes, such as cylindrical, cuboid, pyramidal, etc. [12].

Various quantum confined structures and their corresponding band diagram are illustrated in Figure 2. In this Figure, E represents the energy level of the systems (bulk, QW, QWire, QD), where E_{CB} and E_{VB} denote the energies of conduction band minimum and valence band maximum, respectively. The valence band is typically filled with electrons which can move to the high energy conduction band if excited and hence, influence the electrical conductivity of the system. Moreover, k and *n* represent the wave vector and dimension of the aforementioned quantum structures along (x,y,z) directions. ρ specifies the electron density of states (DOS) that tends to change as the dimension of the system changes. As observed in Figure 2, the DOS in the bulk material is in a parabolic shape that becomes sharper as the dimension of the bulk material decreases to quantum structures. These sharpened DOS is inherent to superior electronic and optical properties and therefore, these quantum structures are used as the active layer in optoelectronic devices such as LEDs, which is the core focus in this Thesis from application point of view. The next section has been dedicated to realize various aspects of a LED structure.

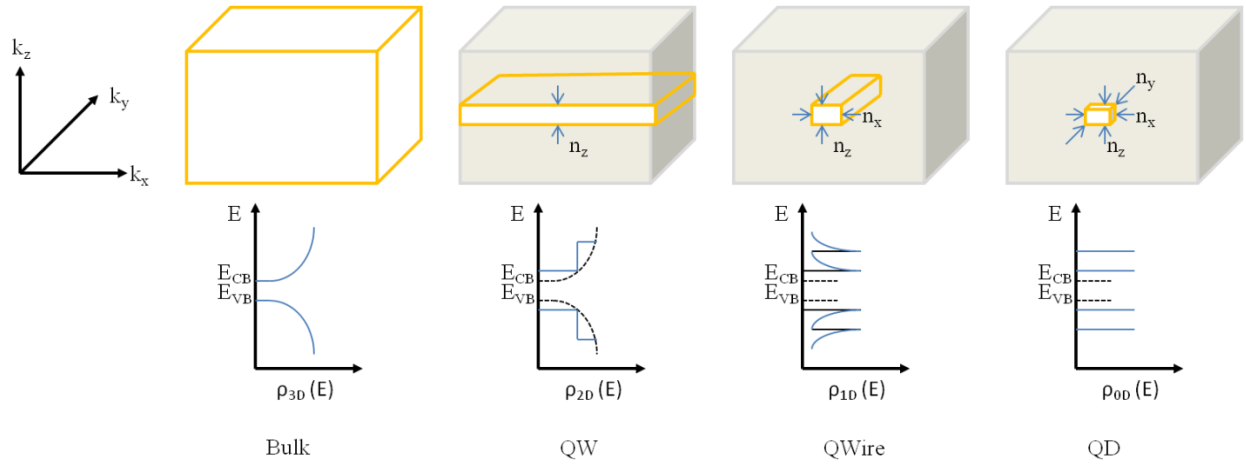

Figure 2: The density of states (from left to right) of bulk, QW, QWire and QD semiconductor structure. Here, as the electron (hole) motion is confined in more dimensions (from bulk to QD), the conduction and valence bands split into successively narrowing overlapping sub-bands. Adapted from [13].

1.2 Functional properties of III-V LEDs

In the present days, LEDs are becoming more and more popular for lighting applications. The reasons include that they require low maintenance, low fabrication costs, longer lifetime and low energy consumption. Moreover, the emitting direction of these LEDs can be controlled and, also, a unique color experiences can be observed through these LEDs. Consequently, they have become the popular lighting choice at home, offices, exteriors of buildings and emergency lighting. LEDs are also used as colorful reflectors in stage technology, direct and backlighting of paintings and statues in art galleries and museums and street lighting.

An LED emits light in variable wavelengths and is typically fabricated by semiconductor epitaxy with a p-n or p-i-n junction. The p-n junction can be either a homojunction of same material with variable doping concentration or a heterojunction of two different materials those induce the p-n doping. These material arrangements facilitate the electrons (holes) to diffuse to the p-type (n-type) material, creating a depletion region near the junction. This depletion region restricts further electron (hole) diffusion to the p-type (n-type) material. In the forward bias condition, an external energy source is used to assist electrons (holes) to break through the depletion barrier to the p-type (n-type) material within a LED structure. This phenomenon causes electron-hole recombination that induces emission of photons with frequency roughly proportional to the E_g of the quantum structures in the active region. Schematic of an operational, epitaxially grown, p-n LED structure has been demonstrated in Figure 3, where InAs/GaAs QDs are used as the active layer quantum structure. Here, GaAs with high electron concentration (n^+) has been used as the substrate of the LED structure. The layers grown underneath of the InAs QDs represent the n-type side of the LED structure, while the overgrown layers denote the p-type side. In p-type side, p^+-*GaAs* means that this particular GaAs layer possesses high hole concentration. Au contacts at the top and the bottom of the LED structure act as the ohmic contact to an external energy source, enabling a forwardly biased, fully functional LED device.

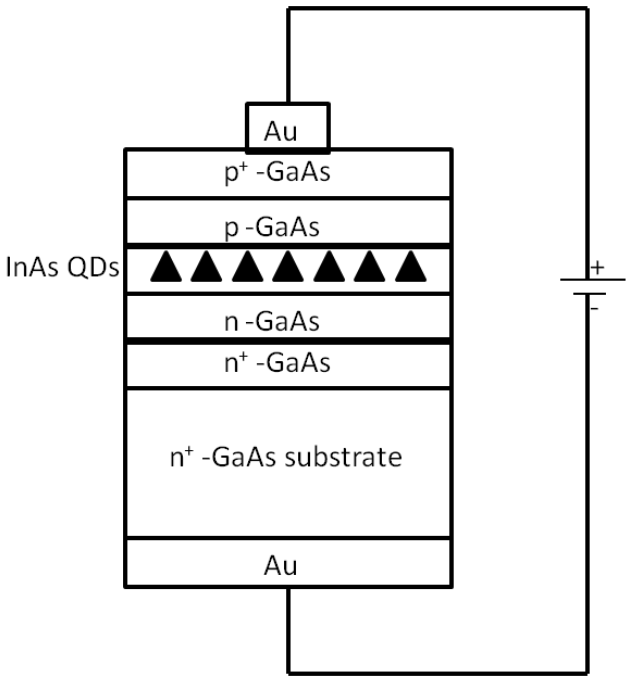

Figure 3: Schematic of a complete InAs/GaAs QD LED structure. Here, $n^+(p^+)$ represents layer with high electron (hole) concentration. Au represents the ohmic contact of the structure. Adapted and edited from [14].

To analyze the efficiency of a LED, measurements of internal quantum efficiency (IQE), external quantum efficiency (EQE) and Wallplug efficiency are taken into account. The IQE describes the efficiency of the active region by comparing the rate of photons generated to the rate of injected electrons in the active region. On the other hand, EQE emphasizes on the design induced losses by comparing the escaping rate of photons from the LED to the rate of injected electrons into the LED. Here, to calculate the escaping rate of the photons from the LED, the amount of light absorbed and/or reflected by the metal contact and/or substrate is taken into account. In case of Wallplug efficiency measurement, the conversion of electric power input into the LED to the total optical power output of the LED is considered.

Due to the 3D confinement of electrons that occurs in QDs, QDs possess highest IQE among all quantum structures. The discrete atomic-like electron energy levels in QDs induce the strongest modification in the corresponding electronic and optical properties. The

modifications include high radiative transition rate, narrow linewidth in emission spectra, reduction in non-radiative Auger recombination, etc. It has been reported that QDs can outperform QWs by reducing non-radiative Auger recombination and achieving higher efficiencies at higher currents in LED application [15]. In addition to LED applications, QDs are also found to be providing distinctive advantages in designing other semiconductor optoelectronic devices. For example, in comparison to QWs, QDs tends to perform with higher intrinsic gain [16] and less sensitive threshold current to temperature [17] associated to laser designing. This facilitates further research in developing QD lasers [18-20]. Moreover, integration of QDs with Si foundry process technology has also been achieved allowing the development of high performance QD lasers on Si substrates [21,22]. The design of QD infrared photodetectors (QDIP) [23-25] is another mention-worthy milestone of epitaxial QD technology. It has also been possible to attain quantum information processing technique through the QD induced quantum bits (Qbits) associated to their corresponding carrier spin states [26]. In addition, the anti-bunched photon emission capability of QDs [27] opened the pathway to develop single photon sources inherent to cryptography and quantum computing [28].

The basic light generation principle is similar in all quantum structures, which is termed as fluorescence. Figure 4 represents the fluorescence through a QD that has discrete energy levels and hence, regarded as QD fluorescence. If a basic LED structure is considered at a forward bias condition, electrons in the minima of a QD ground state (S_0) in valence band (VB) get excited and travel to a higher energy level (maxima) of an excited state (S_1) in the conduction band (CB), illustrated in Figure 4. Transference of the electrons from S_0 minima to S_1 maxima (denoted by upward red arrow) is called the *excitation state*. To allow excitation from S_0 to S_1, the energy absorbed by the electrons should be at least, $E_{S1(minima)}$-$E_{S0(maxima)}$, i.e., the E_g. When the excited electrons reaches to a maxima of S_1, they experience a rapid thermalization that allows those exited electrons to travel from the S_1 maxima to S_1 minima through phonon emission [29]. The downward maroon arrow in Figure 4 designates this rapid thermalization. Because of this, electron-hole (e-h) pairs are formed between the electrons in S_1 minima and the holes in S_0 maxima through coulomb interaction. Finally, the excited electrons return to the S_0 maxima (downward green arrow) causing e-h recombination that facilitates emission of fluorescence light. The emitted photon energy (E_g) is typically less than

the energy that causes the aforementioned excitation. This energy difference corresponds to the Stoke's Shift that expresses the characteristics of the material.

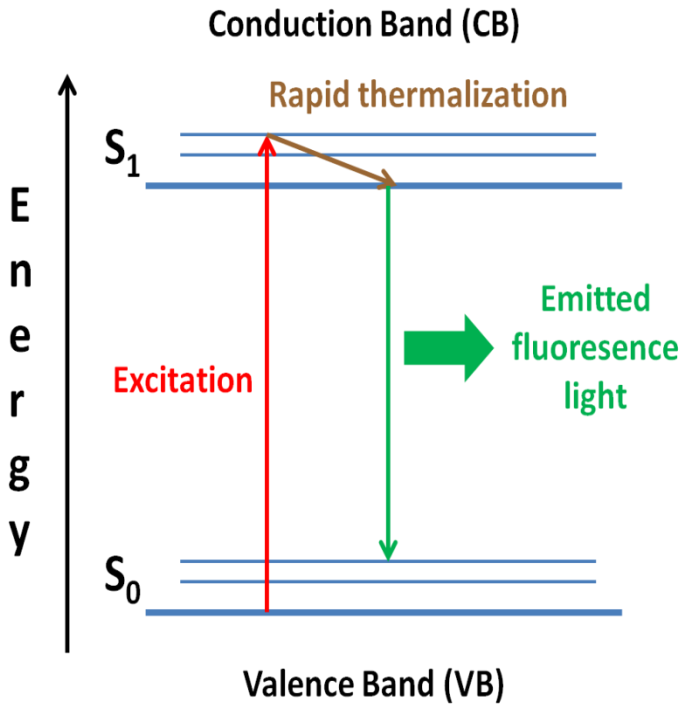

Figure 4: Schematic of luorescence within a QD with discrete energy levels .

Although the growth of the aforementioned epitaxial QDs is expensive, when they are incorporated to costly III-V wafers, fabrication of advanced optoelectronic devices is possible. Among various epitaxial growth techniques, MBE system supported conventional epitaxy (CE) and the emergent migration induced epitaxy (MEE) are the most popular mediums to form high quality, epitaxial III-V QDs. Because of this, the next section has been dedicated to perform comparative discussions between these two mediums in terms of corresponding QDs growth steps.

1.3 MBE induced III-V QDs growth modes: CE *vs.* MEE

During the MBE induced CE deposition, both group III and group V materials are deposited simultaneously in order to grow a III-V alloy on the growth surface. When a thin

layer of binary III-V alloy, termed as the wetting layer (WL) is deposited by CE on a III-V substrate/barrier/buffer layer with different lattice constant, the thin WL gets pseudomorphically strained (elastic strain) on the substrate/barrier/buffer layer because of the lattice mismatch between these III-V alloys. When the thickness of the WL reaches its critical thickness (WL_{crit}), the large elastic strain energy between the WL and substrate/barrier/buffer layer needs to be relieved, typically by forming energetically favorable small 3D islands with nanoscale dimensions, i.e., the QDs on the WL. The final material arrangements need to minimize the sum of the elastic strain energy, the surface energy and the interface energy. Such a growth process is termed as Stranski-Krastanov (SK) growth process [30-32]. A schematic of the formation of SK QDs by CE has been demonstrated in Figure 5a. It should be noted that the elastic strain energy may also gets relieved by forming unwanted defects and dislocations [33] which tend to hamper corresponding optoelectronic efficiencies. Therefore, cautions must be taken in selecting the growth conditions of both epitaxial and substrate/barrier/buffer materials to avoid the formation of such defects and dislocations.

The control in the uniformity of the size of the QDs is necessary to obtain good optical properties of the QDs, which is complicated to achieve through CE deposition [34,35]. The size of the CE grown SK QDs has been reported to be controlled by changing the amount of deposited material at a given growth condition, although could not be attained as expected [32]. On the other hand, the growth of these SK QDs is inherently dependent to prior deposition of a WL which induces detrimental effect on the optical properties of these QDs. For instance, it has been reported that WL tends to facilitate carrier scattering in QDs, leading to an unwanted decrease in the corresponding modulation bandwidth (BW) and maximum gain [36].

In order to eliminate WL induced effects and to control QDs sizes at a given growth conditions, MBE induced migration enhanced epitaxy (MEE) [37] has been considered. The MEE technique was initially developed to facilitate improved atoms surface migration that allows low temperature (LT) MBE growth of AlAs/GaAs QWs [37]. Afterwards, this technique has been used to obtain QDs [38] as an alternative to the SK growth mode in order to overcome the SK QDs associated aforementioned size inhomogeneity and surrounding WL imposed weak carrier confinement. During the MEE growth, group III and group V materials are alternatively supplied to the III-V substrate/barrier/buffer layer in contrast to the

simultaneous deposition performed in the CE growth mode. As a result, these materials experience increased mobility on the growth front due to their atomic form in MEE rather than III-V molecules-like structure in CE. The formation of MEE QDs can be initiated by either group III or group V deposition and their amount in the growth front is generally controlled by the corresponding substrate temperature. A schematic of the formation of WL-free, very small MEE QDs initiated by group V deposition have been demonstrated in Figure 5b. These MEE QDs in Figure 5b have been formed by single cycle of group III and group V deposition, but this can be repeated several times with various counts to form MEE QDs while accommodated by various growth conditions [34,39]. This implies that the change in the number of MEE cycles, along with corresponding growth parameters may also influence the optoelectronic properties of these MEE QDs through the manipulation of the QDs size and associated material distribution.

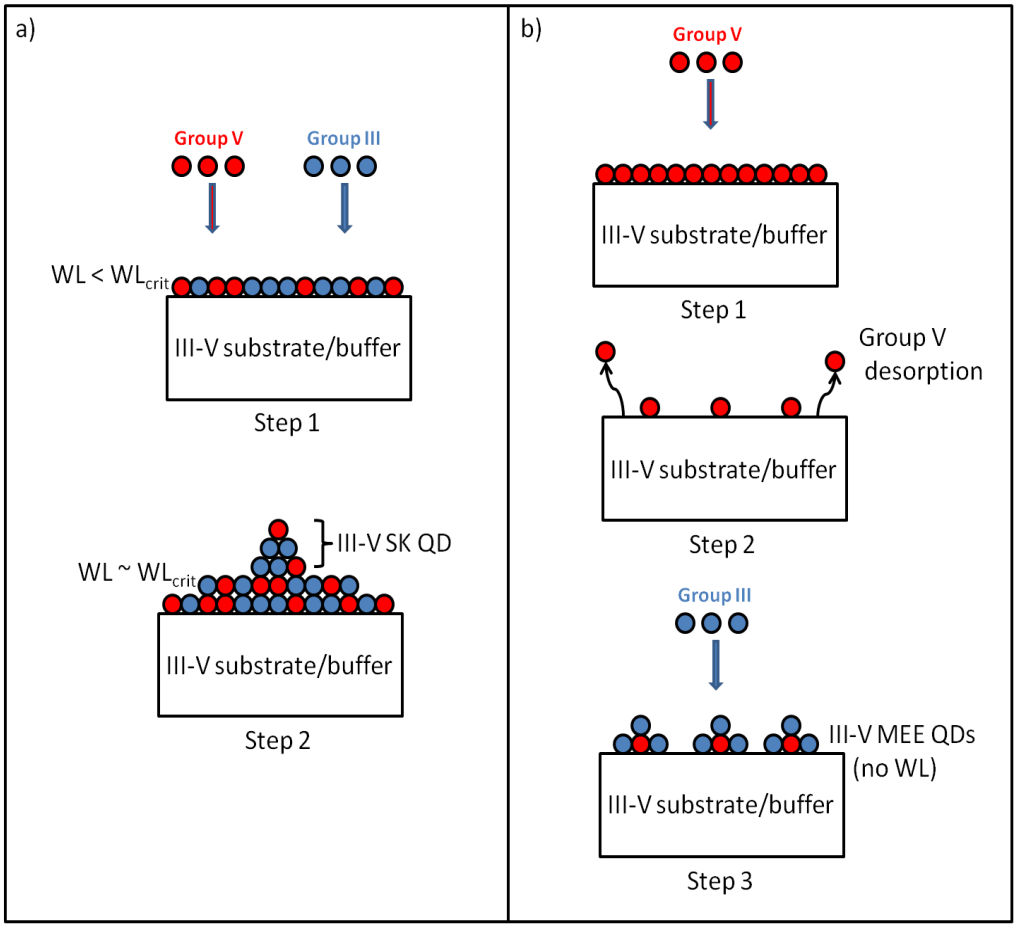

Figure 5: Schematics of the formation of III-V (a) single SK QD by CE and (b) MEE QDs with no WL.

In this Thesis, the MEE deposition technique has been used to form InSb/InAs QDs with applications as the active layer of LED structures in the MIR range. In order to realize the importance of InSb/InAs QDs for this application, the next section has been dedicated to explain the characteristics of InSb/InAs QDs from fabrication and optoelectronic points of view.

1.4 InSb/InAs QDs

The specific characteristics of InSb, InAs and their ternary $InSb_xAs_{1-x}$ offer various applications in the fields of electronics and optoelectronics. For example, InAs offers a small E_g of 0.35 eV, while having low electron effective mass of $0.023m_0$ and a high electron mobility of 33000 $cm^2\ V^{-1}\ s^{-1}$ [40-42]. On the other hand, InSb offers even lower E_g of 0.17 eV, while having a lower electron effective mass of $0.013m_0$ and a higher electron mobility of 77000 $cm^2\ V^{-1}\ s^{-1}$ [43,44]. In addition to that, InSb also offers a hole mobility of 850 $cm^2\ V^{-1}\ s^{-1}$. Because of these, InSb is of great importance in terms of high-speed, low-power electronic devices and quantum transport studies [45]. Moreover, InSb is also considered for thermoelectric power generation because of its possession of high thermoelectric figure of merit (0.6) [46]. Furthermore, the ternary compound of InAs and InSb, $InSb_xAs_{1-x}$, offers compositional tuning between InAs and InSb which enables the modulation of the physical and electrical properties precisely between the binaries. For example, InSb/InAs QDs with variable Sb compositions have reported to emit light in the MIR range [47-50]. The MIR spectral range contains the fundamental absorption bands of various hazardous gases such as CH_4 (3.3 μm), CO_2 (4.6 μm), CO (4.2 μm), and hence, InSb/InAs QDs associated MIR LEDs within MIR sensors are perfect choices to detect these gases associated to oil-rigs, coal mines, landfill sites, car exhausts, etc. Other applications of InSb/InAs QDs MIR LEDs may include non invasive MIR based medical diagnosis, bio-chemical imaging, detection of narcotics, free space optical communication at MIR range, thermal imaging for both military and civil situations, etc.

When InSb WL is epitaxially grown with a WL_{crit} ~ 1.7 monolayer (ML) on InAs substrate/barrier/buffer layer by CE, type II self-assembled SK InSb QDs form on the InAs substrate/barrier/buffer layer [51], thanks to the large lattice mismatch of 6.9% between these

two III-V binary alloys. Due to the presence of these QDs, Auger recombination in the type II broken gap band alignment is reduced and hence, an increase in the radiation lifetime in the associated narrow band gap LED structure is observed. In the discussed type II broken gap alignment, strong hole localization with quantized energy levels occurs in InSb QDs, while electrons are loosely confined within the InAs matrix, demonstrated in Figure 6. Yeap *et. al.* [52] realized this phenomenon through a thorough theoretical analysis on the self-assembled InSb QDs in InAs matrix by modeling the electronic structure of InSb QDs with variable shapes, aspect ratios, and compositions based on strain-dependent multiband k·p theory. Based on their outcome, there may be spatially indirect transitions between the QD and the matrix material and hence, acknowledging a possibility of QDs size and composition induced wavelength tuning.

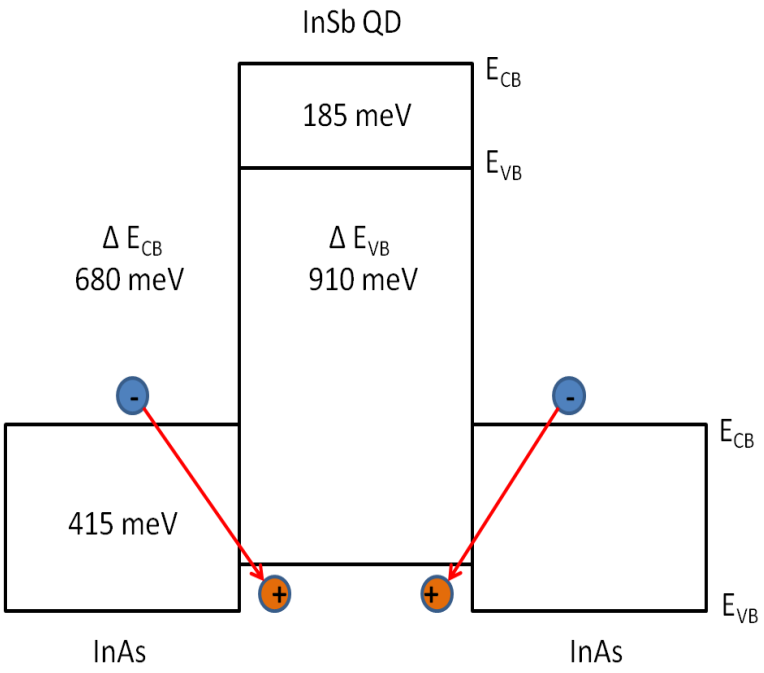

Figure 6: InSb/InAs type II broken gap alignment, where holes (orange circles) are entrapped in InSb QD and the electrons (blue circles) are in the InAs matrix. ECB and EVB represent conduction band and valence band energies, respectively. Adapted from [48].

In order to control the emission wavelength of the InSb/InAs SK QDs in MIR range, it is necessary to control the corresponding Sb composition of the QDs. This is complex to

achieve through the change in the amount of InSb deposition, as for any given growth condition, the composition and size of SK QDs does not linearly increase with the increase in the InSb WL thickness. For example, Karim *et. al.* [32] reported the growth of SK InSb/InAs QDs, most of them with similar sizes despite being obtained by depositing slightly different amounts of InSb (1.8 and 2 ML), emitting light at 4 μm in both cases. On the other hand, SK InSb QDs are surrounded by a WL underneath which, in general, has been reported to facilitate carrier scattering in the corresponding QDs, leading to an unwanted decrease in modulation BW and maximum gain [36] during optoelectronic applications. MEE seems to be a promising deposition technique to overcome the WL effect on the QDs, as discussed in section 1.3. Additionally, it has been reported that the tuning of the emission wavelength of MEE grown InSb/InAs QDs could be achieved through sub-monolayer (SML), i.e., ~ 1 ML insertion of InSb layer(s) [47-49]. Because of this, the realization of the effect of MEE growth on the formation of WL-free InSb/InAs QDs is one of the principle targets in this Doctoral Thesis.

The success of MEE grown InSb/InAs QDs depends on the growth conditions selected. For example, it has been reported that the thickness of InSb insertion can be controlled within a SML range of 0.6-1 or 1.4 ML while the substrate temperature is varied from 485^{o}C to 400^{o}C [47,49]. Other growth parameters which may impact on the aforementioned MEE growth include growth interruption (GI) period(s) during MEE growth [39,53,54], presence/absence of an annealing stage [34], type of group V flux [48], etc. Moreover, in order to integrate the QDs in the LED structure, they are needed to be covered with a capping layer(s). These capping layers tend to change the morphology and optical properties of the QDs underneath through material interchange between the capping layer and the QDs and these interchanges are often influenced by the capping layer growth temperature. For example, Hodgson *et. al.* [55] demonstrated that the morphology and optical properties of MEE grown InGaSb/GaAs QDs could be altered through the controlling of Sb-As atomic exchange induced by the overgrown GaAs capping layer growth temperature. This is comparatively a new area of research and no detailed investigation on the influence of capping layer growth temperature on MEE grown InSb/InAs QDs has been performed yet, specifically while the QDs are capped with InAs layer(s). As a result, an important target of

this Thesis has been fixed to determine the effect of InAs capping layer growth temperature that may induce Sb-As atomic exchange while grown on the MEE grown InSb/InAs QDs.

The aforementioned observations indicate that both the MEE growth mode and the InAs capping layer growth temperature may potentially modify the Sb distribution within the InSb/InAs QDs. This Sb distribution is directly correlated to the optoelectronic behaviors of the corresponding MIR LEDs and hence, a careful investigation of this distribution is required to understand the functional properties and growth conditions of the InSb/InAs QDs. For this, nano/atomic level characterization has been performed through TEM analyses in this Thesis to obtain visible realization of the aforementioned Sb distribution. Because of this, various TEM techniques have been introduced in the next section.

1.5 Transmission electron microscopy characterization techniques

TEM is an outstanding technique for nano/atomic level characterization in terms of acquiring morphological, structural and chemical information of organic and inorganic materials, including the semiconductor materials. Correlation of this information to corresponding design, fabrication and functional properties has opened the pathways for further development of the analyzing materials.

The use of electrons for imaging in the TEM techniques has revolutionized image acquisition with higher spatial resolution in the last decades compared to the photon-based imaging by optical microscopy techniques. An optical microscope permits acquiring images with the help of visible light with a visibility limit up to a wavelength of ~ 400 nm. As a result, they are incapable to image quantum confined structures (QW, QWire, QD) which have diameters compatible to the *de Broglie* wavelength of the corresponding electron wave function [56]. On the other hand, the electron-based image acquisition approach allows the TEM techniques imaging structures as small as atoms or molecules. The first electron microscope, which was designed by Ernst Ruska, was built in Berlin, Germany in 1931 [57]. Afterwards, the electron microscope was commercialized for the first time in 1938 by Ernst Ruska at Siemens in Germany. Such a great invention led Ernst Ruska to win a Nobel Prize in Physics in 1986. The improvement of electron microscopes is defined by the progression of the microscopes' spatial resolution. As a result, a new era of TEM revolution was observed

when the aberration correctors were introduced within these microscopes, offering distinctive enhancement in their spatial resolution [58,59].

There are three major components in TEM equipments, which include:

i) The illumination system that consists of a gun and the condenser lenses with a condenser aperture. The gun produces the electron beam and the condenser lenses guide the electron beam to the analyzing specimen either in parallel or converging mode. Generally, two types of guns are used in modern TEM machines: thermionic guns and field-emission guns (FEGs).

ii) The second system consists of the sample/specimen holder and the objective lens with an objective aperture. The interaction between the electron beam and the specimen takes place in this unit. The transmitted beam through the specimen is collected by the objective lens and then passed to the imaging system.

iii) The imaging system helps constructing magnified images with the help of several other lenses and then displaying the acquired image on a fluorescent viewing screen.

The TEM characterization includes a wide range of complementary electron microscopy techniques, such as diffraction contrast induced conventional TEM (CTEM), high-resolution phase contrast TEM (HRTEM), high angle annular dark field (HAADF) scanning (S-) TEM, energy-dispersive X-ray (EDX) spectroscopy, electron energy loss spectroscopy (EELS), etc.

In the CTEM technique, a parallel electron beam interacts with the specimen to form an image. In diffraction contrast, the incident electron beam interact with the crystalline electron transparent specimen and the elastically scattered electrons can be used to obtain information on crystal defects such as dislocations or stacking faults [60,61] and composition [62,63]. On the other hand, HRTEM is also used to obtain information on crystal structure and lattice imperfection [64,65], but in high resolution. Here, the information of the investigating material is obtained through the images formed due to the interference between the transmitted beam and some diffracted beams, termed as phase contrast. Because of this, HRTEM technique is susceptible to the change in specimen thickness and focus conditions. In terms of attaining compositional information from crystalline nanostructures [59,66], the

HAADF-STEM is considered to be a front runner as images with atomic column resolution with compositional information can be acquired with this technique. Here, atomic column resolved images are formed due to Rutherford dispersion where the transmitted electrons are mostly scattered at high angles after interacting with the nuclei of the atoms within a nanostructure. As a result, the atomic column-by-column intensity of a HAADF-STEM image is proportional to the average atomic number in an atomic column with power n ($I \alpha Z^n$), where n is varied within the range of 1.7-2. It must be pointed out that the HAADF-STEM intensity contains information of specimen thickness, in addition to the chemical compositions of the material. As a result, a precise compositional analysis is greatly dependent on considering the specimen thickness induced signal from the HAADF-STEM intensity. Other complementary chemical analysis techniques include EDX and EELS. In EDX, X-rays are created due to the interaction between the incident electron beam and the specimen. The corresponding operation takes place when the electron incident beam excites an electron in an inner shell in an atom, the excited electron leaves the atom and hence, a hole is created in its place. As a result, an electron from an outer shell (higher energy shell) fills this hole by releasing energy as X-rays. EDX works better with high Z materials, is a straightforward technique and the interpretation of the corresponding data is relatively easy. On the other hand, EELS reveals the compositional information through the amount of energy loss of the electrons within the incident electron beam after they interact with the specimen. In terms of the analysis by EELS, using the electrons with no energy loss (zero-loss peak, ZLP) is a useful way to measure TEM specimen thickness. As a result, establishing a correlation between ZLP EELS and HAADF-STEM analysis provides a potentially precise chemical composition analyzing technique. In contrast to EDX, EELS work better with relatively low Z material and the corresponding data interpretation is more complex.

Regarding the material analyzed in the present Thesis mentioned in Section 1.4, investigating the Sb composition at atomic column scale in the InAs capped InSb/InAs QDs grown by MEE is crucial to understand the effect of this growth method, the influence of the capping layer and the corresponding optoelectronic properties. Because of this, atomic column resolved HAADF-STEM analysis has been chosen as the principle TEM characterization technique in this Doctoral Thesis. In order to interpret the data obtained from the HAADF-STEM analysis, various specialized tools are available. In particular, in this

Thesis the quantitative HAADF (qHAADF) tool [67] has been considered. Using this tool, the ratio between the intensity within a region of interest (ROI) and the mean intensity within a region of known composition (reference region) located in the same HAADF-STEM image can be calculated. For this, integration areas (called *Mask*s) need to be chosen in both ROI and reference regions. This calculation reveals the normalized integrated intensities (R) on the ROI atomic columns, which eventually correlates the material composition. For a specific composition, the R values have been reported to be least dependent to the specimen thickness over a convenient range and based on this realization, a linear regression equation has been offered in [67] that relates the R values with composition. Later on, Hernández-Maldonado *et. al.* [59] verified that the aforementioned linear regression equation can also be used for experimental compositional quantification of a single material within other III-V ternary alloys. The equation was generally expressed as:

$$R_i = 1 + a*x_i \qquad (1)$$

In order to determine 'a' directly, the corresponding researchers offered an equation that considers parameters including N (which is the number of MLs containing both ROI and reference regions in a single HAADF-STEM image), the total number of ML deposition of the investigating material in a ternary within the N MLs ($\sum_{i=1}^{N} x_i$) and the summation of ML-by-ML average R_i values ($\sum_{i=1}^{N} R_i$) within the N MLs. It must be pointed out that the III-V [001] dumbbells in each row along [110] direction represents a single ML in a HAADF-STEM image. The proposed equation was expressed as:

$$\sum_{i=1}^{N} \boldsymbol{R_i} = N + a* \sum_{i=1}^{N} \boldsymbol{x_i} \qquad (2)$$

Combination of these two equations deduces the atomic column-by-column compositions of the investigating material within the analyzing HAADF-STEM image.

In addition to the intensity based analysis, atomic column resolved HAADF-STEM images can also be used to analyze lattice distortions generated by compositional changes or by structural defects in a material. For example, in terms of an InSb/InAs heterostructure, when Sb atoms are incorporated into InAs layers, the InAs layer experiences lattice distortion, since Sb atoms have larger size than As atoms. The identification of regions with lattice distortion in the InAs layer would reveal the incorporation of Sb within the InAs layer. Tools to quantify this lattice distortion are also available. Thus, the geometrical phase analysis

(GPA) method [68] is used to measure local lattice distortion within an atomic column resolved HAADF-STEM image [69,70] with the help of fast Fourier transform (FFT). Similar to the GPA tool, the peak pairs analysis (PPA) [71] tool can also generate a local strain map, but in real space.

It is worth mentioning that the success of the TEM analysis is highly dependent on the procedures to obtain electron transparent specimens to be studied. In order to prepare high quality electron transparent specimens from a bulk material, different methodologies are available, such as the conventional method or the focused ion beam (FIB) technique. The conventional method is performed by the steps of mechanical grinding with SiC papers and Ar^+ ion milling. Extreme cautions must be maintained during ion milling as this process could produce amorphization and/or impurity implantation into the specimen. On the other hand, Ga^+ ions are used in FIB for specimen milling, while the adjacent electron beam column facilitates specimen imaging and hence, thin electron transparent specimen can be prepared with *in situ* monitoring.

1.6 Justification of the theme of the Thesis

The aim of this Thesis is to contribute to the development of InSb/InAs QDs grown by MEE for the design of high electroluminescence (EL) generated LEDs at MIR range. As a result, nano/atomic scale characterization of the morphology and composition of the discussed nanostructures through aberration corrected TEM has been chosen as the core contributing medium that should induce necessary advancement in the future fabrication steps.

This Doctoral Thesis is presented as *Compendium of Publications*, and the corresponding articles are attached as appendices of this Thesis. Publication I is dedicated to develop a modification of the existing qHAADF tool (explained in section 1.5) so it can be applied to the material analyzed in the present Thesis, MEE InSb/InAs QDs. The modification allows selecting a reference region from a second HAADF-STEM micrograph, different from that one which includes the ROI region. This development is necessary for the analysis of many semiconductor materials including the one studied in the present Thesis, as very often complex heterostructures design or unwanted phenomena such as segregation prevents from finding an appropriate reference region in the analyzing HAADF-STEM image. In this paper,

the influence of important parameters such as the difference in thickness between ROI and reference regions or the mask size are also analyzed in order to allow a precise composition determination. Regarding Publication II, the material distribution in InSb/InAs QDs grown by the MEE technique, where the group III and group V elements are supplied alternatively, is analyzed quantitatively by aberration corrected HAADF-STEM. Here, the growth temperature of the InAs capping layer is maintained at 430ºC, the same temperature as the active layer. The corresponding CTEM and HAADF-STEM analyses revealed that scarce Sb-rich InSbAs agglomerates form within a InSbAs continuous WL due to high Sb segregation towards the growth direction. In order to reduce this high Sb segregation, a plausible strategy could be reducing the corresponding InAs cap growth temperatures. In order to ensure this speculation, the impact of InAs cap growth temperatures on the formation of the aforementioned InSbAs agglomerates has been analyzed in Publication III. Here, it has been observed through both CTEM and HAADF-STEM analyses that a reduced InAs cap growth temperature increases the Sb composition in the InSbAs agglomerates, likely due to a reduction in Sb segregation. The modification in the Sb distribution observed is proved to tune the photoluminescence (PL) response of the active layer in the MIR range.

The aforementioned publications and this Doctoral Thesis can be considered as a step-forward to the determination of the optimum growth steps to form high quality InSb/InAs QDs without WL which may facilitate designing high efficient MIR LEDs.

Chapter 2

Hypotheses and Objectives

The main hypotheses of this Doctoral Thesis are described below:

i) The addition of Sb to III-V epitaxial semiconductor nanostructures improves the functional properties of advanced optoelectronic devices, especially to work in the infrared regions. In particular, the addition of Sb facilitates designing MIR LEDs, as well as long wavelength infrared lasers and photo-detectors (λ >3 μm), optical communication lasers (λ = 1.3-1.55 μm) and high speed electronic devices. Moreover, the MEE grown Sb-containing nanostructures allow improved optoelectronic properties in a controlled manner over the conventional MBE grown nanostructures.

ii) The analysis of these III-V-Sb materials by advanced TEM techniques with resolution at the nano/atomic scale could contribute to the development of these materials by providing information on the compositional distribution of the material, the morphology of the nanostructures and the strain in the layers, opening new pathways to modify various compatible optoelectronic properties.

The main objective of this PhD is to understand the Sb distribution and overall structural properties of InSb/InAs QDs obtained using the non-conventional growth method of MEE in order to configure optimum design parameters for applications in highly efficient gas and bio-sensing LEDs at MIR range.

As a result, the following specific objectives have been established:

i) Modification and analysis of the method based in qHAADF to extract quantitative compositional information from HAADF-STEM images to be used in the study of InSb/InAs QDs in order to understand the Sb distribution in the material.

ii) Investigation on the formation of InSb/InAs QDs grown by MEE in order to understand the relation between this growth technique and the final structural characteristics of the material.

iii) Analysis of the effect of the InAs cap layer growth temperature in the structural properties and Sb distribution of InSb/InAs QDs grown by MEE.

Chapter 3

Critical analysis of the state of the art

Semiconductor QDs grown by epitaxy on substrates act as 0D quantum structures because the electrons/holes are confined in all three directions in a QD. A very small QD can have discrete energy levels as an atom and hence, they are also termed as "Artificial Atoms". Consequently, smaller the size of the QDs, better the quantum confinement. According to this observation, growing very small InSb/InAs QDs would facilitate designing superior optoelectronic devices whose performance depends on the quantum confinement, for example the above mentioned LEDs. However, controlling the size of MBE induced CE grown InSb/InAs QDs is not easy, as explained before. Additionally, the corresponding WL inherent to SK QDs decreases their optoelectronic performance. As a result, MBE induced MEE is emerging as an alternative to form small InSb/InAs QDs without a WL. The MEE growth process is highly influenced by the associated growth conditions which eventually determine the size of the QDs. Because of this, the main idea of this Thesis is to contribute to determine the optimum MEE growth parameters which would help forming very small InSb/InAs QDs with no WL.

In general, the formation of MEE QDs can be initiated by either group III or group V deposition and their amount in the growth front is generally controlled by the corresponding substrate temperature. In case the MEE growth is initiated with group III materials, the associated adatoms (surface atoms) have longer migration length (than CE) on the substrate/barrier/buffer surface as they do not go through any reaction induced by the group V materials. This migration length is typically controlled by the associated substrate temperature [72], therefore, a substrate temperature must be chosen that facilitates 2D island nucleation. Afterwards, when deposition of group V materials is performed, the group V atoms bond with the group III nucleated regions and 3D QDs form. However, it has been reported that the formed QDs in this way are also surrounded by a WL underneath, although thinner if compared to the WL during CE growth [35]. On the other hand, this WL formation underneath may be overcome if MEE growth of only group V material is performed as demonstrated in refs. [47-50]. In this case, when the substrate/barrier/buffer layer is exposed to group V molecules, efficient group V exchange occurs between the deposited group V atoms which stick on the growth surface and the group V constituent of the substrate/barrier/buffer layer. The amount of stuck group V atoms and eventually, the amount of group V exchange is generally controlled by the corresponding growth temperature and as

a result, a suitable growth temperature must be chosen so that very small QDs form with high density [50]. However, WL-free, very small III-V MEE QDs may also be formed if the group III materials are deposited after the aforementioned V exchange. In this case, the enhanced migration length of the group III material is generally restricted by the group V materials in case a high group V surface density exists [73].

In order to grow very small InSb/InAs QDs by MEE without a WL, a single InSb SML insertion could be performed by exposing the InAs growth surface to a Sb flux. It has been reported that a single nominal SML InSb insertion of ~ 1 ML obtained through Sb deposition by MEE within a InSb/InAs heterostructure facilitates forming very small QDs with a mean lateral size of ~ 2.5 nm and with high sheet density [50]. That SML thickness of the InSb insertion generally depends to the growth temperature. According to Ivanov *et. al.* [49] and Solov'ev *et. al.* [47], the nominal InSb insertion thicknesses can be controlled within 0.6-1 or 1.4 ML, if the corresponding growth temperature is varied from 485^{o}C to 400^{o}C. The 0.6-1 or 1.4 ML InSb insertions facilitate InSb PL emission wavelengths at the MIR range of 3.9-4.3 μm, respectively, at room temperature (RT) of 300K, after capped by InAs layer. As a result, possibilities to design RT optoelectronic devices which emit light in variable MIR wavelengths may arise. Moreover, for a specific growth condition, the InSb/InAs MEE QDs typically possess uniform size distribution in comparison to its SK counterpart and hence, better optical properties are observed in the MEE QDs [34]. On the other hand, it has been reported that the MEE QDs which formed by multiple MEE insertions of III-V materials are surrounded by thinner WL underneath than the WL that facilitates forming SK QDs [39]. This observation implies that if the InSb/InAs MEE QDs are grown through single SML InSb insertion, even thinner/no WL underneath would surround those QDs. As a result, these InSb/InAs MEE QDs would be least/not subjected to the population of WL states which induce sub-linear increase of the population inversion in the QDs with carrier density [36]. Because of this, WL associated reduction in the associated maximum gain and modulation BW would be possible to overcome in InSb/InAs MEE QDs.

As mentioned above, variable SML InSb insertion thicknesses are achieved by changing corresponding MEE growth temperatures. Here, these insertion thicknesses depend on how many Sb atoms stick to the InAs growth surface. However, when these SML InSb layers are capped with a capping layer, some of those attached Sb atoms incorporate into the

capping layer [74]. Various previous articles indicate that the incorporation of Sb atoms to the capping/overgrown layer generally happens through segregation [75-77] and a high growth temperature induces high Sb segregation [53,74,78-81]. In case an InAs capping layer is used, this Sb segregation may likely form a ternary InSbAs alloy [74]. Therefore, the MEE growth temperature must be controlled to control the quantity of Sb segregation that eventually influences Sb contents within the ternary alloy.

In addition to the controlled growth temperatures, material flux ratio and flux type may also help growing good quality heterostructures. For example, Shen *et. al.* [80] has demonstrated that a change in Sb/As flux ratio, controlled by Sb/In and As/In flux ratios, influences overall structural quality and Sb composition in CE grown type II InAs/InSbAs SLs. In a similar manner, the change in Sb/As flux ratio may also affect the quality of InSb/InAs heterostructures with the possibility to control the corresponding MEE facilitated Sb distribution in the aforementioned InSb/InAs QDs. Moreover, the growth temperature to grow InAs capped InSb/InAs heterostructure can be varied by using either the dimers (As_2 and Sb_2) or the tetramers (As_4 and Sb_4) or the combination of both [48]. The dimers allow growing the heterostructures at a lower growth temperature than its tetramer counterpart to induce same PL emission wavelength. Since Sb exchange is harder in As_2 than As_4, there is less Sb-As exchange between the InSb and As_2 associated InAs cap layer and as a result, smaller QDs with higher Sb composition may form than in the exchange between InSb and As_4 associated InAs cap. This implies that the usage of As_2 during InAs capping and the MEE growth associated to single SML InSb insertion may facilitate the formation of very small QDs as aimed in this Thesis. Additionally, incorporation of even more Sb atoms within these small QDs may be achieved through introducing some modifications during the growth of these QDs, such as the usage of InAs cold caps (CC).

The term CC refers to those capping layers which are grown in a lower growth temperature than the under-grown active layer growth temperature, which could influence the atomic exchange between the capping and the active layers. For example, Hodgson *et. al.* [55] demonstrated that MEE grown uncapped, double-lobed surface InGaSb/GaAs QDs with high lateral size turn into small core InGaAsSb QDs surrounded by highly intermixed disc, if capped by GaAs CC. Such a change in the QDs morphology and PL response of the core QDs has been correlated to the presence of GaAs CC. In a similar manner, change in morphology

and PL spectra may also be observed if InAs CC is deposited over MEE grown InSb/InAs QDs, influencing the corresponding Sb-As atomic exchange. However, care should be taken when reducing the growth temperature of InAs layers. Growth temperatures $\geq 400^{o}$C have been chosen to grow good quality InAs layers in various previous literatures [47,49,53,74,80-82]. For instance, Ye *et. al.* [82] illustrated that if InAs/InAs layer is grown below 430^{o}C results in an undulating surface. Because of this, attention should be paid to the effect of growing InAs CC at LT on InSb MEE QDs.

In addition to the usage of CC, GI period during the MEE growth and a post growth annealing step may also affect the morphology and density of these MEE grown InSb/InAs QDs. For instance, Semenov *et. al.* [53] demonstrated that performing a GI period without a Sb flux after the MEE deposition of Sb on an InAs layer enhances the size uniformity of the MEE grown InSb/InAs QDs. On the other hand, Zhuang *et. al.* [34] illustrated that a post-growth annealing under Sb flux reduces MEE grown InSb/InAs QDs density from ~ 10^{10} to 10^{9} cm^{-2}, while enhancing QDs dimensions and destroying QDs size homogeneity. The LT InSb PL peak could only be observed in a non-annealed case while capped with InAs layer if the cap layer temperature is reduced from 490 to 450^{o}C, which eventually established the idea of growing InAs CC in this Doctoral Thesis.

In order to realize unique Sb composition distribution that is influenced by aforementioned MEE growth parameters and the corresponding Sb segregation, HAADF-STEM technique has been chosen as the core characterization technique in this Thesis which was described in brief in section 1.5. Several methodologies [66,84-87] are available in order to interpret the HAADF-STEM images in terms of compositional analysis, but many of them are dependent to time consuming multiple experimental analyses associated to variable image acquisition parameters or the integration of additional instruments to the existing ones or they are just incompatible to realize material segregation induced compositional quantification. In order to perform direct and reasonably fast composition quantification from HAADF-STEM images, the qHAADF tool [67] can be considered, which was also briefly discussed in section 1.5. The qHAADF tool has been used to analyze the atomic column intensities induced by III-V ternary alloy composition within a QD [75]. As a result, the size and shape of the analyzed QD structure could be realized through the corresponding intensity variation. Moreover, combining this qHAADF tool with the analysis observed in ref. [59] opens the possibility to

directly convert the above mentioned atomic column intensities to their corresponding compositions. Therefore, the combination of these two analyses in refs. [59,67] has been used in various QDs based compositional quantification [88-90]. For instance, Sb composition within GaAsSbN capped InAs/GaAs QDs was quantified using this combination [88]. Consequently, this combination could also be considered to quantify Sb composition within the InSb/InAs SML heterostructures while influenced by the MEE growth, InAs capping layer growth temperature and the corresponding Sb segregation effects to realize the associated optoelectronic behaviors.

Chapter 4

Joint discussion of the obtained results

Investigation of composition distribution within III-V heterostructures is necessary to understand corresponding MBE growth parameters and optoelectronic properties. In this Thesis, in order to understand the Sb distribution in MEE InSb/InAs QDs, atomic column resolved HAADF-STEM has been chosen as a suitable technique for this purpose, as explained before. The intensity within HAADF-STEM images (related to the composition distribution) can successfully be quantified using the qHAADF tool, as exemplified for III-V nanostructures in [75]. In order to implement this qHAADF tool, a reference region, which is an area of known composition such as the substrate, the buffer or the barrier layer typically made of the same III-V binary alloy as in the analyzing III-V ternary alloy in the ROI must be present in the same HAADF-STEM image that contains the ROI. However, locating a reference region may be complicated within the MEE QDs as they are typically formed by multiple cycle of group III and group V depositions [34,39] and they also suffer from segregation in some cases. Therefore, the compositional analysis of these MEE QDs by the qHAADF tool may not be straightforward. The solution to the problem of reference area selection may be achieved by selecting the reference area from a second HAADF-STEM micrograph, as demonstrated in Publication I. The possibility of choosing the ROI area from one HAADF-STEM micrograph (ROI image) and the reference area from another HAADF-STEM micrograph (reference image) for qHAADF interpretation of the ROI image allows extending the application of this method to a wide variety of materials that were limited before by the requirement of having a reference region sufficiently close to the ROI area. Additionally, magnification restriction observed in the existing method has been possible to be overcome during the acquisitions of the images. The modified method allows analyzing high resolution HAADF-STEM images associated to highly magnified ROI and reference regions, as moderate magnifications to allow ROI and reference regions to be included in the same image is not required. Consequently, this modified method could be a good medium for compositional analysis of the aforementioned MEE QDs structures where locating a reference region is complicated due to multiple layers and material segregation.

The functionality of the modified qHAADF method can ideally be analyzed with the help of HAADF-STEM simulated images which contains our core material InSb/InAs. According to publication I, in order to perform the analysis of the modified qHAADF method with InSb/InAs, the ROI image has been constructed with simulated InAs/$InSb_xAs_{1-x}$/InAs

([001]) heterostructure and the simulated reference image has been considered to accommodate pure InAs ([001]) material with no Sb. Similar to the existing qHAADF tool, the quantification of the intensity by the modified tool is also initiated by choosing an intensity region, i.e., a Mask, on each analyzing ROI and reference images. In order to quantify Sb within the aforementioned simulated images, these Masks are applied on group V columns in both ROI and reference images. Afterwards, the Mask intensities of each atomic column in the ROI image are divided by the mean of the Mask intensities in the reference image. These ratio of Mask intensities between the ROI and reference images are denoted by R (normalized integrated intensities values in the ROI image). Later on, these R values can be converted to Sb composition with help of the analysis proposed by Hernández-Maldonado *et. al.* [59]. It should be highlighted that the selection of Mask size and location is a crucial factor for precise compositional quantification. In order to realize how the Mask sizes affect during Sb quantification within InSb/InAs heterostructures, different Mask sizes have been investigated in this Thesis those assist compositional analysis through modified qHAADF method, as explained below.

In the literature, there is no detailed agreement regarding the Mask sizes in terms of appropriate composition quantification. For example, it has been proposed that the size and location of the Masks on the analyzing atomic columns should be chosen in such a way that the corresponding quantifications of the analyzing material are the least affected by the neighboring atomic columns [59], such as through atomic column crosstalk [91,92]. As the starting point, in this Thesis the first Mask has been chosen in a similar way as in ref. [59] that has been claimed to offer the least susceptibility of the analyzing atomic column to its neighbors and it has been termed as Mask1. However, some other researchers have observed that a Mask that surrounds a whole analyzing atomic column offer good HAADF-STEM quantifications in terms of varying convergence angle, magnification, source size and defocus [93], specimen associated small mis-tilt [94], aberrations and astigmatism [95] and scan induced noises [96]. Moreover, it has also been reported that, if a Mask is considered that imposes rectangular Voronoi cell [97] around each whole dumbbell, the associated average HAADF-STEM intensity values may allow revealing compositions closer to the nominal composition [98]. As a result, in addition to Mask1, two other Mask sizes, termed as Mask2 (covers each whole group V column) and Mask3 (covers each whole dumbbell) have be

considered in this Thesis during modified qHAADF quantification from HAADF-STEM simulated images. The results obtained in this analysis have shown that these three Masks offer very similar results, with only slight differences between them. In particular, Mask3 has been found to possess marginally the least average standard error and hence, Mask3 has been considered during Sb compositional analyses in all InSb/InAs HAADF-STEM images in this Thesis.

Besides the mask, the high level of accuracy in the measurement of composition obtained with the simulated images is also related to the fact that the same imaging parameters and specimen thickness can be maintained in both ROI and reference images. This accuracy is likely to suffer from some degradation in terms of experimental analysis if there is a poor calibration of the required parameters during the image acquisition. In particular, to obtain the R values by the modified qHAADF method, the experimental ROI and reference HAADF-STEM images are acquired separately and hence, care should be taken in maintaining same image contrast, brightness and magnification in the analyzing two images. Additionally, it is essential that both images contain regions of the specimen with same thickness, as thickness has a strong effect in HAADF-STEM intensity. Finding a reference region with same specimen thickness as the ROI experimentally is complicated because the specimen thickness varies gradually in the electron-transparent region, so when the ROI and the reference area are situated far from each other, the corresponding experimental specimen thickness will likely be different. Moreover, the specimen thickness within a single image may also fluctuate induced by an irregular surface associated to the TEM specimen preparation techniques. These thickness variations contribute to the HAADF-STEM intensity, along with the corresponding material composition and therefore, this thickness variation must be compensated in order to obtain composition only contribution. To realize how thickness variation may contribute in experimental InAs/$InSb_xAs_{1-x}$/InAs associated HAADF-STEM composition analysis of Sb, in this Thesis R values have been calculated using simulated images where the specimen thickness between the simulated ROI and reference images are varied. In particular, the specimen thickness of the simulated ROI images has been varied within 15 nm to 35 nm, while maintaining the reference image (InAs) thickness in 30 nm. This has been repeated for different Sb compositions in the range of 0-100%. The measured R values have been found to change by a factor of ~ 0.02 ± 0.004 for each 1 nm

specimen thickness variation (Δt) in every analyzed Sb composition. Because of this, the equation 1 in section 1.5 can be re-written in the following format that considers specimen thickness effect during R calculation:

$$R_i = 1 + a*x_i \pm 0.02*\Delta t \quad (3)$$

This equation implies that Δt strongly influences R values and precise thickness measurements of both ROI and reference regions are essential for the precise atomic column-by-column Sb quantification in the ROI that contains $InSb_xAs_{1-x}$ alloy. The utilization of equation 3 helps quantifying specimen thickness variation in R values and hence, opens the possibility to acquire composition only information by the modified qHAADF where the experimental ROI and reference images do not have exactly the same specimen thickness. Moreover, this equation may also help obtaining experimental R values using the existing qHAADF analysis, in case the image suffers from different specimen thicknesses in ROI and reference areas within the image. Therefore, specimen thickness of each experimental HAADF-STEM image must be measured through ZLP EELS analysis in order to quantify Sb with the highest precision.

According to publication I, it has been proved that the modified method is highly compatible to the existing method from experimental point of view. Thus, the modified method has been shown to experimentally obtain Sb induced ML-by-ML similar average R values as in the existing method within a InSb/InAs heterostructure by compensating ROI and reference image thickness variation through equation 3. Additionally, the modified qHAADF method could also be used to determine In composition induced R values within experimental InSb/GaSb SML SL structure through equation 3, where the reference region was situated far away. Here, since the ROI and reference regions are situated far away from each other, it is difficult to contain both the ROI and reference regions in a single HAADF-STEM image. Consequently, obtaining the aforementioned In induced R values is not possible by the existing qHAADF method. Therefore, in such a scenario, where the reference region is selected in a second HAADF-STEM image, the modified method assures its significance over the original method.

Publication II and III describe the influence of MEE growth and InAs cap growth temperatures in the Sb distribution within InSb/InAs heterostructures. The growth process

followed in the analyzed samples has been based in previous studies which report that InSb SML thicknesses can be formed by 20s of MEE deposition of Sb on InAs growth surface [48-50]. In order to realize an improved control on InSb deposition thickness, three samples have been grown where each 20s MEE deposition of Sb is followed by additional MEE depositions of 5s In and 6s Sb, while maintaining a growth temperature of 430^{o}C. Afterwards, each MEE deposition is followed by the CE deposition of InAs cap layer with growth temperatures of either 430^{o}C, 380^{o}C or 310^{o}C. Since the InAs cap growth temperature of 380^{o}C and 310^{o}C are lower than growth temperature of the MEE depositing layer (430^{o}C), they are called InAs CCs. Based on our experimental X-ray diffraction (XRD) analyses, the simulated XRD data where flat layers of pure InSb composition is assumed have indicated InSb SML thickness of 0.65 ML at the sample with InAs cap layer growth temperature of 430^{o}C, which gets thicker in the CC samples. In the CC samples, the InSb SML nominal thicknesses become 0.86 ML and 1.02 ML for 380^{o}C and 310^{o}C InAs CC samples, respectively. This suggests that a larger amount of Sb is incorporated in the material for reduced CC growth temperatures, which may tune the emission wavelength of the heterostructure. In order to realize the optical behavior of the analyzed materials, LT PL analysis has been performed.

It has been shown in publication III that the emission wavelength of the InSb PL peak in 430^{o}C sample is lower than the InSb PL peak wavelength in 310^{o}C sample. It is well known that Sb incorporation in III-V semiconductors reduces the associated bandgap energy and hence, imposes a red shift in wavelength [99,100], where a higher Sb composition induces a larger red shift [48]. Therefore, the PL spectra obtained indicates that the 430^{o}C sample that nominally contains 0.65 ML InSb layers seems to have lower Sb composition than the 310^{o}C sample that nominally accommodates 1.02 ML InSb layers. However, as per 380^{o}C sample, two InSb PL peaks appear at either side of the InSb PL peak of 430^{o}C sample. This indicates the formation of two distinct quantum structures within the associated InSb layers. Moreover, the appearance of these two InSb PL peaks at either side of the 430^{o}C sample associated InSb PL peak suggests that the 380^{o}C InAs CC may help forming both Sb-rich and Sb-poor regions within the InSb layers. This implies that Sb-rich clusters could be high density QDs which are significant enough to induce variation in the PL emission. In a similar manner, two InSb PL peaks were observed in refs. [53,74], where the corresponding authors concluded that the peak at a lower wavelength represents InSbAs WL, while the peak

at higher wavelength assures the presence of InSb QDs with higher Sb composition than the WL. However, our speculation could also be extended to the fact that the QDs density may get even higher at the lower 310^{o}C InAs CC, since the 310^{o}C CC sample induced InSb PL peak intensity is higher than the 380^{o}C CC sample induced InSb PL peak for Sb-rich regions at the same emission wavelength. In order to examine the above mentioned assumptions, diffraction contrast induced 002 dark field (DF) CTEM analyses as the initial TEM characterization technique have been performed on the TEM specimens of these samples.

In general, 002 DF diffraction contrast CTEM analysis reveals chemically sensitive information of crystalline micro/nanostructures within a TEM specimen. As a result, this technique is generally considered during TEM-based composition analysis of epitaxial layers [62,63]. In this Thesis, the InSb/InAs layers have been investigated through 002 DF analyses, and the details are included in Publications II and III. Despite the existence of individual InSb layers within all samples has been observed, this analysis has shown that neither of these InSb layers has SML thickness and hence, it is likely that the InSb SMLs have been converted to InSbAs alloy layers. 002 DF images have shown that the InSbAs layer in either sample is not homogeneous as random nucleated regions are located along the layers. These agglomerated regions lack common QD shapes found in literature (cuboid, cylindrical, pyramidal, etc. [12]). According to publication III, the size of InSbAs agglomerates seem to get bigger and more continuous as the InAs cap temperature is reduced. This observation qualitatively supports the experimental XRD analyses, discussed earlier. Regarding the emission properties, the corresponding red-shift observed in the PL emission of the CC samples can be justified by the increase in the Sb content derived from the 002 DF images. However, it must be pointed out that two different quantum structures with statistical significance are expected in the 380^{o}C sample since the associated PL spectra contains two InSb peaks at different wavelengths, but such two different structures are not evident at the sight of the 002 DF images. TEM analyses allows analyzing small regions of the specimen (around tens of nms) at a time, while a PL spectrum is performed on the whole heterostructure with dimension up to several hundreds of nms. Because of such different characterization approaches, a direct correlation between the obtained results by these two techniques is sometimes difficult to carry out. In terms of the single PL peak observed in the 430ºC sample, it could be related to the formation of small agglomerates which contain low Sb composition. Comparatively, the single peak observed in

310ºC InAs CC sample may be associated to either Sb-rich continuous layer or bigger InSbAs agglomerates.

As per 002 DF analyses in publication III, the InSbAs layers exist as a continuous layer i.e., like WLs, unexpected in typical MEE induced SML growth. The conversion from nominal SML thicknesses (measured by XRD analyses) to the nms thick continuous WLs in either sample suggests that both a lateral movement of the Sb atoms and the upwards segregation have taken place during growth. The lateral movement of Sb atoms is improved while deposited by MEE on InAs surface, as explained before. Afterwards, it is likely that Sb/As exchange takes place on the InAs growth surface [53]. Semenov *et. al.* [53,74] demonstrated that, during InAs capping layer deposition, some of the Sb atoms tend to segregate into the InAs capping layer, which eventually forms the InSbAs WL. It must be pointed out that the balance in chemical potentials of the surface and bulk atoms at the sub-surface is essential to the thermodynamics of segregation [101]. Because of this, when the difference between the calculated exchange energies of $E_{Sb/As}^{bulk->surface}$ =1.68 eV and $E_{Sb/As}^{surface->bulk}$ =1.75 eV becomes positive, Sb segregation occurs [102] that balances the chemical potential. The tendency of Sb to segregate highly depends on the corresponding growth temperature observed in various previous works [53,74,78,79], where a high Sb segregation is induced by a high growth temperature. In terms of InAs capped InSb/InAs heterostructures, Sb segregation initiates when Sb atoms break free the low In-Sb binding energy of 1.40 eV [103]. Afterwards, an exchange between surface atomic species, i.e., As from InAs cap layer and sub-surface Sb segregant atoms occurs that produces a floating layer at the growth surface. A similar behavior has also been observed experimentally in other III-V semiconductors [104-106]. This floating layer tends to impose great influence on the growth dynamics in semiconductor alloys. For example, it has been reported that Sb containing floating layer is formed during GaAs capping on GaSb/GaAs heterostructure and eventually, discontinuous layer (WL) with low volume GaAsSb nanostructures is formed [75]. This observation implies that segregation induced floating layer and strain induced atomic re-distribution eventually control the formation of the nanostructures and the surrounding WL at the presence of a capping layer. Therefore, controlling the interaction between the floating layer and the capping layer would contribute in the formation of the WL and the nanostructures within. In a similar manner, the different interactions of 430^{o}C InAs cap and

InAs CCs to their corresponding Sb containing floating layers may have induced changes in the associated InSbAs regions. However, the aforementioned discussions could only establish a qualitative understanding of Sb segregation facilitated by their MEE growth and InAs cap growth temperatures. In order to obtain further information on Sb segregation, the corresponding Sb composition distribution needs be quantified which could be attained through quantitative TEM analyses.

The Sb induced compositional variations observed during 002 DF analyses can be quantified to a certain extent using the kinematical diffraction theory [107]. In this theory, it is considered that there is no interaction between the transmitted and the diffracted waves, and that the corresponding absorption effects are negligible. Additionally, the analyzing TEM specimen should be unattainably thin (~ 1 nm). However, plausible results associated to this theory have been achieved for reasonably thin experimental specimens [76,108] and hence, it has been considered for the Sb composition analysis from the 002 DF images in this Thesis. In terms of 430ºC sample, values of Sb composition in the range 5-10% have been measured in the InSbAs WL demonstrated in publication II, where an agglomerate contains a higher Sb composition. According to Beanland *et. al.* [109], kinematical approximation works well for a composition below 20%, where the electron scattering factors are roughly proportional to the corresponding atomic numbers of the existing materials. The obtained composition values are below 20%, therefore in the range of application of this model. A detailed observation of the obtained Sb profiles have shown asymmetric edges along the growth direction ([001]), where the interfaces between the overgrown InAs cap and the InSbAs WL are graded whereas the interfaces between the InSbAs WL and the InAs barrier are more abrupt. This graded upper interface indicates Sb segregation towards the growth direction, similar to the analyses observed in refs. [75-77]. In order to quantify the Sb composition with better spatial resolution, aberration corrected high resolution HAADF-STEM analyses have been performed to ensure precise Sb composition distribution.

The atomic column intensities in a HAADF-STEM image is roughly proportional to the average atomic number associated to the element(s) present in those atomic columns with power n ($I \alpha Z^n$), where n is varied within the range of 1.7-2. This means, in terms of an InAs/InSbAs/InAs heterostructure, the Sb/As containing columns would have higher HAADF-STEM intensities than pure As columns, since Sb has higher Z number than As. The

HAADF-STEM intensity also depends on specimen thickness [85,110]. Because of this, Sb-containing regions where the specimen thickness is smaller could show same intensity as InAs regions with larger thickness, therefore care should be taken with small thickness fluctuations in regions of small Sb content. A similar scenario has been observed in the experimental HAADF-STEM images associated to 430^{o}C sample in publication II. Here, the InSbAs WL could not be clearly distinguished from the InAs layers, suggesting either the presence of low Sb composition within the InSbAs WL or thicker InAs regions. In order to clearly identify the InSbAs layer, GPA analysis [68] was performed on the HAADF-STEM image. The GPA analysis functions with the position of HAADF-STEM atomic columns, not intensity and therefore, unaffected by local specimen thickness variation. The GPA analysis revealed the presence of Sb atoms in the InSbAs WL layer as it causes lattice displacement in InAs due to larger size. Here, the maximum lattice displacement was found to be 1% in the agglomerate, where for a 10% Sb as observed in 002 DF images the theoretical value would be 0.69%. This finding assures coherence between the 002 DF and the GPA results. In order to measure the Sb composition in the InSbAs layer, specimen thickness variations have been compensated during the HAADF-STEM analysis and, as a result, ML-by-ML maximum average of 10% Sb as similar to the aforementioned 002 DF analysis is found. It is worth noting that, similar to the Sb profiles obtained in 002 DF analysis, the ML-by-ML Sb profile from the HAADF-STEM image experiences graded interface between the InSbAs and upper InAs layer and hence, also indicates Sb segregation towards the growth direction ([001]).

In contrast to the HAADF-STEM image of 430^{o}C sample, it was easier to locate InSbAs WLs with few agglomerates through corresponding high intensity dumbbells in the HAADF-STEM images associated to the CC samples, due to larger Sb content. In order to quantify the intensities of these dumbbells, the original qHAADF tool [67] was initially used, where both ROI and reference regions exist in the same micrograph. This tool generates atomic dumbbell-by-dumbbell R values on the ROI with the help of Mask3. Afterwards, these R values reveal atomic column-by-column Sb composition (in %) using the method by Hernández-Maldonado *et. al.* [59]. However, in order to assure precise Sb quantification, the thickness variation between the ROI and reference regions needs to be compensated, discussed earlier. As a result, ZLP EELS analysis has been performed while acquiring each HAADF-STEM image in order to measure specimen thickness. The ZLP EELS revealed a

very low average thickness variation of < 1 nm between ROI and reference regions in either image. Therefore, to compensate this thickness variation, the aforementioned equation 3 has been applied during the qHAADF quantification to obtain more precise Sb induced R values. Afterwards, the Sb compositions are obtained with these corrected R values using the approach by Hernández-Maldonado *et. al.* [59]. The Sb compositional distribution in the HAADF-STEM images from either CC sample revealed that the corresponding agglomerates lack both the shapes of any QD (cylindrical, cuboid, pyramidal, etc. [12]) and size uniformity. In order to evaluate possible differences in the Sb content in the associated InSbAs WLs within the CC samples, a histogram was generated using several images from either CC sample that reveals the statistical analysis of Sb composition in atomic columns. According to the histogram, the 310ºC InAs CC sample has a larger number of atomic columns with Sb composition in the range 21-30% Sb, whereas the 380º InAs CC sample contains Sb in the range 11-20%. The comparative observation between the CC samples implies that the Sb composition increases in the InSbAs layer with decreasing InAs CC growth temperatures. Additionally, the analysis of individual agglomerates show that a higher ML-by-ML average Sb composition of 24% is found in the 310^{o}C sample in comparison to the value of 10% Sb associated to the 430^{o}C sample. This outcome quantitatively shows that an InAs CC influences the Sb incorporation within a InSbAs WL that eventually effects the corresponding PL responses.

Regarding the experimental values of Sb composition quantified by TEM in the present Thesis, it should be noted that these values are not the actual Sb composition in the observed clusters, but averages of Sb compositions along the whole specimen thickness. This is due to the fact that in TEM, images are the result of the projection of the features contained in the electron transparent specimen into a plane. In order to obtain a closer approximation to the actual Sb composition in the agglomerates, HAADF-STEM image simulation has been performed in this Thesis. The simulated images have been designed as InAs structures of 35 nm specimen thickness which incorporates a cubic InSbAs agglomerate of 5 nm at the middle of the InAs structure. In order to decide the Sb composition to be included in the simulations, some rough calculations have been performed in terms of simulated HAADF-STEM image intensity, $I=k*Z^{n}$, detailed in Publication II. The HAADF-STEM simulations performed have revealed that a single agglomeration with 45% Sb included in a InAs layer 35 nm thick is able

to generate an average intensity in the layer corresponding to an average Sb composition of ~ 10%, similar to the maximum average Sb composition measured experimentally in the agglomerate in the 430^{o}C sample. This observation assures the expectation of having a larger Sb composition in the InSbAs agglomerates than the average Sb composition measured in the experimental HAADF-STEM images, indicating that nanostructures more similar to QDs are likely present in the InSbAs WLs. Further simulations to implement a more precise analysis including the Sb composition of the WL, a variability in the agglomerate positions along the specimen thickness and the number of overlapping agglomerates are in progress. Extensive research should be performed in this regard to realize precise nanostructure formation induced by the corresponding growth steps. It should be mentioned that the projection effect that occurs in TEM is most relevant when analyzing individual nanostructures in a layer, as in the analysis of homogeneous regions the averaged values obtained often resemble the average composition of the layer. This is the case of the regions in the InSbAs layers where clusters are absent. In this sense, it is worth noting that, similar to the ML-by-ML Sb profile from the HAADF-STEM image of 430^{o}C sample, the 380º and 310^{o}C samples associated ML-by-ML Sb profiles also experiences a graded interface between the InSbAs and upper InAs layer, indicating the presence of Sb segregation towards the growth direction ([001]). Because of this, segregation in these samples will be analyzed next using the average values of composition obtained by HAADF-STEM.

In order to quantify the Sb segregation to analyze the effect of the CC in the Sb distribution, the widely used theoretical segregation model developed by Muraki *et. al.* [111] has been considered. The Muraki model has been widely used to quantify segregation in III-V QWs. For example, Sb segregation in InAs/InAs$_{1-x}$Sb$_x$ type-II superlattices [76] and GaInSb/InAs strained-layer superlattices [112], or In segregation in In$_x$Ga$_{1-x}$As/GaAs heterostructures [59,113] have been analyzed with the model. For segregation analysis on the aforementioned HAADF-STEM composition profiles, the maximum averages in a ML for samples 430º and 310ºC (10% and 24%, respectively) have been positioned at ML1 and so on and so forth. Afterwards, the corresponding Sb segregation in either sample has been quantified using the following equation:

$$x = x_0*(1 - S^N)*S^{z-N}, \text{ for } z \geq N \qquad (4)$$

Here, x is the average ML-by-ML Sb composition, x_0 is the nominal InSb composition, z is the number of analyzing MLs at ML≥0, S is the segregation coefficient and N is the nominal thickness of the InSb layer.

In terms of the 430^{o}C sample, the best fit between the experimental and Muraki model has been observed for a S value of 0.81 at a nominal InSb deposition thickness of 0.72 ML which is in good agreement with our XRD nominal deposition thickness value of 0.65 ML. On the other hand, in terms of the 310^{o}C sample, the best Muraki fit has been obtained with an S of 0.61 for a nominal InSb deposition thickness of 1.09 ML which is also in good agreement with the deposition thickness of 1.02 ML obtained in the XRD analysis. Here, the S value of 0.81 obtained from 430^{o}C sample has been found to be compatible to the segregation coefficient value of 0.82 measured by RHEED in SML InSb/InAs insertions grown at 430^{o}C [53,74]. Also, the low S value of 0.61 found in 310^{o}C sample is in good agreement with an S value of 0.59 obtained by extrapolating the RHEED data measured in the range 410-500ºC in the aforementioned references to the InSb growth temperature of 310ºC. The correlation of a high Sb composition in a ML in the 310^{o}C CC sample and a thick InSb deposition layer to the corresponding low S value indicates that CC growth temperature has a direct effect on the Sb incorporation and distribution during growth. In the literature, references on the effect of decreasing the cap layer growth temperature on the composition distribution of MEE nanostructures associated to SML deposition have not been found. However, the effect of the SL growth temperature in the Sb composition has previously been studied. It has been reported that the MEE grown SL that contains Sb MLs in (In, Ga, Al)As experiences an increased Sb incorporation in the material when the SL growth temperature is reduced [90]. This enhancement of Sb incorporation has been found to occur in the temperature range 465-400ºC, where a complete ML of InSb per period can be achieved at a growth temperature below 420°C. Moreover, Haugan *et. al.* [81] found a 14% increase in Sb composition in InAs/InAsSb SLs if the corresponding growth temperature is reduced from 440 to 400ºC which they attributed to low Sb segregation during InAsSb growth through group V exchange process. These observations are somewhat compatible to the effect of the InAs cap growth temperature on the Sb distribution in the present work as improved Sb incorporation (less Sb segregation) is observed in all cases while the corresponding growth temperatures are reduced. Moreover, since it was possible to obtain a complete InSb ML

thickness grown at a high 430ºC by reducing the InAs CC temperature to 310ºC, the importance of the cap layer growth conditions on the characteristics of the InSb layers is justified.

Our results have shown the strong effect of the MEE growth steps and InAs cap growth temperature on Sb segregation. However, other growth parameters also have some influence on the material segregation and associated atomistic processes, including flux rate and anion exchange [114,115], surface diffusion [116,117], surface relaxation/reconstruction that corroborates interface formation [112,118], etc. These observations indicate that the epitaxial growth is a complex procedure where various atomistic processes occur simultaneously. These atomistic processes may partially/completely change with slight alteration in the growth condition and hence, experimentally pinpointing the nature of these changes is quite complicated. Further work is needed in order to facilitate precise controlling of the morphology and compositional distribution of the promising InSb/InAs nanostructures analyzed, and in order to exploiting the potential advantages of the MEE growth technique.

Chapter 5

Conclusions

The results obtained in this Doctoral Thesis in terms of the morphological and compositional analyses of InSb/InAs novel functional nanostructures for MIR LED applications have allowed achieving the following conclusions:

- The development of a modified qHAADF tool facilitates compositional analysis of many complex ternary semiconductor heterostructures including the InSb/InAs nanostructures where locating an appropriate reference region of known composition in a single HAADF-STEM image is complicated. This modified tool obtains compositional information of the first HAADF-STEM image (ROI image) with the help of a second HAADF-STEM image used as the reference region. (Publication I)
- The compensation process of thickness variation between the ROI and reference regions as well as selecting the optimum Mask sizes are crucial in order to allow a precise Sb compositional determination within InSb/InAs heterostructures with both the original and the modified qHAADF tools. (Publication I)
- Single SML InSb insertion through MEE deposition of Sb on InAs substrate induce InSbAs regions with low Sb compositions and thicknesses of few nanometers after InAs capping, if same high substrate temperatue (>400^{o}C) is used during InAs cap growh and Sb deposition. The formed InSbAs region is constituted of scarce InSbAs agglomerates within a continuous InSbAs WL, instead of the independent QDs expected. This result has been correlated to a high growth temperature induced Sb segregation towards the [001] growth direction, and quantified through the theoretical Muraki model. (Publication II)
- Care should be taken in the quantification of the Sb composition in InSbAs clusters by TEM techniques when they are embedded in a InSbAs WL, as the projection effect produces an averaging of the composition values along the specimen thickness. Simulated HAADF-STEM images have demonstrated that the InSbAs agglomerates observed may contain larger Sb composition than the average Sb composition measured in the experimental HAADF-STEM images, up to ~ 45% Sb. This observation indicates that although independent QDs have not been found in the layer, Sb clusters that may be the seed of future QDs are present in the InSbAs WLs. (Publication II)

- The use of InAs CCs have been found to modify the Sb distribution in InSb/InAs heterostructures obtained by MEE. A reduction in the Sb segregation in the InSbAs layer has been realized which leads to higher Sb composition within the InSbAs agglomerates. This CC contributed modifications on Sb distribution have been found to tune the PL response of the corresponding InSb layers in the MIR range. Further work is needed to exploit the potential advantages of the MEE growth technique for obtaining controllable size QDs without WL. (Publication III)

Chapter 6

Prospects

LED lighting is considered to be the superior lighting technology in comparison to its other two counterparts: incandescent light bulbs and compact fluorescent lights (CFL). Among these three lighting technologies, the LED and CFL lighting technologies are in competition to be the principle candidate of future lighting industry. In comparison, the LEDs are cleaner, more energy efficient and possesses longer lifetime over CFL, where the CFL contains poisonous mercury content. However, currently LEDs are slightly more expensive than CFL, although they are expected to approximately match the cost of CFL by the year 2020 [119]. Because of the unique properties of LED lighting, they are considered in various advanced applications. For example, the use of LEDs could offer efficient indoor horticulture [120] and match human circadian rhythm [121], thanks to their dynamic features and spectral design flexibility. These conventional LEDs can be replaced by micro-LEDS in terms of optogenetics application [122] and the advanced Li-Fi (light fidelity) technology [123] (considered as the future of wireless communication), achieving data transmit rate over 10 Gbps [124], which is much higher than the data transmit rate of current Wi-Fi (wireless fidelity) technology of 150 Mbps [123]. As a result, this Li-Fi technology could be used to design highly functional single systems that combine information displays, lighting and high BW communication, opening the possibility to design advanced smart homes, vehicles, healthcare and security systems, etc.

The above mentioned smart homes will likely include systems to monitor the indoor air quality through efficient sensing technology. Undesirable gases with MIR signatures, such as volatile organic compounds (VOC), CO_2, CO, etc, could be detected through MIR LED sensors. As a result, MIR sensors are becoming more and more desirable in these emerging smart living and working spaces. MIR LED sensors can also be used to monitor the concentration of CH_4 gas in the environment which plays a principle role in global warming. In order to detect small CH_4 gas leaks and flow rate in the well pads, Methane Observation Networks with Innovative Technology to Obtain Reductions (MONITOR) program has been developed in the United States that allocates US$3000 annual funds to a dozen of technologies [125]. In such a scenario, battery-operated, low cost MIR LED sensors could certainly be a front runner meeting these sensing needs. Low cost MIR LEDs may also be used in non-invasive medical applications. For instance, integration of MIR LEDs in smartphones and wearable devices could facilitate measuring blood glucose of diabetic

patients at a lower cost in oppose to comparatively expensive MIR quantum-cascade laser (QCL) [126].

The active layer of the aforementioned MIR LEDs may contain MEE grown InSb QDs as discussed in this Thesis. Typically, the growth success of these InSb QDs depends on various growth conditions during MEE growth, which include substrate temperature [47,49], annealing stage [34], type of group V flux [48], GI period [53], etc. Moreover, presently it is even possible to grow III-V MEE QDs on selective locations on the III-V substrate [127] using selective area epitaxy (SAE) [128], which seems to influence the physical and optical characteristics of these QDs. The combination of SAE and MEE with SML insertion of InSb on InAs substrate may facilitate forming InSbAs QDs with no/thin WL underneath which could open the possibility to design arrays of high performance LEDs at MIR range for integrated photonics applications. On the other hand, it has been recently demonstrated that low temperature and extremely low growth rate during CE growth of InSb layer with WL thickness > 2 ML on InAs induces defect-free InSb/InAs quantum nanostripes, i.e., elongated QDs along [110] direction [129,130]. Similar to MEE grown InSb/InAs QDs, the aforementioned unique CE growth technique allows the InSb/InAs quantum nanostripes to emit light at MIR range in RT, contrasting the analysis observed in ref. [32].

In order to realize the influence of various growth parameters on the formation of the MEE/CE grown InSb/InAs QDs, their morphology and composition must be analyzed with high spatial resolution. For this, revolutionary (S)TEM techniques play a special role which is now heading to 3D analyses. For instance, a new EDX detection system has recently been developed [131] which facilitates quantitative chemical analysis of semiconductors materials in 3D. In order to induce further development of the spatial resolution of the (S)TEM images, continuous research are being performed to develop the aberration correctors of these TEM machines [132,133]. In addition to this, advanced research is also being performed to obtain superior image simulation techniques to assist in image analysis [134,135], improved sample holder [132], optimized TEM specimen preparation technique [136], high performance detectors [131,132,137], etc. Such continuous improvements would likely open the pathways to even more precise structural and compositional analyses that will escalate the development of advanced nanostructures and devices.

References

[1] Holonyak N and Bevacqua S F 1962 Coherent (visible) light emission from Ga($As_{1-x}P_x$) junctions *Appl. Phys. Lett.* **1** 82–3

[2] Nathan M I, Dumke W P, Burns G, Dill F H and Lasher G 1962 Stimulated emission of radiation from GaAs p-n junctions *Appl. Phys. Lett.* **1** 62–4

[3] Hall R N, Fenner G E, Kingsley J D, Soltys T J and Carlson R O 1962 Coherent light emission from GaAs junctions *Phys. Rev. Lett.* **9** 366–8

[4] Nelson H 1963 Epitaxial growth from the liquid state and its application to the fabrication of tunnel and lasar diodes *RCA Rev.* **24** 603–15

[5] Alferov Z I, Andreev V M, Garbuzov D Z, Zhilyaev Y V, Morozov E P, Portnoi E L and Trofim V G 1971 Investigation of the influence of the AlAs-GaAs heterostructure parameters on the laser threshold current and the realization of continuous emission at room temperature *Sov. Phys. Semicond* **4** 1573–5

[6] Cho A Y, Panish M B and Hayashi I 1971 Molecular beam epitaxy of GaAs, AlGaAs and GaP *3rd Int. Symp. Gall. Arsenide Relat. Compd.* 18–29

[7] Manasevit H M 1968 Single-crystal gallium arsenide on insulating substrates *Appl. Phys. Lett.* **12** 156–9

[8] Manasevit H M and Simpson W I 1969 The Use of Metal-Organics in the Preparation of Semiconductor Materials I. Epitaxial Gallium-V Compounds *J. Electrochem. Soc.* **116** 1725–32

[9] Valdueza-Felip S 2011 PhD Thesis: Nitride-based semiconductor nanostructures for applications in optical communications at 1.5 um

[10] Alferov Z I 2001 Nobel Lecture: The double heterostructure concept and its applications in physics, electronics, and technology *Rev. Mod. Phys.* **73** 767

[11] Kroemer H 2001 Nobel Lecture: Quasi-Electric Fields and Band Offsets: Teaching Electrons New Tricks *ChemPhysChem* **2** 490–9

[12] Ngo C Y, Yoon S F, Fan W J and Chua S J 2006 Effects of size and shape on electronic states of quantum dots *Phys. Rev. B* **74** 245331

[13] Edvinsson T 2018 Optical quantum confinement and photocatalytic properties in two-, one-and zero-dimensional nanostructures *R. Soc. open Sci.* **5** 180387

[14] Klyuev A V and Yakimov A V 2014 1/f Noise in GaAs nanoscale light-emitting structures *Phys. B Condens. Matter* **440** 145–51

[15] Wierer Jr J J, Tansu N, Fischer A J and Tsao J Y 2016 III-nitride quantum dots for ultra-efficient solid-state lighting *Laser Photon. Rev.* **10** 612–22

[16] Asada M, Miyamoto Y and Suematsu Y 1986 Gain and the Threshold of Three-Dimensional Quantum-Box Lasers *IEEE J. Quantum Electron.* **22** 1915–21

[17] Arakawa Y and Sakaki H 1982 Multidimensional quantum well laser and temperature dependence of its threshold current *Appl. Phys. Lett.* **40** 939–41

[18] Bhattacharya P, Mi Z, Yang J, Basu D and Saha D 2009 Quantum dot lasers: from promise to high-performance devices *J. Cryst. Growth* **311** 1625–31

[19] Coleman J J, Young J D and Garg A 2010 Semiconductor quantum dot lasers: a tutorial *J. Light. Technol.* **29** 499–510

[20] Ledentsov N N 2010 Quantum dot laser *Semicond. Sci. Technol.* **26** 14001

[21] Lee A D, Jiang Q, Tang M, Zhang Y, Seeds A J and Liu H 2013 InAs/GaAs quantum-dot lasers monolithically grown on Si, Ge, and Ge-on-Si substrates *IEEE J. Sel. Top. Quantum Electron.* **19** 1901107

[22] Liu A Y, Zhang C, Norman J, Snyder A, Lubyshev D, Fastenau J M, Liu A W K, Gossard A C and Bowers J E 2014 High performance continuous wave 1.3 μ m quantum dot lasers on silicon *Appl. Phys. Lett.* **104** 41104

[23] Krishna S, Gunapala S D, Bandara S V, Hill C and Ting D Z 2007 Quantum dot based infrared focal plane arrays *Proc. IEEE* **95** 1838–52

[24] Martyniuk P and Rogalski A 2008 Quantum-dot infrared photodetectors: Status and outlook *Prog. Quantum Electron.* **32** 89–120

[25] Barve A V, Montaya J, Sharma Y, Rotter T, Shao J, Jang W-Y, Meesala S, Lee S J and Krishna S 2011 High temperature operation of quantum dots-in-a-well infrared photodetectors *Infrared Phys. Technol.* **54** 215–9

[26] Henneberger F and Benson O 2016 Semiconductor quantum bits (CRC Press)

[27] Michler P, Kiraz A, Becher C, Schoenfeld W V, Petroff P M, Zhang L, Hu E and Imamoglu A 2000 A quantum dot single-photon turnstile device *Sci.* **290** 2282–5

[28] Buckley S, Rivoire K and Vučković J 2012 Engineered quantum dot single-photon sources *Reports Prog. Phys.* **75** 126503

[29] Li A 2003 Interaction of Nanoparticles with Radiation *ASP Conf. Ser.* **000**

[30] Bennett B R, Shanabrook B V., Thibado P M, Whitman L J and Magno R 1997 Stranski-Krastanov growth of InSb, GaSb, and AlSb on GaAs: Structure of the wetting layers *J. Cryst. Growth* **175**–**176** 888–93

[31] Yamaguchi K, Yujobo K and Kaizu T 2000 Stranski-Krastanov growth of InAs quantum dots with narrow size distribution *Jpn. J. Appl. Phys.* **39** L1245

[32] Karim A, Gustafsson O, Hussain L, Wang Q, Noharet B, Hammar M, Anderson J and Song J 2012 Characterization of InSb QDs grown on InAs (100) substrate by MBE and MOVPE *Opt. Sens. Detect. II* **8439** 84391J

[33] Mahajan S 1997 Defects in epitaxial layers of compound semiconductors grown by OMVPE and MBE techniques *Prog. Mater. Sci.* **42** 341–55

[34] Zhuang Q, Carrington P J and Krier A 2008 Growth optimization of self-organized InSb/InAs quantum dots *J. Phys. D. Appl. Phys.* **41**

[35] Song J D, Park Y M, Shin J C, Lim J G, Park Y J, Choi W J, Han I K, Lee J I, Kim H S and Park C G 2004 Influence of arsenic during/indium deposition on the formation of the wetting layers of InAs quantum dots grown by migration enhanced epitaxy *J. Appl. Phys.* **96** 4122–5

[36] Matthews D R, Summers H D, Smowton P M and Hopkinson M 2002 Experimental investigation of the effect of wetting-layer states on the gain–current characteristic of quantum-dot lasers *Appl. Phys. Lett.* **81** 4904–6

[37] Horikoshi Y, Kawashima M and Yamaguchi H 1986 Low-temperature growth of gaas and aias-gaas quantum-well layers by modified molecular beam epitaxy *Jpn. J. Appl. Phys.* **25** L868–70

[38] Cirlin G E, Petrov V N, Dubrovskii V G, Golubok A O, Tipissev S Y, Guryanov G M, Maximov M V, Ledentsov N N and Bimberg D 1997 Direct formation of InGaAs/GaAs quantum dots during submonolayer epitaxies from molecular beams *Czechoslov. J. Phys.* **47** 379–84

[39] Cho N K, Ryu S P, Song J D, Choi W J, Lee J I and Jeon H 2006 Comparison of structural and optical properties of InAs quantum dots grown by migration-enhanced molecular-beam epitaxy and conventional molecular-beam epitaxy *Appl. Phys. Lett.* **88** 2004–7

[40] Dayeh S A, Aplin D P R, Zhou X, Yu P K L, Yu E T and Wang D 2007 High electron mobility InAs nanowire field-effect transistors *Small* **3** 326–32

[41] Ford A C, Ho J C, Chueh Y-L, Tseng Y-C, Fan Z, Guo J, Bokor J and Javey A 2008 Diameter-dependent electron mobility of InAs nanowires *Nano Lett.* **9** 360–5

[42] Thelander C, Björk M T, Larsson M W, Hansen A E, Wallenberg L R and Samuelson L 2004 Electron transport in InAs nanowires and heterostructure nanowire devices *Solid State Commun.* **131** 573–9

[43] Caroff P, Wagner J B, Dick K A, Nilsson H A, Jeppsson M, Deppert K, Samuelson L, Wallenberg L R and Wernersson L 2008 High-quality InAs/InSb nanowire heterostructures grown by metal–organic vapor-phase epitaxy *Small* **4** 878–82

[44] Wang Y, Chi J, Banerjee K, Grützmacher D, Schäpers T and Lu J G 2011 Field effect transistor based on single crystalline InSb nanowire *J. Mater. Chem.* **21** 2459–62

[45] Nilsson H A, Deng M T, Caroff P, Thelander C, Samuelson L, Wernersson L E and Xu H Q 2011 InSb nanowire field-effect transistors and quantum-dot devices *IEEE J. Sel. Top. Quantum Electron.* **17** 907–14

[46] Mingo N 2004 Thermoelectric figure of merit and maximum power factor in III–V semiconductor nanowires *Appl. Phys. Lett.* **84** 2652–4

[47] Solov'ev V A, Lyublinskaya O G, Semenov A N, Meltser B Y, Solnyshkov D D, Terent'Ev Y V., Prokopova L A, Toropov A A, Ivanov S V. and Kop'Ev P S 2005 Room-temperature 3.9-4.3 μm photoluminescence from InSb submonolayers grown by molecular beam epitaxy in an InAs matrix *Appl. Phys. Lett.* **86** 3–6

[48] Carrington P J, Solov'ev V A, Zhuang Q, Ivanov S V. and Krier A 2008 Type II InSb/InAs quantum dot structures grown by molecular beam epitaxy using Sb 2 and As 2 fluxes *Quantum Sens. Nanophotonic Devices V* **6900** 69000I

[49] Ivanov S V., Semenov A N, Solov'ev V A, Lyublinskaya O G, Terent'ev Y V., Meltser B Y, Prokopova L G, Sitnikova A A, Usikova A A, Toropov A A and Kop'ev P S 2005 Molecular beam epitaxy of type II InSb/InAs nanostructures with InSb sub-monolayers *J. Cryst. Growth* **278** 72–7

[50] Lyublinskaya O G, Solov'ev V A, Semenov A N, Meltser B Y, Terent'ev Y V., Prokopova L A, Toropov A A, Sitnikova A A, Rykhova O V., Ivanov S V., Thonke K and Sauer R 2006 Temperature-dependent photoluminescence from type-II InSb/InAs quantum dots *J. Appl. Phys.* **99** 0–6

[51] Toropov A A, Moiseeva M M, Ivanov S V, Magnusson B and Monemar B 2001 Photoluminescence and atomic force microscopy studies of InAs/InSb nanostructures grown by MBE *SPRINGER Proc. Phys.* **87** 401–2

[52] Yeap G H, Rybchenko S I, Itskevich I E and Haywood S K 2009 Type-II InAs x Sb 1− x/InAs quantum dots for midinfrared applications: Effect of morphology and composition on electronic and optical properties *Phys. Rev. B* **79** 75305

[53] Semenov A N, Lyublinskaya O G, Solov'Ev V A, Mel'Tser B Y and Ivanov S V. 2008 In situ study of the formation kinetics of InSb quantum dots grown in an InAs(Sb) matrix *Semiconductors* **42** 74–9

[54] Ryu S P, Cho N K, Lim J Y, Rim A R, Choi W J, Song J D, Lee J Il and Lee Y T 2009 Effect of growth interruption in migration enhanced epitaxy on InAs/GaAs quantum dots *Jpn. J. Appl. Phys.* **48** 0911031–4

[55] Hodgson P D, Bentley M, Delli E, Beanland R, Wagener M C, Botha J R and Carrington P J 2018 Optical and structural properties of InGaSb/GaAs quantum dots grown by molecular beam epitaxy *Semicond. Sci. Technol.* **33** 125021

[56] Cahay M, Leburton J P, Lockwood D J, Bandyopadhyay S and Harris J S (eds.) 2001 Quantum confinement VI: Nanostructured materials and devices: Proceedings of the International Symposium *Electrochem. Soc.* **2001-19**

[57] Ruska E 1987 The development of the electron microscope and of electron microscopy *Rev. Mod. Phys.* **59** 627

[58] Rose H H 2009 Historical aspects of aberration correction *J. Electron Microsc. (Tokyo).* **58** 77–85

[59] Hernández-Maldonado D, Herrera M, Alonso-González P, González Y, González L, Gazquez J, Varela M, Pennycook S J, Guerrero-Lebrero M D L P, Pizarro J, Galindo P L and Molina S I 2011 Compositional analysis with atomic column spatial resolution by 5th-order aberration-corrected scanning transmission electron microscopy *Microsc. Microanal.* **17** 578–81

[60] Ponce F A, Cherns D, Young W T and Steeds J W 1996 Characterization of dislocations in GaN by transmission electron diffraction and microscopy techniques *Appl. Phys. Lett.* **69** 770–2

[61] Howie A and Whelan M J 1961 Diffraction contrast of electron microscope images of crystal lattice defects-II. The development of a dynamical theory *Proc. R. Soc. London. Ser. A. Math. Phys. Sci.* **263** 217–37

[62] Lemaître A, Patriarche G and Glas F 2004 Composition profiling of In As⁄ Ga As quantum dots *Appl. Phys. Lett.* **85** 3717–9

[63] Bithell E G and Stobbs W M 1991 III-V ternary semiconductor heterostructures: The choice of an appropriate compositional analysis technique *J. Appl. Phys.* **69** 2149–55

[64] Wen C and Ma Y J 2018 Determination of atomic-scale chemical composition at semiconductor heteroepitaxial interfaces by high-resolution transmission electron microscopy *Micron* **106** 48–58

[65] Sartori D R, Dell'Arciprete M L, Magnacca G, Calza P, Laurenti E and Gonzalez M C 2018 Multi-walled carbon nanotubes photochemistry: A mechanistic view of the effect of impurities and oxygen-containing surface groups *Carbon N. Y.* **138** 161–8

[66] Martinez G T, Rosenauer A, De Backer A, Verbeeck J and Van Aert S 2014 Quantitative composition determination at the atomic level using model-based high-angle annular dark field scanning transmission electron microscopy *Ultramicroscopy* **137** 12–9

[67] Molina S I, Sales D L, Galindo P L, Fuster D, González Y, Alén B, González L, Varela M and Pennycook S J 2009 Column-by-column compositional mapping by Z-contrast imaging *Ultramicroscopy* **109** 172–6

[68] Hÿtch M J 1997 Geometric phase analysis of HREM images *Scanning Microsc.* **11** 53–66

[69] Fernández-Delgado N, Herrera M, Chisholm M F, Kamarudin M A, Zhuang Q D, Hayne M and Molina S I 2016 Atomic-column scanning transmission electron microscopy analysis of misfit dislocations in GaSb/GaAs quantum dots *J. Mater. Sci.* **51** 7691–8

[70] de la Mata M, Magén C, Caroff P and Arbiol J 2014 Atomic scale strain relaxation in axial semiconductor III–V nanowire heterostructures *Nano Lett.* **14** 6614–20

[71] Galindo P L, Kret S, Sanchez A M, Laval J Y, Yáñez A, Pizarro J, Guerrero E, Ben T and Molina S I 2007 The Peak Pairs algorithm for strain mapping from HRTEM images *Ultramicroscopy* **107** 1186–93

[72] Neave J H, Dobson P J, Joyce B A and Zhang J 1985 Reflection high-energy electron diffraction oscillations from vicinal surfaces—a new approach to surface diffusion measurements *Appl. Phys. Lett.* **47** 100–2

[73] Hatami F, Kim S M, Yuen H B and Harris J S 2006 InSb and InSb:N multiple quantum dots *Appl. Phys. Lett.* **89** 1–4

[74] Semenov A, Lyublinskaya O G, Solov'ev V A, Meltser B Y and Ivanov S V. 2007 Surface segregation of Sb atoms during molecular-beam epitaxy of InSb quantum dots in an InAs(Sb) matrix *J. Cryst. Growth* **301**–**302** 58–61

[75] Molina S I, Beltrán A M, Ben T, Galindo P L, Guerrero E, Taboada A G, Ripalda J M and Chisholm M F 2009 High resolution electron microscopy of GaAs capped GaSb nanostructures *Appl. Phys. Lett.* **94**

[76] Lu J, Luna E, Aoki T, Steenbergen E H, Zhang Y H and Smith D J 2016 Evaluation of antimony segregation in InAs/$InAs_{1-x}Sb_x$ type-II superlattices grown by molecular beam epitaxy *J. Appl. Phys.* **119**

[77] Luna E, Satpati B, Rodriguez J B, Baranov A N, Tourníe and Trampert A 2010 Interfacial intermixing in InAs/GaSb short-period-superlattices grown by molecular beam epitaxy *Appl. Phys. Lett.* **96** 34–7

[78] Yurasov D V., Drozdov M N, Murel A V., Shaleev M V., Zakharov N D and Novikov A V. 2011 Usage of antimony segregation for selective doping of Si in molecular beam epitaxy *J. Appl. Phys.* **109**

[79] Antonov A V, Drozdov M N, Novikov A V and Yurasov D V 2015 Segregation of Sb in Ge epitaxial layers and its usage for the selective doping of Ge-based structures *Semiconductors* **49** 1405–9

[80] Shen X M, Li H, Liu S, Smith D J and Zhang Y H 2013 Study of InAs/InAsSb type-II superlattices using high-resolution x-ray diffraction and cross-sectional electron microscopy *J. Cryst. Growth* **381** 1–5

[81] Haugan H J, Brown G J and Peoples J A 2017 On the study of antimony incorporation in InAs/InAsSb superlattices for infrared sensing *J. Vac. Sci. Technol. B, Nanotechnol. Microelectron: Mater. Process. Meas. Phenom.* **35** 02B107

[82] Ye H, Li L, Hinkey R T, Yang R Q, Mishima T D, Keay J C, Santos M B and Johnson M B 2013 MBE growth optimization of InAs (001) homoepitaxy *J. Vac. Sci. Technol. B.* **31** 03C135

[83] Carrington P J, Repiso E, Lu Q, Fujita H, Marshall A R J, Zhuang Q and Krier A 2016 InSb-based quantum dot nanostructures for mid-infrared photonic devices *Nanophotonic Mater. XIII* **9919** 99190C

[84] Müller-Caspary K, Oppermann O, Grieb T, Krause F F, Rosenauer A, Schowalter M, Mehrtens T, Beyer A, Volz K and Potapov P 2016 Materials characterisation by angle-resolved scanning transmission electron microscopy *Sci. Rep.* **6** 1–9

[85] Rosenauer A, Gries K, Müller K, Pretorius A, Schowalter M, Avramescu A, Engl K and Lutgen S 2009 Measurement of specimen thickness and composition in $Al_xGa_{1-x}N$ / GaN using high-angle annular dark field images *Ultramicroscopy* **109** 1171–82

[86] Lebeau J M, Findlay S D, Allen L J and Stemmer S 2008 Quantitative atomic resolution scanning transmission electron microscopy *Phys. Rev. Lett.* **100** 1–4

[87] LeBeau J M, Findlay S D, Wang X, Jacobson A J, Allen L J and Stemmer S 2009 High-angle scattering of fast electrons from crystals containing heavy elements: Simulation and experiment *Phys. Rev. B* **79** 214110

[88] Reyes D F, González D, Ulloa J M, Sales D L, Dominguez L, Mayoral A and Hierro A 2012 Impact of N on the atomic-scale Sb distribution in quaternary GaAsSbN-capped InAs quantum dots *Nanoscale Res. Lett.* **7** 1–7

[89] Reyes D F, Ulloa J M, Guzman A, Hierro A, Sales D L, Beanland R, Sanchez A M and González D 2015 Effect of annealing in the Sb and In distribution of type II GaAsSb-capped InAs quantum dots *Semicond. Sci. Technol.* **30** 114006

[90] Bennett B R, Shanabrook B V. and Twigg M E 1999 Anion control in molecular beam epitaxy of mixed As/Sb III-V heterostructures *J. Appl. Phys.* **85** 2157–61

[91] Allen L J, Findlay S D, Oxley M P and Rossouw C J 2003 Lattice-resolution contrast from a focused coherent electron probe. Part I *Ultramicroscopy* **96** 47–63

[92] Baladés N, Herrera M, Sales D L, Guerrero M P, Guerrero E, Galindo P L and Molina S I 2019 Influence of the crosstalk on the intensity of HAADF-STEM images of quaternary semiconductor materials *J. Microsc.* **273** 81–8

[93] E H, MacArthur K E, Pennycook T J, Okunishi E, D'Alfonso A J, Lugg N R, Allen L J and Nellist P D 2013 Probe integrated scattering cross sections in the analysis of atomic resolution HAADF STEM images *Ultramicroscopy* **133** 109–19

[94] MacArthur K E, D'Alfonso A J, Ozkaya D, Allen L J and Nellist P D 2015 Optimal ADF STEM imaging parameters for tilt-robust image quantification *Ultramicroscopy* **156** 1–8

[95] Martinez G T, De Backer A, Rosenauer A, Verbeeck J and Van Aert S 2014 The effect of probe inaccuracies on the quantitative model-based analysis of high angle annular dark field scanning transmission electron microscopy images *Micron* **63** 57–63

[96] Jones L and Nellist P D 2013 Identifying and correcting scan noise and drift in the scanning transmission electron microscope *Microsc. Microanal.* **19** 1050–60

[97] Aurenhammer F 1991 Voronoi diagrams---a survey of a fundamental geometric data structure *ACM Comput. Surv.* **23** 345–405

[98] Jones L 2016 Quantitative ADF STEM: Acquisition, analysis and interpretation *IOP Conf. Ser. Mater. Sci. Eng.* **109**

[99] Ripalda J M, Alonso-Álvarez D, Alén B, Taboada A G, García J M, González Y and González L 2007 Enhancement of the room temperature luminescence of InAs quantum dots by GaSb capping *Appl. Phys. Lett.* **91** 1–4

[100] Guimard D, Tsukamoto S, Nishioka M and Arakawa Y 2006 Emission at 1.55 μm from InAs/GaAs quantum dots grown by metal organic chemical vapor deposition via antimony incorporation *Phys. Status Solidi Curr. Top. Solid State Phys.* **3** 4023–6

[101] McLean D 1957 Grain Boundaries in Metals (Oxford University Press)

[102] Magri R and Zunger A 2002 Effects of interfacial atomic segregation and intermixing on the electronic properties of InAs/GaSb superlattices *Phys. Rev. B* **65** 165302

[103] Yano M, Seki Y, Ohkawa H, Koike K, Sasa S and Inoue M 1998 Characteristics of self-assembled InSb dots grown on (100) AlGaSb by molecular beam epitaxy *Jpn. J. Appl. Phys.* **37** 2455

[104] Martini S, Quivy A A, Lamas T E, Da Silva M J, Da Silva E C F and Leite J R 2003 Influence of indium segregation on the RHEED oscillations during the growth of InGaAs layers on a GaAs (001) surface *J. Cryst. Growth* **251** 101–5

[105] Kaspi R 1999 Compositional abruptness at the InAs-on-GaSb interface: optimizing growth by using the Sb desorption signature *J. Cryst. Growth* **201** 864–7

[106] Kaspi R and Evans K R 1997 Sb-surface segregation and the control of compositional abruptness at the GaAsSbGaAs interface *J. Cryst. Growth* **175** 838–43

[107] Amelinckx S 1972 The geometry and interfaces due to ordering and their observation in transmission electron microscopy and electron diffraction *Surf. Sci.* **31** 296–354

[108] Sanchez A M, Beltran A M, Beanland R, Ben T, Gass M H, De La Pẽa F, Walls M, Taboada A G, Ripalda J M and Molina S I 2010 Blocking of indium incorporation by antimony in III-V-Sb nanostructures *Nanotechnology* **21**

[109] Beanland R 2005 Dark field transmission electron microscope images of III-V quantum dot structures *Ultramicroscopy* **102** 115–25

[110] Van den Broek W, Rosenauer A, Goris B, Martinez G T, Bals S, Van Aert S and Van Dyck D 2012 Correction of non-linear thickness effects in HAADF STEM electron tomography *Ultramicroscopy* **116** 8–12

[111] Muraki K, Fukatsu S, Shiraki Y and Ito R 1992 Surface segregation of in atoms during molecular beam epitaxy and its influence on the energy levels in InGaAs/GaAs quantum wells *Appl. Phys. Lett.* **61** 557–9

[112] Steinshnider J, Harper J, Weimer M, Lin C-H, Pei S S and Chow D H 2000 Origin of antimony segregation in GaInSb/InAs strained-layer superlattices *Phys. Rev. Lett.* **85** 4562

[113] Pelá R R, Teles L K, Marques M and Martini S 2013 Theoretical study of the indium incorporation into III-V compounds revisited: The role of indium segregation and desorption *J. Appl. Phys.* **113**

[114] Dehaese O, Wallart X and Mollot F 1995 Kinetic model of element III segregation during molecular beam epitaxy of III-III'-V semiconductor compounds *Appl. Phys. Lett.* **66** 52–4

[115] Millunchick J M, Anderson E M, Pearson C, Sarney W L and Svensson S P 2013 Incorporation kinetics in mixed anion compound semiconductor alloys *J. Appl. Phys.* **114** 1–6

[116] Godbey D J and Ancona M G 1997 Modeling of Ge segregation in the limits of zero and infinite surface diffusion *J. Vac. Sci. Technol. A* **15** 976–80

[117] Haxha V, Drouzas I, Ulloa J M, Bozkurt M, Koenraad P M, Mowbray D J, Liu H Y, Steer M J, Hopkinson M and Migliorato M A 2009 Role of segregation in InAs/GaAs quantum dot structures capped with a GaAsSb strain-reduction layer *Phys. Rev. B* **80** 165334

[118] Anderson E M and Millunchick J M 2018 The atomistic mechanism for Sb segregation and As displacement of Sb in InSb(001) surfaces *Surf. Sci.* **667** 45–53

[119] Outlook A E 2014 Early Release Overview *US Energy Inf. Adm.*

[120] Mitchell C A, Both A-J, Bourget C M, Burr J F, Kubota C, Lopez R G, Morrow R C and Runkle E S 2012 LEDs: The future of greenhouse lighting! *Chron. Horticult.* **52** 6–12

[121] Blume C, Garbazza C and Spitschan M 2019 Effects of light on human circadian rhythms, sleep and mood Auswirkungen von Licht auf zirkadiane Rhythmen, Schlaf und die Stimmung bei Menschen *Somnologie* **23** 147–56

[122] McAlinden N, Cheng Y, Scharf R, Xie E, Gu E, Reiche C F, Sharma R, Tathireddy P, Dawson M D, Rieth L, Blair S and Mathieson K 2019 Multisite microLED optrode array for neural interfacing *Neurophotonics* **6** 1

[123] Chaudhuri R R, Dutta K and Saha A I 2015 Review on Li-Fi Technology in Advances in optical science and engineering *Springer Proc. Phys.* **166** 479–85

[124] Zhu D and Humphreys C J 2016 Solid-State Lighting Based on Light Emitting Diode Technology *Optics in Our Time* (Springer, Cham) pp 87–118

[125] Patel P 2017 Monitoring methane: Low-cost sensors could help natural gas producers plug costly methane leaks *ACS Cent. Sci.* **3** 679-82

[126] Matsuura Y and Koyama T 2019 Non-invasive blood glucose measurement using quantum cascade lasers *Quantum Sens. Nano Electronics and Photonics XVI* **10926** 1092606

[127] Horikoshi Y 2019 Migration-enhanced epitaxy and its applications in Molecular beam epitaxy: materials and applications for electronics and optoelectronics 1st edn (John Wiley & Sons) p. 41.

[128] Mokkapati S, Lever P, Tan H H, Jagadish C, McBean K E and Phillips M R 2005 Controlling the properties of InGaAs quantum dots by selective-area epitaxy *Appl. Phys. Lett.* **86** 1–3

[129] Srisinsuphya P, Rongrueangkul K, Khanchaitham R, Thainoi S, Kiravittaya S, Nuntawong N, Sopitpan S, Yordsri V, Thanachayanont C, Kanjanachuchai S, Ratanathammaphan S, Tandaechanurat A and Panyakeow S 2019 InSb/InAs quantum nano-stripes grown by molecular beam epitaxy and its photoluminescence at mid-infrared wavelength *J. Cryst. Growth* **514** 36–9

[130] Rongrueangkul K, Srisinsuphya P, Thainoi S, Kiravittaya S, Nuntawong N, Thornyanadacha N, Sopitpan S, Yordsri V, Thanachayanont C, Kanjanachuchai S, Ratanathammaphan S, Tandaechanurat A and Panyakeow S 2019 Investigation of the

Morphology of InSb/InAs Quantum Nanostripe Grown by Molecular Beam Epitaxy *Phys. Status Solidi* **1900374**

[131] Aoyama Y, Ohnishi I, Endo N, Okunishi E, Sasaki T, Iwasawa Y and Kondo Y 2018 Structural Analysis of Semiconductor Devices by Using STEM/EDS Tomography *JEOL News* **53** 43-7

[132] Ohnishi I, Suzuki T, Miyatake K, Jimbo Y, Iwasawa Y, Morita M, Sasaki T, Sawada H and Okunishi E 2018 Analytical and in situ applications using aberration corrected scanning transmission electron microscope *e-Journal Surf. Sci. Nanotechnol.* **16** 286–8

[133] Rose H, Nejati A and Mueller H 2019 Magnetic Cc/Cs-corrector compensating for the chromatic aberration and the spherical aberration of electron lenses *Ultramicroscopy* **203** 139–44

[134] Krause F F, Bredemeier D, Schowalter M, Mehrtens T, Grieb T and Rosenauer A 2018 Using molecular dynamics for multislice TEM simulation of thermal diffuse scattering in AlGaN *Ultramicroscopy* **189** 124–35

[135] Wu W and Schäublin R 2018 Simulations of weak-beam diffraction contrast images of dislocation loops by the many-beam Schaeublin–Stadelmann equations *J. Mater. Sci.* **53** 15694–702

[136] Canavan M, Daly D, Rummel A, McCarthy E K, McAuley C and Nicolosi V 2018 Novel in-situ lamella fabrication technique for in-situ TEM *Ultramicroscopy* **190** 21–9

[137] Nellist P D and Martinez G T 2018 Fast Pixelated Detectors: A New Era for STEM *JEOL News* **53** 2-7

Appendices

In this section of the Thesis, Appendix I contains the list of the participated congresses/workshops during this PhD Thesis. Afterward, in Appendix II, the publications which are part of this *Thesis by Compendium of Publications* are included.

Appendix I

Congresses

- Atif A. Khan, M. Herrera, J. Pizarro, P. L. Galindo, E. R. Menéndez, A. Krier and S. I. Molina (2018) *Atomic column resolved HAADF-STEM analysis of InSb/InAs sub-monolayer quantum dots* in Marie Sklodowska-Curie ITN PROMIS conference, July 18-19, 2018 by Lancaster University, UK: *Oral Presentation*
- A. A. Khan, J. Pizarro, P. L. Galindo, M. Herrera and S. I. Molina (2017) *Development of a modified qHAADF program for atomic column resolution quantitative HAADF-STEM analysis* in Microscopy at the Frontiers of Science, September 5-8, 2017 (MFS2017) in Zaragoza, Spain: *Oral Presentation*
- Atif A. Khan, M. Herrera, J. Pizarro, P. L. Galindo, H. Fujita, E. R. Menéndez, A. Krier and S. I. Molina (2016) *Compositional analysis of InSb sub-monolayer quantum dots within (Al)GaSb-based barriers grown on GaAs* in 19th International Conference on Molecular Beam Epitaxy, September 4-9, 2016 (MBE2016) in Montpellier, France: *Poster Presentation*
- A. A. Khan, M. Herrera, N. Fernández-Delgado, D. Montesdeoca, P. Carrington, H. Fujita, J. S. J. Asirvathan, M. Wagener, R. Botha, A. Marshall, A. Krier and S. I. Molina (2016) *Structural analysis of GaSb/GaAs quantum rings for solar cells* in The 16th European Microscopy Congress, August 28 – September 2, 2016 (EMC2016) in Lyon, France: *Poster Presentation*

Workshops

- Marie Sklodowska-Curie ITN PROMIS workshop 2018 by University of Nottingham, UK.
- Marie Sklodowska-Curie ITN PROMIS workshop 2017 by Sapienza University of Rome, Italy
- 16th TEM-UCA European Summer Workshop Transmission Electron Microscopy of Nanomaterials 2016 by University of Cádiz, Spain.
- Marie Sklodowska-Curie ITN PROMIS workshop 2016 by University of Cádiz, Spain.

- Marie Sklodowska-Curie ITN PROMIS workshop 2015 by University of Sheffield, UK.

Appendix II

Publication I

Modified qHAADF method for atomic column-by-column compositional quantification of semiconductor heterostructures

Atif A. Khan, M. Herrera, J. Pizarro, P. L. Galindo, P. J. Carrington, H. Fujita, A. Krier, S. I. Molina

Journal of Materials Science 54: 3230 (2019)

J Mater Sci

Electronic materials

Modified qHAADF method for atomic column-by-column compositional quantification of semiconductor heterostructures

Atif A. Khan[1,*], M. Herrera[1], J. Pizarro[2], P. L. Galindo[2], P. J. Carrington[3], H. Fujita[4,5], A. Krier[4], and S. I. Molina[1]

[1] *Department of Material Science, Metallurgical Chemistry and Inorganic Chemistry, IMEYMAT, University of Cádiz, 11510 Puerto Real, Spain*
[2] *Department of Computer Engineering, ESI, University of Cádiz, 11510 Puerto Real, Spain*
[3] *Department of Engineering, Lancaster University, Lancaster LA1 4YW, UK*
[4] *Physics Department, Lancaster University, Lancaster LA1 4YB, UK*
[5] *Asahi Kasei Corporation, 2-1 Samejima, Fuji-City, Shizuoka 416-8501, Japan*

Received: 28 May 2018
Accepted: 23 October 2018

ABSTRACT

The qHAADF method allows the quantification of the composition at atomic column resolution in semiconductor materials by comparing the HAADF-STEM intensities between a region of interest to a region of the material of known composition. However, the application of this qHAADF approach requires both regions to be differentiable and included in the same micrograph at close proximity. This limits the application of this approach to certain materials and magnifications where this requirement is fulfilled. In this work, we extend the qHAADF method to analyses where the reference region is imaged in a separate micrograph. The validity of this modified method is proved by comparison to the original qHAADF approach using HAADF-STEM simulated images of the semiconductor heterostructure InSb/InAs. Additionally, the methods are applied successfully to experimental images both of a simple InSb/InAs interface and of a complex InSb/GaSb heterostructure, justifying the significance of the modified method over the original method.

Introduction

High angle annular dark field (HAADF)–scanning transmission electron microscopy (STEM) [1] is widely used for the investigation of the morphology and composition of materials at atomic scale [2–5]. The analysis of single dopant atom in crystalline structures [6], defects within structures [7], interfacial discontinuity [8–10] or structural strain [11] are some of the advantageous outcomes of this method. In some materials, the study of the composition at atomic scale is essential to understand their

Address correspondence to E-mail: atif.khan@uca.es

https://doi.org/10.1007/s10853-018-3073-y

Published online: 15 November 2018

performance. This is the case of semiconductor materials where, for example, the emission wavelength of InGaAsN laser can be tuned within 1.2–1.6 μm by manipulating In and N incorporations [12]. In InSbAs, the control of the distribution Sb–As allows the design of type II quantum dots (QDs) [13] based highly efficient mid-infrared optoelectronic devices at a wavelength range of 2–8 μm [14]. Because of this, HAADF-STEM has been widely used for the analysis of III–V [15] and II–VI [16] semiconductor heterostructures. As an example, the effect of the capping layer in the morphology of InAs/GaAs QDs [17] has been demonstrated using this technique. In semiconductor materials, quantifying the composition with large spatial resolution is needed to correlate material band structure and epitaxial growth conditions, which eventually assists the extrapolation of optimum device design parameters. Several direct and indirect analyzing techniques have been used in this regard such as photoluminescence (PL) [18, 19], energy dispersive spectroscopy (EDS) [20] or electron energy loss spectroscopy (EELS) [21, 22]. HAADF-STEM can also be used with this purpose, although the quantification is not straightforward as the HAADF-STEM signal contains both composition and specimen thickness induced information [23, 24]. Several methodologies have been developed in order to obtain quantitative information using (HA)ADF-STEM images. For example, a setup has been built to exploit the explicit angular dependence of scattered intensity for angle-resolved STEM to measure N content and specimen thickness in GaN_xAs_{1-x} [25]. Also, a method is proposed to normalize HAADF-STEM intensity to the incident electron beams in order to quantify ADF images [24, 26, 27]. Additionally, it has been shown that empirical incoherent parametric imaging can be combined with frozen lattice multislice simulations in order to evolve from a relative toward an absolute quantification of the composition of single atomic columns [28]. Although these methodologies have been shown to provide reliable results, they either require time consuming multiple experimental analyses in terms of variable image acquisition parameters or require additional complex instrumentation or not compatible to material segregation associated compositional quantification. As a result, a direct and faster compositional quantification model of quantitative HAADF (qHAADF) [29] has been developed that compares experimental HAADF-STEM integrated intensities of the region of interest (ROI) with the intensity of a homogenous (reference) area to quantify the composition [30], using a single set of image acquisition parameters. For example, the compositional distribution of Sb has been quantified within GaAs capped GaSb nanostructures [22] and in GaAsSbN capped InAs quantum dots (QDs) [31] using this method. However, this program only works when the ROI and reference regions are at the same HAADF-STEM image. This basic requirement limits this method to function in low magnification in terms of multilayered structures, where the ROI and the reference area (typically, substrate) could be positioned far away from each other. Moreover, in the compositional quantification of highly segregating materials like Sb [32], locating a homogenous region is rather complicated, restraining functionality to this method.

In this paper, a modified version of the qHAADF program is presented. This version compares the integrated intensities of a ROI area to a homogenous (reference) area present in two separate HAADF-STEM images in order to generate a compositional map on the ROI image. The InSb/InAs material is considered to exemplify the method. Primarily, the compositional outcomes of the modified method applied to simulated InSb/InAs images are compared to the existing qHAADF method using various image-pixel accumulation areas (integration areas), and to the real composition in the simulated models, proving its validity. Later, the compatibility of the modified method to the original method is demonstrated in terms of experimental HAADF-STEM $InAs/InSb_xAs_{1-x}/InAs$ images. As the final demonstration, another experimental HAADF-STEM image of alternating InSb/GaSb structure is considered which can potentially be analyzed by the modified method due to the absence of a reference region close to the ROI.

Materials and methods

The first experimental sample consists of an InSb/InAs heterostructure, grown on an InAs [001] substrate using molecular beam epitaxy (MBE) technique. This sample possesses 10 InSb layers of 1.4 ML each, where two consecutive InSb layers are separated by an InAs layer of 18 nm in between. The second experimental sample accommodates a 30 ML

thick MBE (001) grown QD layer, comprised of alternating sub-monolayer (SML) InSb/GaSb structure. This sample has been selected as an example because the existing qHAADF method assisting compositional quantification of In within this QD layer with the help of a homogeneous buffer layer of GaSb is rather impossible due to a presence of a very thick (1.5 μm) $Al_{0.3}Ga_{0.7}Sb$ barrier layer in between and hence justifies the importance of developing the modified method.

The electron transparent specimens for the HAADF-STEM analysis associated with both samples were prepared by mechanical thinning and Precision Ion Polishing System (PIPS) associated Ar^+ ion milling. All experimental high-resolution HAADF-STEM images of the prepared specimens were obtained using a JEOL JEM ARM 200cF single aberration corrected (condenser aberration) microscope working at an operating voltage of 200 kV, while having imaging parameters of $C_s = -611$ nm, $C_5 = 817.2$ mm, HAADF detector inner angle = 90 mrad, objective aperture angle = 15.2 mrad and defocus = − 1 Å.

Simulated HAADF images of InAs/InSb/InAs structures along [110] zone axis have been computed using the model illustrated in Fig. 1 where As columns are included as blue circles, In as cyan circles and Sb as yellow circles. In each simulated model, Sb columns are included within 3 central monolayers (MLs) as shown in Fig. 1, with partial presence of As ($InSb_xAs_{1-x}$). Here, the nominal Sb composition (x) is varied from 0 to 0.5 with 0.1 increment. All the simulations were performed using SICSTEM software that runs on CAI supercomputer in UCA. The working principle of the SICSTEM software can be found here [33]. Aberration correction associated spatial incoherence was also considered during simulations [34].

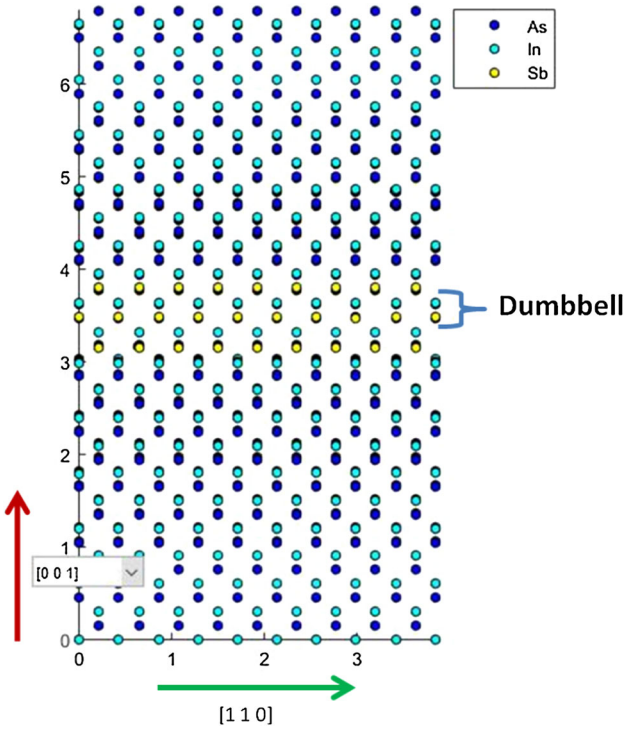

Figure 1 Schematic of the model used for the simulation of the InAs/InSb/InAs layers.

Results and discussion

Implementation of the method

In order to exemplify the application of the modified qHAADF method, two simulated images of InAs/$InSb_xAs_{1-x}$/InAs ([001]) have been chosen where the nominal Sb composition at the ROI image is 50% ($x = 0.5$) and at the reference image is 0% ($x = 0$), with specimen thickness of 20 nm. As the first processing step, individual local intensity maxima associated with the group III and V atomic columns are located within each HAADF-STEM image. This is done using a peak finding (PF) technique, used by Pedro L. Galindo et al. while developing the Peak Pairs (PP) method [35]. Figure 2a shows a simulated HAADF-STEM image of the ROI (the Sb containing layer) with PF generated peaks, where the group III (In) atomic columns are marked with red dots and the group V (As/Sb) columns with blue dots. For clarity, the inset shows a single III–V pair (dumbbell) with separate group III (red) and group V (blue) column peaks. In our case, the atomic columns with variable composition are the group V ones so they are the columns of interest. In order to measure the intensity in these columns, integration areas are chosen around the group V intensity maxima. In this case, an integration area containing the same part of the atomic column as proposed in [36] has been chosen with different pixel numbers justifying the corresponding image resolution (see the green rectangle included in the inset of Fig. 2a), which is reported to possess least susceptibility to the effects of the neighboring group III columns. This integration area can be named as Mask 1. As the first calculation step, the pixel intensities are integrated

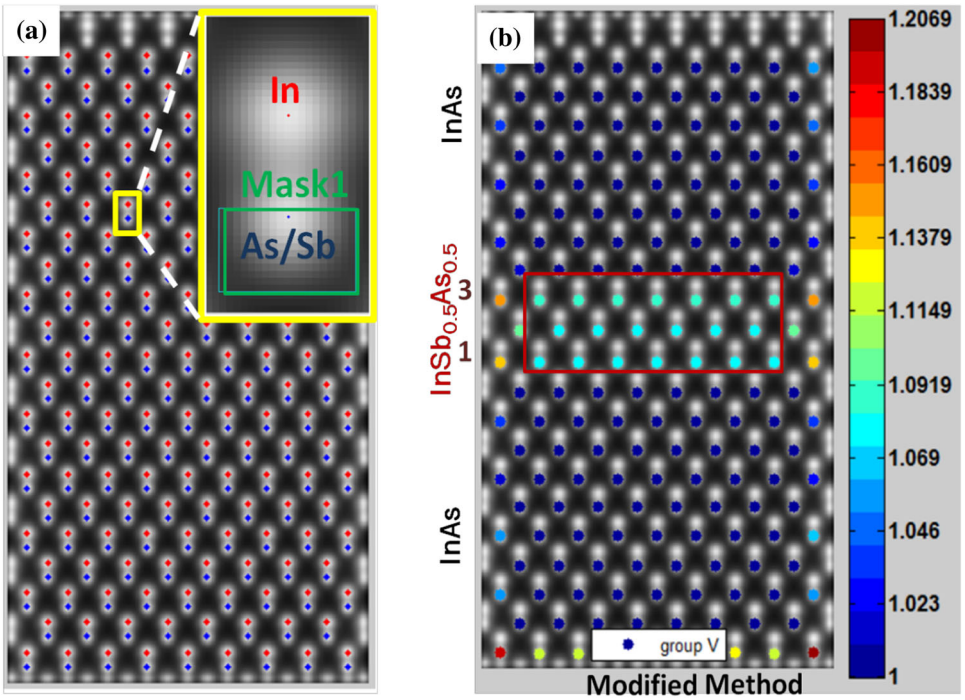

Figure 2 **a** HAADF-STEM simulated image of $InSb_{0.5}As_{0.5}$ where the group III (In) atomic columns are marked with red dots and the group V (As/Sb) atomic columns with blue dots. The inset represents a single dumbbell where a group V atomic column is surrounded by a Mask1 (green rectangle). **b** The modified qHAADF method generated '*R*' map corresponds the image in **a**. The red rectangle represents the $InSb_{0.5}As_{0.5}$ area.

within Mask 1 areas on each dumbbell individually on the ROI image. With regards to the reference image, it has been taken as the HAADF-STEM image that contains only InAs dumbbells (known composition). Similarly to the procedure explained above for the ROI image, the Mask 1 containing pixel intensities around each group V (As) atomic columns integrated on the reference image and later these integrated intensities from all group V (As) columns are averaged. Finally, the integrated intensities from each group V column on the ROI image are divided by the average of the integrated intensities from the group V columns on the reference image. These outcomes on the ROI image can be termed as normalized integrated intensities, *R*. Figure 2b represents the modified qHAADF program originated '*R*' map corresponding to the group V columns (As/Sb) included in Fig. 2a. In this map, $R = 1$ (deep blue dots) depicts the absence of Sb (InAs atomic columns). The red rectangle marks the dumbbells within the three $InSb_{0.5}As_{0.5}$ MLs, where an average '*R*' value of ~ 1.08 has been measured. It should be noted that the unrealistic and relatively higher '*R*' values associated with the dumbbells nearer to the image boundaries must not be taken into account as those contain simulation originated boundary errors.

In order to assess the validity of the modified method, it has been compared to the original qHAADF method. For this, InAs dumbbells from the same image of $InSb_{0.5}As_{0.5}$ analyzed have been taken as the reference region for the calculation, and the same Mask 1 has been used while having the sample thickness of 20 nm. Our results have shown that the original method generates same '*R*' values over same group V columns (not shown) as in Fig. 2b. This outcome confirms that for a homogenous and same ROI-reference thickness, the modified method is compatible with the original method in terms of simulated images.

To analyze the efficiency of the modified method, the deviation of Sb composition values obtained from the qHAADF methods with regards to the nominal composition need to be evaluated. This requires converting the Sb contribution associated '*R*' values within the InSbAs layers into composition values. For this, we have used the atomic column-by-column quantification approach developed in [29]. Here, a statistically obtained linear regression equation was proposed to quantify column-by-column As composition from '*R*' or 'R_i' values, associated with experimental $InAs_xP_{1-x}/InP$ structure. The proposed equation is

$$R_i = 1 + a \cdot x_i \quad (1)$$

where x_i represents As composition. They obtained the constant '*a*' value by evaluating an As-based

statistical R_i versus x_i graph in terms of a few known x_i compositions. They have also experimentally ensured that the effect of certain range of sample thicknesses over 'R_i' values is insignificant and hence, the variation in x_i is the only effective contributing parameter here. Later on, the validity of the above mentioned equation was justified at [36] for other III–V ternary alloys. Here, the researchers proposed a direct approach to obtain the constant 'a' value by summing monolayer-by-monolayer average 'R_i' values within certain number of MLs (N), where the both analyzing and reference materials must be present at the same HAADF-STEM image. Their proposed equation was

$$\sum_{i=1}^{N} Ri = N + a \cdot \sum_{i=1}^{N} xi. \tag{2}$$

This equation illustrates the total change in the R_i value due to total deposition of x_i within certain number of MLs (N). This equation provides the 'a' value, which later can be used to obtain average monolayer-by-monolayer or column-by-column x_i values.

We have applied the methodology above for the quantification of Sb in our simulated HAADF images using the 'R' values obtained with the modified method shown in Fig. 2b. Initially, 'a' has been obtained using total deposited x_i values and corresponding average monolayer-by-monolayer R_i values within N MLs. For that, 17 MLs in the ROI image have been chosen (N = 17) as it ensures that the 3 Sb containing MLs are present within that 17 MLs while ignoring the simulation oriented boundary errors. Next, the obtained 'a' value is used in the first equation and Sb associated column-by-column local composition map is generated. Figure 3a represents the column-by-column local composition values calculated for the image corresponding to $InSb_{0.5}As_{0.5}$ through red dots. Here, to maintain simplicity evaluating the Mask1 associated deviation between the nominal (x = 0.5) and calculated values, four central group V columns have been chosen, represented within a yellow rectangle. The obtained average value of Sb composition associated with those four dumbbells has been found to be 47.38% with a standard estimation error of 3.77%. This error falls within 99.9% of confidence level to the average value associated with statistical two-sided t-distribution, signifying that the composition of 47.38 ± 3.77% assures 99.9% certainty to the true (nominal) value. In order to determine whether this method is also good for other nominal compositions, column-by-column Sb composition quantification maps have been generated for the Sb nominal values of $0.1 \leq x \leq 0.4$ (not shown) with 0.1 increment. Figure 3b shows a graph of the average atomic column Sb composition (x_i) versus nominal Sb composition associated with Mask1 for images with $0 \leq x \leq 0.5$ (in green). Here, the Mask1 based overall standard error obtained from the calculated profile (Mask1) is found to be only 4.37%, assuring that the modified qHAADF method is in a good agreement with the expected values in terms of all nominal compositions of $0 \leq x \leq 0.5$.

It should be noted that, as suggested by Jones [37], Mask size can be influential in terms of compositional quantification. However, there is no agreement in the literature regarding which mask would be more appropriate for composition quantification. For example, Mask1 functions appropriately in terms of very thin samples, ranging from 15 to 40 nm [34] since the investigating atomic column stays unaffected by the surrounding dumbbells in this thickness range [29]. On the other hand, some researchers suggested a Mask that contains the whole analyzing atomic column proving to provide better HAADF quantitative approach in terms of varying convergence angle, magnification, source size and defocus [38], sample associated small mis-tilt [39], aberrations and astigmatism [40] and scan induced noises [41], as long as the probe size does not change with the sample thickness. These characteristics allow possibility analyzing even thicker samples than of Mask1. In addition, another Mask has been suggested that imposes rectangular Voronoi cell [42] around each whole dumbbell that allows analyzing even thicker samples by providing an average value closer to the nominal [37]. Moreover, for a HAADF-STEM detection angle of 90 mrad, these Voronoi cells are sensitive to sample thickness induced effect [25] and hence, compositional quantification with a higher precision is expected as the thickness contribution to the HAADF-STEM signal can be identified. Because of these arguments, along with Mask1, the modified qHAADF program has been examined with two other Mask sizes, termed as Mask2 (covers each whole group V column) and Mask3 (covers each whole dumbbell) in terms of simulated images, while both ROI and reference images possess same

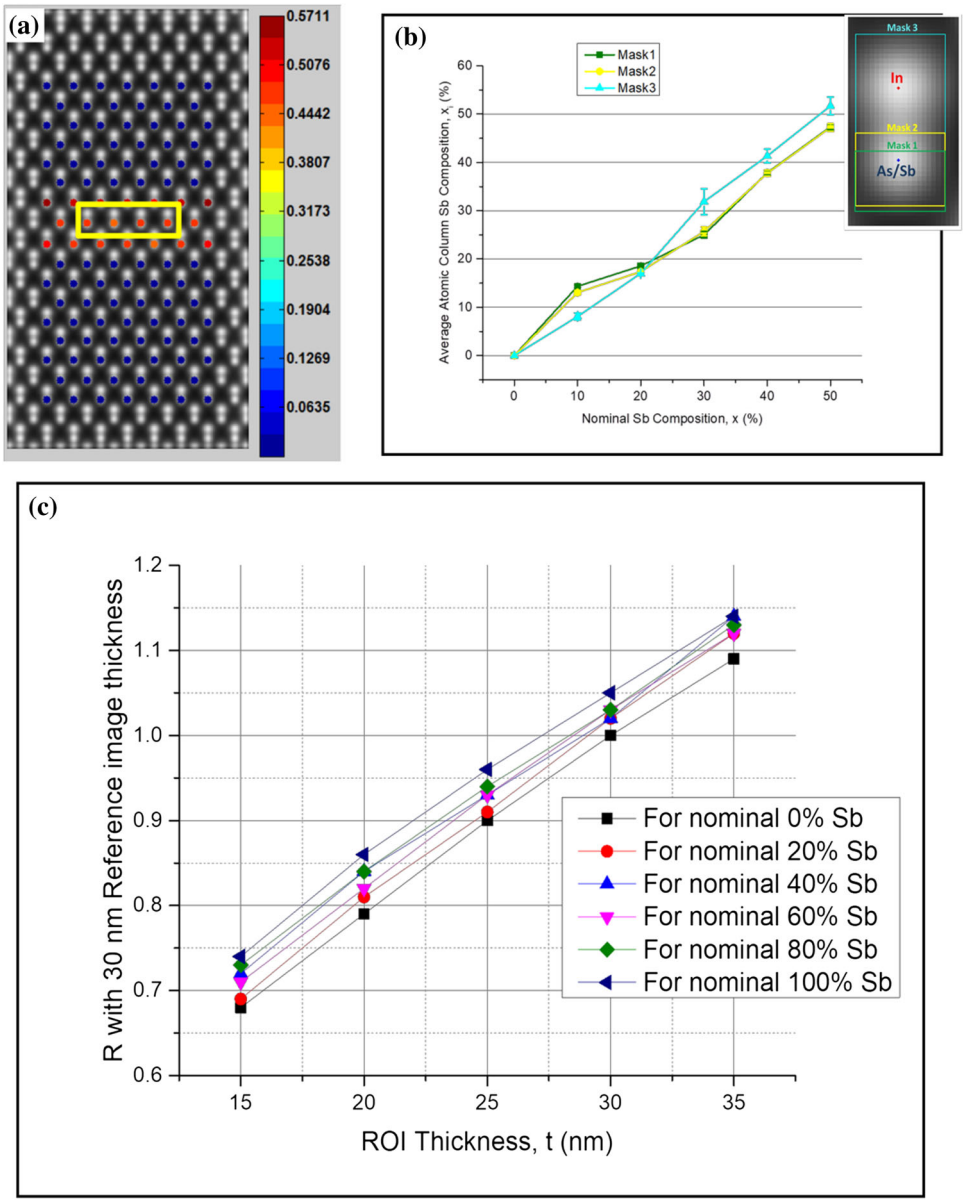

Figure 3 **a** Atomic column composition map calculated from the modified qHAADF originated '*R*' values shown in Fig. 2b, superimposed to the HAADF-STEM simulated image. **b** Graph of the average atomic column Sb composition calculated from the modified qHAADF originated '*R*' values versus the nominal Sb composition for the three masks considered. The error bars illustrate standard deviations to the corresponding averages. The inset represents the three mask areas considered: Mask1 (green), Mask2 (yellow) and Mask3 (cyan), surrounding a single In–As/Sb dumbbell. **c** Plots of Sb composition induced R *vs* specimen thickness effect as per simulated HAADF-STEM signals with ROI thicknesses of 15–35 nm in association to average reference thickness of 30 nm.

specimen thickness of 20 nm. Figure 3b shows Mask1 (green), Mask2 (yellow) and Mask3 (cyan) originated graphs in terms of the average atomic column Sb compositions (x_i), associated with the same dumbbells within the yellow rectangle as in Fig. 3a versus varying nominal Sb composition ($0 \leq x \leq 0.5$). For clarity, Fig. 3b includes an inset showing a single In–As/Sb dumbbell where the three masks considered have been graphically represented. Here, the Mask1 based overall standard error obtained from the calculated profile (Mask1) is found to be only 4.37%. Again, the overall standard errors corresponding to Mask2 and Mask3 have also been found to be very small as 3.96% and 2.63%, respectively. Thus, our results show that in terms of simulated HAADF-STEM images with same specimen thickness, the three mask sizes considered are appropriate for the composition quantification. The high level of accuracy obtained could face slight degradation in terms of experimental analysis if the required parameters are not calibrated properly during the image acquisition. For example, to obtain the '*R*' values, it is essential that both the ROI and reference HAADF-STEM images possess same image contrast, brightness and magnification. Once the necessary calibrations are performed, this modified method will offer benefits analyzing high-resolution HAADF-STEM images associated with very high magnifications,

since the ROI and reference regions do not need to be present in the same image. For example, the high-resolution compositional quantification of a highly segregating material such as Sb [32] within a complex micro structure can be performed using this method without finding a pure homogenous area in the same HAADF-STEM image.

It is worth mentioning that the thickness of the sample also plays an essential role in the composition quantification as it has a strong effect on the HAADF-STEM intensity. It has been experimentally proved that the relative normalized integrated intensity 'R', and eventually the composition of a material is hardly affected by the specimen thickness within 15–40 nm [34], as long as both ROI and reference areas exist in the same image and have similar thicknesses [29]. Because of this, in the present paper we address the issue of errors due to the specimen thickness considering the case where the ROI and the reference images correspond to regions of the specimen with different thicknesses. For this, we have measured the R values for $InSb_xAs_{1-x}$ (ROI) images with thickness 15–35 nm considering reference InAs regions with average thickness of 30 nm, for Sb compositions of 0% to 100%, and we show the results obtained in Fig. 3c. As observed in this Figure, for each 1 nm increment at the specimen thickness, the R values increase by a factor of $\sim 0.02 \pm 0.004$ for every Sb composition. For this thickness range, Eq. (1) can be rewritten as

$$R = 1 + a \cdot xi \pm 0.02 \cdot \Delta t \tag{3}$$

As it can be observed, there is a strong effect of Δt on R, indicating that the precise measurement of the thickness of both ROI and reference regions is essential for the precise calculation of the atomic columns composition. However, it is not necessary to use ROI and reference regions with exactly the same thickness, as the calculation of the effect of Δt on R based on simulated images may assist in the quantification of the thickness related intensity modification, allowing a composition value read-justment. This is not inherent to the modified method and should be extended to the original method as well, where sometimes thickness differences can be found in different regions of the same image. However, these thicknesses differences are expected to be more noticeable in the modified method due to the larger distance between ROI and reference regions in the specimen. Therefore, specimen thickness associated with each experimental HAADF-STEM image must be measured with the highest precision through zero-loss peak EELS analysis.

Application of the method to InSb/InAs and InSb/GaSb experimental HAADF-STEM images

To understand how this modified method behaves in terms of experimental HAADF-STEM images, it has been applied to a semiconductor heterostructure of InSb/InAs. HAADF-STEM images of this material have been acquired using the same imaging parameters as in the simulated images (included in the section Experimental Details). Initially and in order to select ROI and reference regions with similar thicknesses, the sample has been analyzed at low magnification, as shown in the HAADF-STEM image of Fig. 4a, where the InSb layers can be observed. The corresponding absolute thickness profile along the green line in Fig. 2a at [001] direction is depicted in Fig. 4b, obtained using zero-loss peak EELS analysis. To generate the absolute thickness profile, Gatan digital micrograph software has been used in terms of HAADF-STEM image acquisition specific log-ratio (absolute) parameters associated with electron mean free path (MFP) of ~ 59 nm (calculated using the equations in [43]) at the spectrometer acceptance angle of 90 mrad (semi angle) and alloy specific effective atomic number, Z_{eff}. The thickness variation between the average thickness of the ROI region and the average thickness of the reference area in the region of the red rectangle in Fig. 4a has been found to be of ~ 1 nm ($t_{\text{ROI}} > t_{\text{reference}}$), as it can be observed in Fig. 4b. Figure 4c illustrates the atomic column resolution HAADF-STEM image of the ROI region in this area that contains an InSb layer. It should be noted that this image contains the opposite III–V polarity to the simulated images, i.e., the group V (As/Sb) element constitutes the top column of each dumbbell, while the group III (In) element are at the bottom column. The vacuum level signal associated with the microscope detector has been subtracted from the obtained experimental HAADF-STEM images [37] and the noise has been reduced by applying a Wiener filter in Fourier space [44]. In order to detect the position of the InSb layer, Fig. 4d shows an intensity profile obtained from the red rectangle box in Fig. 4c along [001] direction. In each specific ML along [110] direction, each higher peak assigns the

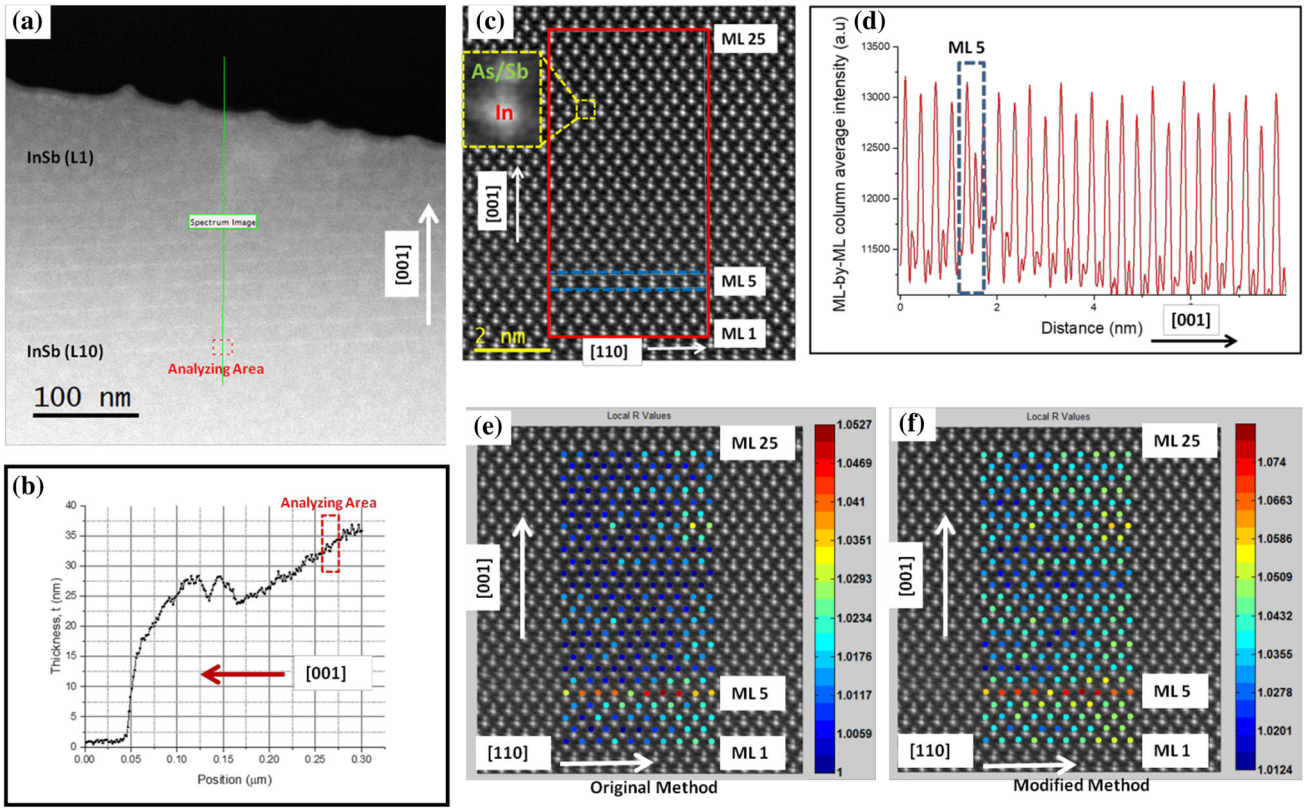

Figure 4 **a** Low-mag HAADF-STEM image where the red rectangle depicts the location of the analyzing ROI and Reference areas; **b** corresponding thickness profile associated with the Spectrum image line (green line), along with the analyzing area in **a**. **c** Experimental HAADF-STEM image of InSb/InAs (single In–As/Sb dumbbell at the inset); **d** intensity profile obtained from the image in **c**, evidencing the position of the InSb layer; R map calculated with the original **e** and modified **f** methods, from the HAADF-STEM image in **c**.

average intensity from the group III atomic column (Z_{In} = 49), and each lower peak designates the average intensity from the group V (Z_{As} = 33), within that ML. According to the obtained profile, the average intensity count along [110] direction from the As/Sb columns within ML5 (marked with blue dotted rectangles in Fig. 4a and b) has higher value than any other As/Sb columns, indicating the presence of Sb at ML5. In order to generate a quantitative '*R*' map from this HAADF-STEM image (ROI image) using the modified qHAADF method, another HAADF-STEM image with same magnification and imaging parameters as in the ROI image has been taken from the InAs substrate in the region of similar thickness (not shown), which will be used as the reference image. Individual local intensity maxima associated with the group III and V atomic columns have been located using previously discussed peak finding (PF) technique, [35] and *R* values have been calculated similarly as in the simulated images. Figure 4e and f represents the original and the modified qHAADF method generated '*R*' maps, respectively. As it can be observed, larger *R* values are obtained in ML5 in both methods where Sb is present, as expected, with an average value of $\sim$ 1.04 (Fig. 4e) associated with the original method and of $\sim$ 1.06 (Fig. 4f), associated with the modified method where average ROI thickness is greater ($\sim$ 1 nm) than the average reference thickness. Due to this variation in the *R* values, the corresponding average x_i at ML5 using equation $R = 1 + a{\cdot}x_i$ become $\sim$ 27% for the original and $\sim$ 46% for modified method. This 16% difference in x_i between the original and modified method is due to the specimen thickness contribution for $a \sim 1$ nm ROI-reference average thickness variation in the modified method. As this is a large difference for quantitative purposes, image simulations need to be taken into account to recalculate the obtained values considering the thickness variations measured in order to obtain precise composition values. In order

to do that, in this case Eq. (3) above can be used. For values of Δt of 1 nm and $R \sim 1.06$, we obtain a x value of $\sim$ 26%, which is very close to the value obtained with the original method, as expected.

To assess how the methodology proposed here allows the analysis at atomic column resolution of regions with strong material segregation, where finding a reference area of known composition is challenging, another experimental sample that contains 30 ML of alternating layers of InSb/GaSb structures within a QD layer has been considered. The segregation tendency of In [45] tend to form $In_xGa_{1-x}Sb$ ternary alloy (ROI) and, hence, obtaining a reference area within the QD layer is rather challenging. On the other hand, due to a great distance of 1.5 µm between the ROI and homogeneous GaSb buffer (reference), they cannot be imaged in the same micrograph. Therefore, it is impractical to quantify In using the original method. This limitation of the original qHAADF method is the principle encouraging factor to develop the modified method, enabling analyzing complex materials. HAADF-STEM images have been acquired from regions in the specimen along the curvature of the conventional technique generated hole, with the aim to find areas of similar thicknesses measured by zero-loss EELS. Figure 5a shows a HAADF-STEM image of the InSb/GaSb (ROI) region, and Fig. 5b depicts the corresponding absolute thickness profile calculated for electron MFP of $\sim$ 61 nm (calculated using the equations in [43]) at the spectrometer acceptance angle of 90 mrad (semi angle) using zero-loss EELS showing an average thickness of $\sim$ 26 nm. In order to calculate R, an area of similar thickness within the reference region (GaSb buffer) has been chosen. Figure 5c shows a HAADF-STEM image of the GaSb substrate, and Fig. 5d shows the absolute thickness profile within the white rectangle in Fig. 5c, generated similar way as in the ROI image. As observed in Fig. 5d, the average thickness at that white rectangle region in Fig. 5c is $\sim$ 21 nm. To ensure a slightly smaller thickness variation of the ROI area to the reference area, a smaller region ($\sim$ 4 nm) in ROI image was chosen with an average thickness of $\sim$ 25 nm, as shown in the ROI thickness profile (Fig. 5b). Finally, the R map is generated on this new ROI using the modified method, illustrated in Fig. 5e. Here, the variable intensity in the group III atomic columns indicates heterogeneous In composition associated with In segregation within the image area. When the existing ROI-reference average thickness variation of $\sim$ 4 nm is not considered, the maximum In composition in this region obtained using equation $R = 1 + a \cdot x_i$ is $\sim$ 18%. In order to analyze how thickness contributes in the HAADF-STEM analyzed signal, simulated models of $GaSb/In_xGa_{1-x}Sb/GaSb$ have been generated. Figure 5f represents plots of R calculated for variable thicknesses of 21–27 nm on ROI in association with the average reference thickness of 21 nm in terms of 0–20% nominal In composition. Here, In associated increment factor has been found to be $\sim 0.025 \pm 0.001$. Now, with the help of the specimen thickness effect contributing equation mentioned above, the maximum In composition in Fig. 5e can be recalculated as $\sim$ 3.27%, as for each 1 nm specimen thickness variation, 3.75% false In composition is added in the HAADF-STEM signals. Local In composition values associated with each atomic column can be recalculated as well in order to obtain a precise information on the atomic column composition distribution in the material. Although it is out of the scope of this paper, this would allow a deep understanding of the growth process of the material, possible deviations from the original design due to segregation and the correlation to the functional properties of the material, which is often done using indirect techniques [13, 46].

Conclusions

We have developed a modified qHAADF method for the quantitative analysis of the composition with atomic column resolution for cases where the ROI and the reference regions are imaged in separate HAADF-STEM micrographs. The compatibility of this method to the original method has been justified with the help of simulated HAADF-STEM images of $InAs/InSb_xAs_{1-x}/InAs$, where $0 \leq x \leq 0.5$. The compatibility between the methods in terms of experimental InSb/InAs structures HAADF-STEM images has also been proved. Additionally, the significance of the modified method over the original method is justified in terms of HAADF-STEM compositional analysis of InSb/GaSb structure, situated far away from the homogeneous GaSb buffer layer.

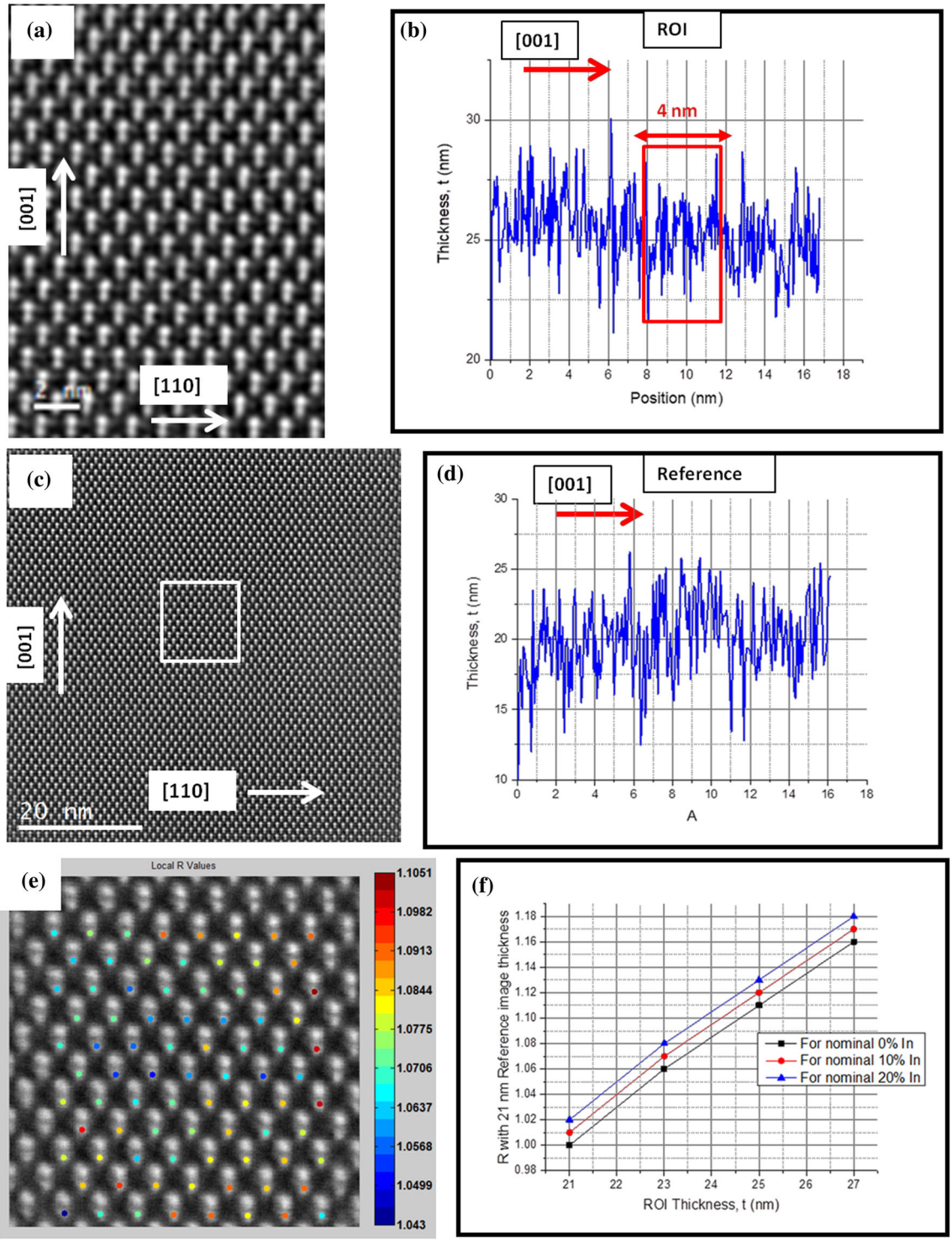

Figure 5 **a** HAADF-STEM image of InSb/GaSb (ROI area) and **b** the corresponding absolute thickness profile; **c** HAADF-STEM image of the GaSb buffer layer (reference area) and **d** the corresponding thickness profile taken from the region on the white rectangle at **c**; **e** R map on the ~ 4 nm ROI area within the selected thickness range in **b**, calculated with the modified method; **f** plots of In composition induced R versus specimen thickness effect as per simulated HAADF-STEM signals with ROI thicknesses of 21–27 nm in association with average reference thickness of 21 nm.

Acknowledgements

This work was supported by European Union (UE) (postgraduate research on dilute metamorphic nanostructures and metamaterials in semiconductor photonics (PROMIS) Horizon 2020 initial training network (ITN) project), Spanish MINECO (Projects TEC2014-53727-C2-2-R and TEC2017-86102-C2-2-R) and the Junta de Andalucía (PAI research groups TEP-946 INNANOMAT and TIC-145). Cofinancing from UE-FEDER is also acknowledged.

Compliance with ethical standards

Conflict of interest The authors declare that they do not have any conflict of interest.

References

[1] Pennycook SJ, Rafferty B, Nellist PD (2000) Z-contrast imaging in an aberration-corrected scanning transmission electron microscope. Microsc Microanal 6:343–352

[2] Pennycook SJ, Boatner LA (1988) Chemically sensitive structure-imaging with a scanning electron microscope. Nature 336:565–567

[3] Batson PE, Dellby N, Krivanek OL (2002) Sub-ångstrom resolution using aberration corrected electron optics. Nature 418:617–620

[4] Muller DA, Nakagawa N, Ohtomo A, Grazul JA, Hwang HY (2004) Atomic-scale imaging of nanoengineered oxygen vacancy profiles in $SrTiO_3$. Nature 430:657–661

[5] Mitchson G, Ditto J, Woods KN, Westover R, Page CJ, Johnson DC (2016) Application of HAADF-STEM image analysis to structure determination in rotationally disordered and amorphous multilayered films. Semicond Sci Technol 31:084003

[6] Kaiser U, Muller DA, Grazul JL, Chuvilin A, Kowasaki M (2002) Direct observation of defect-mediated cluster nucleation. Nat Mater 1:102–105

[7] Yamazaki T, Nakanishi N, Recnik A, Kawasaki M, Watanabe K, Ceh M, Shiojiri M (2004) Quantitative high-resolution HAADF-STEM analysis of inversion boundaries in Sb_2O_3-doped zinc oxide. Ultramicroscopy 98:305–316

[8] Anderson SC, Birkeland CR, Anstis GR, Cockayne DJH (1997) An approach to quantitative compositional profiling at near-atomic resolution using high-angle annular dark field imaging. Ultramicroscopy 69:83–103

[9] Klie RF, Zhu Y (2005) Atomic resolution STEM analysis of defects and interfaces in ceramic materials. Micron 36:219–231

[10] Klenov DO, Stemmer S (2006) Contributions to the contrast in experimental high-angle annular dark-field images. Ultramicroscopy 106:889–901

[11] Wang P, Bleloch AL, Falke M, Goodhew PJ, Ng J, Missous M (2006) Direct measurement of composition of buried quantum dots using aberration-corrected scanning transmission electron microscopy. Appl Phys Lett 89:072111

[12] Mokkapati S, Jagadish C (2009) Review: III-V compound SC for optoelectronic devices. Mater Today 12:22–32

[13] Semenov A, Lyublinskaya OG, Solov'ev VA, Meltser BY, Ivanov SV (2007) Surface segregation of Sb atoms during molecular-beam epitaxy of InSb quantum dots in an InAs(Sb) matrix. J Cryst Growth 301–302:58–61

[14] Namazi L, Ghalamestani SG, Lehmann S, Zamani RR, Dick KA (2017) Direct nucleation, morphology and compositional tuning of $InAs_{1-x}Sb_x$ nanowires on InAs (111) B substrates. Nanotechnology 28:165601

[15] Zhang Y, Wu J, Aagesen M, Liu H (2015) Review: III-V nanowires and nanowire optoelectronic devices. J Phys D Appl Phys 48:463001

[16] Bonef B, Gérard L, Rouvière JL, Grenier A, Jouneau PH, Bellet-Amalric E, Mariette H, André R, Bougerol C (2015) Atomic arrangement at ZnTe/CdSe interfaces determined by high resolution scanning transmission electron microscopy and atom probe tomography. Appl Phys Lett 106:051904

[17] Tey CM, Liu HY, Cullis AG, Ross IM, Hopkinson M (2005) Structural studies of a combined InAlAs-InGaAs capping layer on 1.3-μm InAs/GaAs quantum dots. J Cryst Growth 285:17–23

[18] Chery N, Ngo TH, Chauvat MP, Damilano B, Courville A, Mierry PD, Grieb T, Mehrtens T, Krause FF, Caspary KM, Schowalters M, Gil B, Rosenauer A, Ruterana P (2017) The microstructure, local indium composition and photoluminescence in green-emitting InGaN/GaN quantum wells. J Microsc 00:1–8

[19] Groiss H, Spindlberger L, Oberhumer P, Schäffler F, Fromherz T, Grydlik M, Brehm M (2017) Photoluminescence enhancement through vertical stacking of defect-engineered Ge on Si quantum dots. Semicond Sci Technol 32:02LT01

[20] Nie JF (2017) IOP Conf Ser Mater Sci Eng 219:012005

[21] Sales DL, Guerrero E, Rodrigo JF, Galindo PL, Yáñez A, Shafi M, Khatab A, Mari RH, Henini M, Novikov S, Chisholm MF, Molina SI (2011) Distribution of bismuth atoms in epitaxial GaAsBi. Appl Phys Lett 98:101902

[22] Molina SI, Beltrán AM, Ben T, Galindo PL, Guerrero E, Taboada AG, Ripalda JM, Chisholm MF (2009) High resolution electron microscopy of GaAs capped GaSb nanostructures. Appl Phys Lett 94:043114

[23] Broek WVD, Rosenauer A, Goris B, Martinez GT, Bals S, Aert SV, Dyck DV (2012) Correction of non-linear thickness

in HAADF-STEM electron tomography. Ultramicroscopy 116:8–12

[24] Rosenauer A, Gries K, Müller K, Pretorius A, Schowalter M, Avramescu A, Engl K, Lutgen S (2009) Measurement of specimen thickness and composition in AlxGa1-xN/GaN using high-angle annular dark field images. Ultramicroscopy 109:1171–1182

[25] Caspary KM, Oppermann O, Grieb T, Krause FF, Rosenauer A, Schowalter M, Mehrtens T, Beyer A, Volz K, Potapov P (2016) Material characterization by angle-resolved scanning transmission electron microscopy. Sci Rep 6:37146

[26] LeBeau JM, Findlay SD, Allen LJ, Stemmer S (2008) Quantitative atomic resolution scanning transmission electron microscopy. Phys Rev Lett 100:206101

[27] LeBeau JM, Findlay SD, Wang X, Jacobson AJ, Allen LJ, Stemmer S (2009) High-angle scattering of fast electrons from crystals containing heavy elements: simulation and experiment. Phys Rev B 79:214110

[28] Martinez GT, Rosenauer A, Backer AD, Verbeeck J, Aert SV (2014) Quantitative composition determination at the atomic level using model-based high-angle annular dark field scanning transmission electron microscopy. Ultramicroscopy 137:12–19

[29] Molina SI, Sales DL, Galindo PL, Fuster D, González Y, Alén B, González L, Varela M, Pennycook SJ (2009) Column-by-column compositional mapping by Z-contrast imaging. Ultramicroscopy 109:172–176

[30] Molina SI, Galindo PL, Gonzalez L, Ripalda JM, Varela M, Pennycook SJ (2010) Exploring semiconductor quantum dots and wires by high resolution electron microscopy. J Phys Conf Ser 209:012004

[31] Reyes DF, González D, Ulloa JM, Sales DL, Dominguez L, Mayoral A, Hierro A (2012) Impact of N on the atomic-scale Sb distribution in quaternary GaAsSbN-capped InAs quantum dots. Nanoscale Res Lett 7:653

[32] Lu J, Luna E, Aoki T, Steenbergen EH, Zhang YH, Smith DJ (2016) Evaluation of Sb segregation in InAs/$InAs_{1-x}Sb_x$ type-II superlattices grown by molecular beam epitaxy. Appl Phys Lett 119:095702

[33] Pizarro J, Galindo PL, Guerrero E, Yáñez A, Guerrero MP, Rosenauer A, Sales DL, Molina SI (2008) Simulation of high angle annular dark field scanning transmission electron microscopy images of large nanostructures. Appl Phys Lett 93:153107

[34] Molina SI, Guerrero MP, Galindo PL, Sales DL, Varela M, Pennycook SJ (2011) Calculation of integrated intensities in aberration-corrected Z-contrast images. J Electron Microsc 60:29–33

[35] Galindo PL, Kret S, Sanchez AM, Laval JY, Yáñez A, Pizarro J, Guerrero E, Ben T, Molina SI (2007) The Peak Pairs algorithm for strain mapping from HRTEM images. Ultramicroscopy 107:1186–1193

[36] Hernández-Maldonado D, Herrera M, Alonso-González P, González Y, González L, Gázquez J, Varlea M, Pennycook SJ, Guerrero-Lebrero MP, Pizarro J, Galindo PL, Molina SI (2011) Compositional analysis with atomic column spatial resolution by 5th-order aberration-corrected scanning transmission electron microscopy. Microsc Microanal 17:578–581

[37] Jones L (2016) Quantitative ADF-STEM: acquisition, analysis and interpretation. IOP Conf Ser Mater Sci Eng 109:012008

[38] MacArthur HE, MacArthur KE, Pennycook TJ, Okunishi E, D'Alfonso AJ, Lugg NR, Allen LJ, Nellist PD (2013) Probe integrated scattering cross sections in the analysis of atomic resolution HAADF STEM images. Ultramicroscopy 133:109–119

[39] MacArthur KE, D'Alfonso AJ, Ozkaya D, Allen LJ, Nellist PD (2015) Optimal ADF STEM imaging parameters for tilt-robust image quantification. Ultramicroscopy 156:1–8

[40] Martinez GT, Backer AD, Rosenauer A, Verbeeck J, Aert SV (2013) The effect of probe inaccuracies on the quantitative model-based analysis of high angle annular dark field scanning transmission electron microscopy images. Micron 63:57–63

[41] Jones L, Nellist PD (2013) Identifying and correcting scan noise and drift in the scanning transmission electron microscope. Microsc Microanal 19:1050–1060

[42] Aurenhammer F (1991) Voronoi diagrams–a survey of fundamental geometric data structure. ACM Comput Surv 23:345–405

[43] Malis T, Cheng SC, Egerton RF (1988) EELS log-ratio technique for specimen-thickness measurement in the TEM. J Electron Microsc Tech 8:193–200

[44] Wiener N (1949) Extrapolation, interpolation and smoothing of stationary time series. Wiley, New York

[45] Haxha V, Drouzas I, Ulloa JM, Bozkurt M, Koenraad PM, Mowbray DJ, Liu HY, Steer MJ, Hopkinson M, Migliorato MA (2009) Role of segregation in InAs/GaAs quantum dot structures capped with a GaAsSb strain–reduction layer. Phys Rev B 80:165334

[46] Carrington PJ, Solov'ev VA, Zhuang Q, Krier A, Ivanov SV (2008) Room temperature midinfrared electroluminescence from InSb/InAs quantum dot light emitting diodes. Appl Phys Lett 93:091101

Publication II

Investigation on Sb distribution for InSb/InAs sub-monolayer heterostructure using TEM techniques

Atif A. Khan, M. Herrera, N. Fernández-Delgado, D. F. Reyes, J. Pizarro,

E. Repiso, A. Krier, S. I. Molina

Nanotechnology 31: 025706 (2020)

IOP Publishing Nanotechnology
Nanotechnology 31 (2020) 025706 (11pp) https://doi.org/10.1088/1361-6528/ab4751

Investigation on Sb distribution for InSb/InAs sub-monolayer heterostructure using TEM techniques

Atif A Khan[1], M Herrera[1], N Fernández-Delgado[1], D F Reyes[1], J Pizarro[2], E Repiso[3], A Krier[3] and S I Molina[1]

[1] Department of Material Science, Metallurgical Chemistry and Inorganic Chemistry, IMEYMAT, University of Cádiz, E-11510 Puerto Real, Spain
[2] Department of Computer Engineering, ESI, University of Cádiz, E-11510 Puerto Real, Spain
[3] Physics Department, Lancaster University, Lancaster, LA1 4YB, United Kingdom

E-mail: atif.khan@uca.es

Received 18 March 2019, revised 6 August 2019
Accepted for publication 24 September 2019
Published 11 October 2019

Abstract

InSb/InAs sub-monolayer (SML) nanostructures such as SML quantum dots offer sharper emission spectra, a better modal gain and a larger modulation bandwidth compared to its Stranski–Krastanov counterpart. In this work, the Sb distribution of SML InSb layers grown by migration enhanced epitaxy has been analyzed by transmission electron microscopy (TEM) techniques. The analysis of the material by diffraction contrast in 002 dark field conditions and by atomic column resolved high angle annular dark field-scanning TEM reveal the presence of a low Sb content InSbAs continuous layer with scarce Sb-rich InSbAs agglomerates. The intensity profiles obtained by both techniques point to Sb segregation during growth. This segregation has been quantified using the Muraki segregation model obtaining a high segregation coefficient R of 0.81 towards the growth direction. The formation of a continuous InSbAs wetting layer as a result of a SML deposition of Sb on the InAs surface is discussed.

Keywords: InSb/InAs sub-monolayer quantum dots, 002 dark field analysis, atomic column HAADF-STEM, composition analysis, Sb segregation

(Some figures may appear in colour only in the online journal)

Introduction

InSb is considered one of the superior candidates in terms of electronic and optoelectronic applications compared to other binary III–V semiconductors due to its low electron effective mass of $0.013m_0$ and very high electron mobility of 77 000 $cm^2\,V^{-1}\,s^{-1}$ [1, 2]. Beside to this high electron mobility, InSb also holds a high hole mobility of 850 $cm^2\,V^{-1}\,s^{-1}$ and hence supports designing low-power, high-speed optoelectronic devices [3]. The design of these highly efficient devices requires InSb to be grown epitaxially on other III–V [4–7] or II–VI [8] semiconductor materials to produce quantum confined structures which act as the driving source of those devices. In particular, when InSb is epitaxially grown on InAs using molecular beam epitaxy (MBE) using the conventional epitaxy (CE) mode where both the In and the Sb shutters are opened simultaneously, type II self assembled Stranski–Krastanov (SK) quantum dots (QDs) are formed as a consequence of the large lattice mismatch of 6.9% [9, 10] between them. In order to improve the performance of optoelectronic devices based in InSb/InAs QDs such as lasers or photo-detectors, the carriers confinement in the active nanostructures should be improved, and for this the size of the QDs should be reduced. Buried InSb/InAs QDs grown at 320°C by CE have been reported to have base diameter as big as ∼15 nm for an InSb deposition thickness of 1.6–2 monolayer (ML) [11]. Despite growth parameters such as temperature, deposition thickness, V/III flux ratio, etc alter the QDs size and shape, it is difficult to reduce the size of the nanostructures as much as desired using CE. Additionally, in

the growth of QDs by SK a wetting layer (WL) is formed around the QDs. In some devices, the emission from this WL may produce an interference with the desired emission, reducing the efficiency of the device. It has been reported that the population of WL states leads to a sub-linear increase of the population inversion in the QDs with carrier density, reducing the gain and differential gain for a given carrier density [12]. In order to avoid this WL and to try to reduce the size of the QDs formed different growth approaches need to be considered. One of these approaches is the migration enhanced epitaxy (MEE) technique [13]. This technique consists of an alternate supply of the pure constituent atoms [14] instead of the simultaneous supply used in CE. This method has been proposed as a plausible approach for producing high density coherent InSb/InAs QDs with better size homogeneity over CE [15] and with emission in the mid-infrared (MIR) wavelength range of 3–5 μm [16]. Whereas the critical InSb deposition thickness for SK QDs formation using CE is of 1.7 ML [17], the exposure of the InAs surface to an antimony Sb_4 flux with the In shutter closed allows considering nominal depositions of InSb within the range of 0.6–1.4 ML [16]. Although often the deposition of several of these InSb sub-monolayer (SML) insertions are used to form the QDs, the growth of only one of these insertions may lead to QDs with a very small size [18]. QDs formed by InSb SML insertions in InAs have been reported to have sharper emission spectra and better modal gain [19, 20]. Because of this, InSb SML QDs have been used to design various optoelectronic devices, such as MIR lasers [21, 22], light emitting diodes (LEDs) [23], etc.

However, the effect of this alternative growth procedure on the structural properties of the InSb/InAs nanostructures grown has been mainly realized using indirect experimental analyses, such as reflection high-energy electron diffraction (RHEED) [16, 22, 24], x-ray diffraction (XRD) [16, 22], and photoluminescence (PL) [16, 18, 22, 24], and in few cases low magnification transmission electron microscopy (TEM) [16, 18, 22]. Because of this, the information obtained is inconclusive to enable a correlation between the changes in optoelectronic properties to differences in the nanostructures sizes and shapes [25, 26]. The analysis of the Sb distribution in InSb/InAs SML insertions is challenging due to the low Sb content in the material and, because of this, advanced techniques with high spatial resolution need to be used. In this regard, aberration corrected TEM analyses, particularly high angle annular dark field (HAADF)-scanning TEM (STEM) analysis [27], can be used as the direct characterization approach. HAADF-STEM is widely used in the analysis of semiconductor materials because of its capability to provide direct compositional information associated to the average *Z*-contrast within atomic column-by-column. For example, this technique has been successfully used to analyze the segregation nature of Sb at atomic column scale in $GaAs_xSb_{1-x}$/GaAs QDs [28], various levels of Sb incorporation into GaAs/GaSb/InAs/GaAs QD heterostructure [29], compositional distribution of In within $In_xGa_{1-x}As$/GaAs heterostructure [30], etc. The advantageous characteristics of HAADF-STEM signify it as an ideal analyzing technique to obtain direct information at atomic column scale of a wide variety of materials, contributing to their further development.

In this work, we analyze quantitatively the Sb distribution in a heterostructure consisting of InSb SML insertions in InAs grown by MEE. Both low magnification diffraction contrast based 002 dark field (DF) analysis and atomic column resolved HAADF-STEM analysis have revealed that the material consists of InSb(As) layers with random agglomerated regions with a maximum average Sb composition of ~10%. The formation of the unexpected Sb distribution found is discussed.

Materials and methods

The InSb/InAs heterostructure has been grown using the MEE technique on n-InAs (001) substrate. The heterostructure consists of ten InSb layers grown at 430 °C. Here, an InSb layer deposition is performed by exposing Sb_2 flux on an InAs surface for 20 s, followed by In exposition of 5 s and then again Sb_2 flux for 6 s. Next, each InSb layer is covered by a 20 nm barrier layer of InAs, grown at 430 °C. Finally, a 100 nm InAs capping layer is grown at 470 °C as the topmost layer. The substrate temperatures T_s have been measured by calibrated thermocouple, and the growth has been monitored by *in situ* RHEED. The post-growth XRD analysis has revealed a reduced ultra-low InSb deposition of 0.65 ML at each case and hence, this 0.65 ML deposition thickness has been used to obtain Sb compositional distribution in this work.

The electron transparent specimens for the TEM analyses have been prepared by the combination of mechanical thinning and precision ion polishing system associated Ar^+ ion milling. The diffraction contrast analysis has been carried out using a JEOL JEM 2100 microscope at an operating voltage of 200 kV. A double aberration corrected FEI Titan Cubed Themis microscope has been used for the atomic column resolved HAADF-STEM analysis at an operating voltage of 200 kV. The parameters used for image acquisition are: $C_s = 1$ μm, $C_5 = 5$ mm, HAADF detector inner angle = 63.8 mrad, convergence angle = 16.04 mrad, camera length = 91 mm and defocus = 0.083 μm. The HAADF-STEM images have been taken from the regions that possess average relative log-ratio value of $t/\lambda \sim 0.58$, measured using zero-loss peak electron energy loss spectroscopy (EELS). Here, t is the thickness of that region and λ is the corresponding electron mean free path (MFP). In our case, the MFP has been calculated to be ~62.14 nm using the equations mentioned in [31]. Hence, the corresponding average specimen thickness has been found to be ~36 nm.

A simulated HAADF-STEM image of InAs/InSb/InAs structure along [110] zone axis has been generated using the same model arrangement as in [32], but with aforementioned HAADF-STEM imaging parameters. Here, the corresponding computations have been performed with respect to the experimental specimen thickness of 35 nm. Moreover, HAADF-STEM images of InSbAs agglomerates with cubic form with 5 nm of side within the 35 nm specimen with

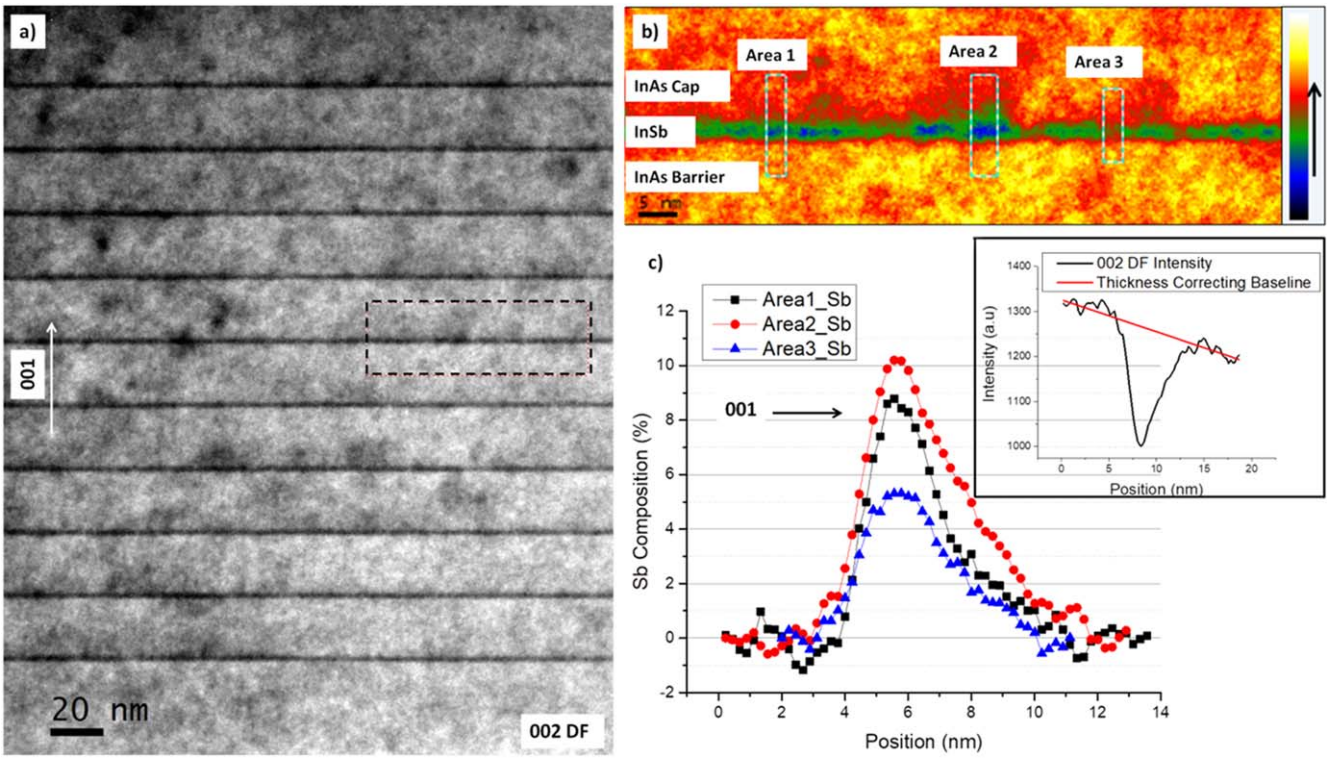

Figure 1. (a) 002 DF TEM image of the complete InSb/InAs ([001]) hetero-structure where no structural defects are found. (b) 002 DF TEM image of a single InSb layer obtained from the black rectangle area in figure 1(a) and represented in temperature grade while containing different analyzing areas termed as Area 1–3. The color scale provides intensity (a.u) that increases from bottom to top in the scale. (c) Sb composition (%) profiles obtained from 002 DF TEM image intensities within Area 1–3 along [001] growth direction. The inset represents the subtraction process of the specimen thickness variation induced signal from a 002 DF intensity profile.

varying Sb composition have also been performed to see the corresponding solo effects induced by an agglomerate. All the relevant computations associated to the simulations have been accomplished using SICSTEM software. This SICSTEM software runs on CAI supercomputer in University of Cádiz (UCA). The working principle of the SICSTEM software can be read in [33]. Aberration corrected spatial incoherence has also been taken into account during these simulations [34].

Results and discussion

As the initial step, the structure quality of the InAs/InSb/InAs hetero-structure grown in [001] direction has been evaluated using diffraction contrast based TEM analysis. Figure 1(a) shows a chemical sensitive 002 DF diffraction contrast TEM image of the investigating sample. Here, the 10 darker layers represent the InSb layers, while the intermediate brighter layers depict the InAs matrices. As per the DF TEM image, no dislocation or other structural defect is observed in this heterostructure. 002 DF TEM images provide information on the composition distribution in the InSb layers. For the Sb distribution analysis, a segment within a black rectangle area on an InSb layer in figure 1(a) has been chosen and is demonstrated in figure 1(b). Figure 1(b) is shown in temperature color grade in order to enhance the 002 DF based intensity variations in arbitrary unit (a.u.). As it can be observed, the non-uniform intensity range within the InSb layer assures the presence of some discontinuity. Some regions on the InSb layer have been marked as Areas 1–3, where Area 2 possesses the lowest intensity and the Area 3 holds the highest intensity indicating different Sb content. The 002 DF intensity variation within the InSb layer can be used to quantify the composition distribution of Sb using the kinematical diffraction theory [35]. The assumptions of the kinematical diffraction theory include that there is no interaction between the transmitted and the diffracted waves and that absorption effects are negligible, which are only normally fulfilled for unattainably thin (∼1 nm) specimens. However, this theory has shown to offer plausible results when applied to reasonably thin TEM experimental specimens [36, 37]. According to the kinematical diffraction theory, the intensity parameter I_{002} in a 002 micrograph of InSb/InAs can be approximated by the electron scattering factors of In, As and Sb, therefore for the $InSb_xAs_{1-x}$ region it can be written as:

$$I_{002} \propto [f_{\mathrm{In}} - f_{\mathrm{As}} - x(f_{\mathrm{Sb}} - f_{\mathrm{As}})]^2, \quad (1)$$

where f_{In}, f_{As} and f_{Sb} represent the electron scattering factors of In, As and Sb, respectively. These factors are roughly proportional to the corresponding atomic numbers and hence, can be replaced by Z_{In}, Z_{As} and Z_{Sb}, respectively [38]. The obtained intensity I_{002} can be normalized in terms of the

intensity generated from the binary InAs alloy by:

$$\alpha = I_{002}/I_{\mathrm{InAs}}. \quad (2)$$

Substitution of equation (1) after *Z*-value replacement to equation (2) provides normalized intensity which latter can be converted to Sb composition (x).

It should be noted that 002 DF intensities in figure 1(b) contain information related to the specimen thickness in addition to the chemical composition. Consequently, to obtain Sb induced chemical information using the aforementioned quantification process from the Areas 1–3 on figure 1(b), the thickness contribution needs to be compensated beforehand. The inset of figure 1(c) represents the compensation process applied on a 002 DF raw intensity profile along [001] growth direction from left to right, where the red curve denotes the baseline that subtracts the thickness variation from the corresponding 002 DF raw intensity profile in black. The specimen thickness compensated Sb composition profiles of Areas 1–3 are shown in figure 1(c). As it can be observed, the areas of smaller intensity (Areas 1 and 2) have larger average Sb composition than the most intense Area 3. Here, the Sb average composition fluctuates from ∼5% (Area 3) to 10% (Area 2) indicating that the InSb layer in figure 1(b) does not grow with uniform composition and the corresponding blue nucleated regions are in fact InSbAs agglomerates. It should be mentioned that the kinematical approximation works well in terms of image contrast assumption as long as the x composition falls below 0.2 (20%), as suggested in [38], therefore it is an adequate approximation to be used in our study. The thickness of the InSbAs layer has been estimated through the FWHM of the 002 DF intensity profiles, and it has been found to be within the range of ∼2.6–3.7 (±0.2) nm exhibiting that Sb is dispersed within agglomerates of variable thicknesses and compositions. It has been reported that the possibility of Sb composition as low as ∼10% within $InSb_xAs_{1-x}$ layers may possess either type I or type II band alignment in terms of strain, concentration and phase separation [39]. In case the agglomerates adapt type I band alignment they may face a reduced optoelectronic application range due to a shorter carrier lifetime than that of the type II band alignment [40].

Our results by 002 DF have shown that the growth by MEE of InSb insertions in InAs produces a continuous InSb layer that includes some Sb agglomerations. The Sb distribution found is far from that expected for the growth approach used, where controlled size QDs without WL are expected. The MEE technique was initially proposed to improve atoms surface migration to allow low temperature MBE growth of semiconductor heterostructures, and demonstrated for AlAs/GaAs QWs [13]. Afterwards, this technique has been used as an alternative to the SK growth mode to obtain QDs [41], as SK QDs normally have size variability and weak carrier confinement due to the WL around the QDs [15]. Thus, QDs have been formed by multiple SML InSb depositions in InAs [22, 42]. Low magnification TEM images suggest that, when the initial InSb SML is grown on InAs, InSb-enriched islands are formed [18]. The strain due to this initial layer produce that subsequent InSb insertions grow on top of this initial one, forming QDs without WL. However, in InAs/GaAs SML QDs formed by 10 InAs-GaAs alternate depositions, strain sensitive TEM images suggests that some In is located in the region between the QDs [19]. Unfortunately, the analysis of the composition distribution in the material was not carried out in that study. In this framework, the analysis carried out in the present work shows that a few nm thick continuous WL is formed from the initial Sb SML insertion. The InSb layer thickness of this sample estimated from the simulation of the experimental XRD rocking curve is of 0.65 ML. This means that, in order to obtain a continuous few nm thick WL from this SML insertion, both a lateral movement of the Sb atoms and the upwards segregation during growth are required. Based on RHEED specular spot intensity (SSI) analyses, it has been suggested that Sb segregation could be responsible for the WL formation in SML InSb/InAs QDs QDs [24]. Segregation in Sb containing III–V semiconductors has been widely reported in the literature [28, 37, 43]. The segregation nature of Sb tends to be highly influenced by the corresponding growth temperature observed in various previous works [24, 44, 45], where a high growth temperature facilitates a high Sb segregation. In relation to this, a closer look at figure 1(c) shows that the compositional profiles obtained in this work show asymmetric edges along the growth direction ([001]). Thus, it can be seen that the interfaces between the overgrown InAs cap and the InSb layer are more graded compared to the interfaces between the InSb layer and the undergrown InAs barrier. This points out Sb segregation taking place along the growth direction ([001]) during growth. In order to quantify the Sb segregation in the material to understand the Sb distribution found, high resolution TEM analysis have been carried out.

For this, different regions of the InSb/InAs layers have been analyzed by aberration corrected HAADF-STEM, which is sensitive to the average Z number in the material. Figure 2(a) shows a HAADF-STEM image of one of the InSb (As) layers where the atomic column III–V pairs (dumbbells) along [110] zone axis can be observed. Unwanted microscope detector contributing vacuum level signal (black level signal) has been removed from this and each acquired image using the method described in [46]. As it can be observed, the InSb (As) layer is not clearly distinguishable in the image. This is likely due to a low Sb composition induced enhancement at the corresponding Z-intensity, in agreement with the low average Sb composition found in the 002 DF profiles in figure 1(c). In order to obtain an estimation of the increase in intensity expected in the HAADF-STEM analysis of the material, a HAADF-STEM image simulation of a InAs/InSbAs/InAs heterostructure along [110] zone axis has been computed. A value of the Sb composition in the InSbAs layer of 10% Sb has been chosen for the simulation following the similar result of ∼10% Sb obtained from the 002 DF analysis, and a thickness of 35 nm is considered, close to the one of the experimental specimen measured by zero-loss peak EELS. As it can be observed in the HAADF-STEM simulated image in figure 2(b), the InSbAs layer located at the central part of the image is hardly visible with the naked eye. Because of this,

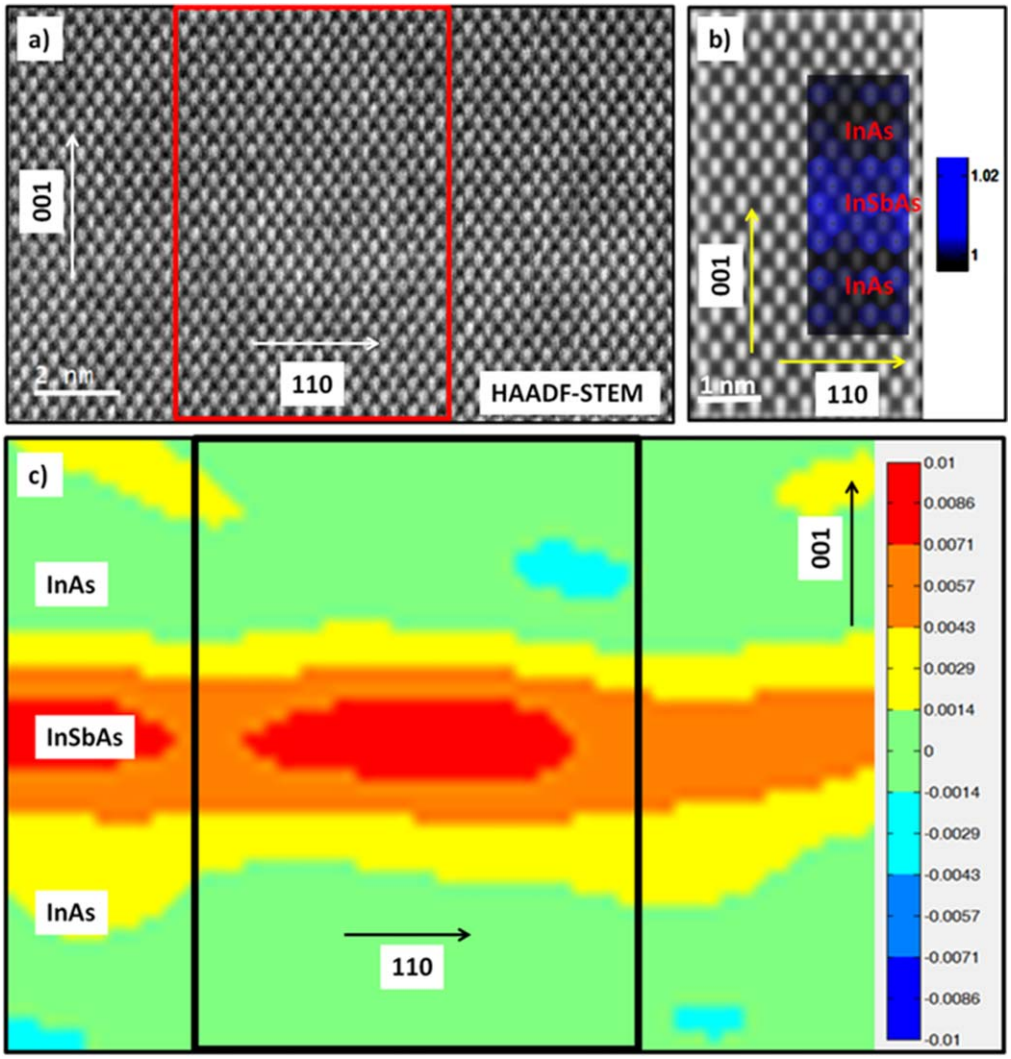

Figure 2. (a) Atomic column resolved experimental HAADF-STEM image of InSb/InAs ([001]) heterostructure along [110] zone axis. (b) Partial superposition of an intensity ratio (R') map on a simulated InAs/InSbAs/InAs ([001]) heterostructure as per 10% Sb with a specimen thickness of 35 nm. (c) Colored lattice displacements map assuring the presence of central InAsSb layer in red as per figure 2(a). The color scale designates induced lattice displacements quantitatively in the heterostructure.

we have used the tool quantitative HAADF (qHAADF) [47] to quantify the atomic column-by column intensities in the HAADF-STEM simulated image. The qHAADF tool has been previously used in the literature to compare the atomic column-by-column intensities integrated within a region of interest (ROI) with the average atomic column integrated intensity of a homogenous (reference) area in order to calculate atomic column-by-column composition in the ROI area. For example, in previous works, it has been used to analyze the Sb composition in GaAs capped GaSb nanostructures [28] and GaAsSbN capped InAs QDs [48]. In our case, an atomic column-by-column color map in terms of the intensity ratio $R' = I_{\mathrm{InSbAs}}/I_{\mathrm{InAs}}$ has been generated from the HAADF-STEM simulated image in figure 2(b) using the aforementioned qHAADF tool and the image pixel integration area corresponding to Mask 3 in [32]. This map has been partially superimposed on the corresponding region on the HAADF-STEM simulated image, illustrated in figure 2(b). As it can be observed, the InSbAs layer in blue can be distinguished from the surrounding InAs matrix in black, although the increase in intensity related to including 10% Sb in the InAs layer regarding the InAs reference region is remarkably small, of only 1% approx. This justifies that the InSbAs layer in the experimental HAADF-STEM image is not clearly visible. In order to do a reliable interpretation of the information contained in the image when such small composition-related intensity variations are obtained, the intensity due to other possible sources need to be carefully taken into consideration. In this case, the main factor to be taken into account is the thickness of the sample, as it has a strong effect in the intensity of HAADF-STEM images [32, 49, 50]. Normally, the thickness in TEM specimens prepared by the conventional method of thinning to electron-transparency is reduced gradually when moving to the edge of the specimen. However, local thickness variations may also be produced during the specimen preparation process that could have a strong effect in our analysis. Because of this, the interpretation of the intensity variations in the

HAADF-STEM experimental image including the compensation of the thickness effect needs to be done locally, preferably over few atomic columns, and not along the full image, to improve the precision of the measurements. For this, the initial step is finding the position of the InSb layer in the HAADF-STEM image.

In order to locate the InSb layer in the experimental HAADF-STEM image and to obtain additional information from the heterostructure, we have performed the analysis of the lattice displacements in the material using the geometric phase analysis (GPA) method [51] due to the fact that Sb atoms are larger than As atoms which may introduce strain at the lattice planes of the material. This analysis is not affected by local variations in the thickness of the specimen as it works with the position of the atomic columns and not with the HAADF-STEM intensity. Figure 2(c) shows a colored map of lattice displacements calculated using the InAs barrier layer (lower InAs layer) as the reference, and generated as per the HAADF-STEM image in figure 2(a). In figure 2(c), the area within the black rectangle represents the area within the red rectangle in figure 2(a). As it can be observed, a strained layer in red exists at the center of the figure 2(c), where red color symbolizes maximum lattice displacements of only ∼1% (0.01). The lattice mismatch of an InSbAs layer with 10% Sb as measured by 002 DF with regards to a InAs layer is 0.69%, therefore this outcome points to the presence of low strained InSbAs agglomerates in red and hence, the InSb layer within the HAADF-STEM image. Similar to the 002 DF TEM image in figure 1(b), the InSbAs agglomerates in the strain map reveals an average thickness of ∼3 nm, broader than the nominal InSb layer thickness of ∼0.21 nm (0.65 ML), indicating that Sb is highly segregated along the growth direction. This high Sb segregation is likely to be the major reason to form the undesired large agglomerates observed instead of the SML QDs. In order to quantify the segregation in the material at the growth temperature of 430 °C, the corresponding Sb segregation coefficient must be realized to achieve the necessary boundary parameters appropriate for SML QDs formation.

In order to analyze the Sb composition distribution in the growth direction within the InSb layer and corresponding Sb segregation coefficient, dumbbell-by-dumbbell HAADF-STEM raw intensities along the [001] growth direction have been obtained from the red rectangle area within the HAADF-STEM image in figure 2(a) and it has been plotted from left to right in black in the inset of figure 3. Assessing the negative slope of this inset profile from left to right, it suggests that within the red rectangle area the specimen thickness changes from bottom to top in the HAADF-STEM image in figure 2(a). To compensate it, a baseline in red has been plotted in the inset of figure 3 that subtracts the thickness variation contribution from the HAADF-STEM signal. Afterwards, ML-by-ML Sb composition from the HAADF-STEM intensity profile has been obtained with the formulations offered in [30, 47], where atomic column resolved composition values are generated from the intensity ratio R' as per a linear regression equation. The obtained Sb composition values have been plotted in figure 3 in black. Here, the maximum average Sb in a ML has been found to be ∼10%, as found in the 002 DF analysis in figure 1(a). A close observation to the HAADF-STEM intensity profile in figure 3 shows that it possesses an asymmetric shape that is graded between the InSb layer and the overgrown InAs layer, indicating the presence of Sb segregation along the [001] growth direction, as expected. In order to quantify this Sb segregation in the HAADF-STEM analysis, we have considered a widely used theoretical segregation model developed by Muraki *et al* [52]. The Muraki model was originally emerged to analyze the quantum well induced III–V material segregation that quantified the segregation phenomenon both inside the well and between the well and the overgrown capping layer along the growth direction. Some successful Muraki model induced segregation analyses include Sb distribution analysis in $InAs/InAs_{1-x}Sb_x$ type-II superlattices [37] and GaInSb/InAs strained-layer superlattices [53], or In distribution analysis in $In_xGa_{1-x}As/GaAs$ heterostructure [30, 54]. For segregation analysis, the ML sequencing has been rearranged primarily as per the model requirement where the maximum HAADF-STEM Sb composition of ∼10% has been positioned at ML1 and so on and so forth, illustrated in figure 3. Muraki model induced Sb segregation between InSb and overgrown InAs layer has been quantified using the following formula:

$$x = x_0(1 - R^N)R^{z-N}, \text{ for } z \geqslant N. \quad (3)$$

Here, x is the average ML-by-ML Sb composition, x_0 is the nominal InSb composition, z is the number of analyzing MLs at ML $\geqslant 0$, R is the segregation coefficient and N is the nominal thickness of the InSb layer.

This fitting curve obtained in our analysis has been demonstrated in figure 3 in red (in%) on the experimental plot in black. The best fit between the experimental and Muraki model has been obtained for a R value of 0.81 at a nominal InSb deposition thickness of 0.72 ML which is slightly deviated from XRD nominal deposition thickness value of 0.65 ML. A segregation coefficient R of 0.81 means that each next ML possesses 81% Sb composition of the immediately previous ML at ML > 0, which is a large variation regarding an intended composition profile. The R value obtained in our analysis has been found to be compatible to the segregation coefficient value of 0.82 measured indirectly by RHEED in SML InSb/InAs insertions grown at 430 °C [24].

It is worth highlighting that the analyses of the InSb/InAs layers by HAADF-STEM have shown the existence of small InSbAs agglomerates where the average Sb composition is measured as 10%, in good agreement with the observations by 002 DF. However, due to the projection over the sample thickness that occurs during the acquisition of (S)TEM images, the Sb content measured is not the actual Sb composition in the agglomerates but averaged with the composition in the WL. With the aim of obtaining a more realistic value of the actual Sb composition in the agglomerates, we have carried out HAADF-STEM image simulations. For this, we have considered a 35 nm thick specimen of InAs structure that includes a cubic InSbAs agglomerate of 5 nm. In order to obtain an estimation of the actual Sb content in the agglomerates to be considered for the design of the

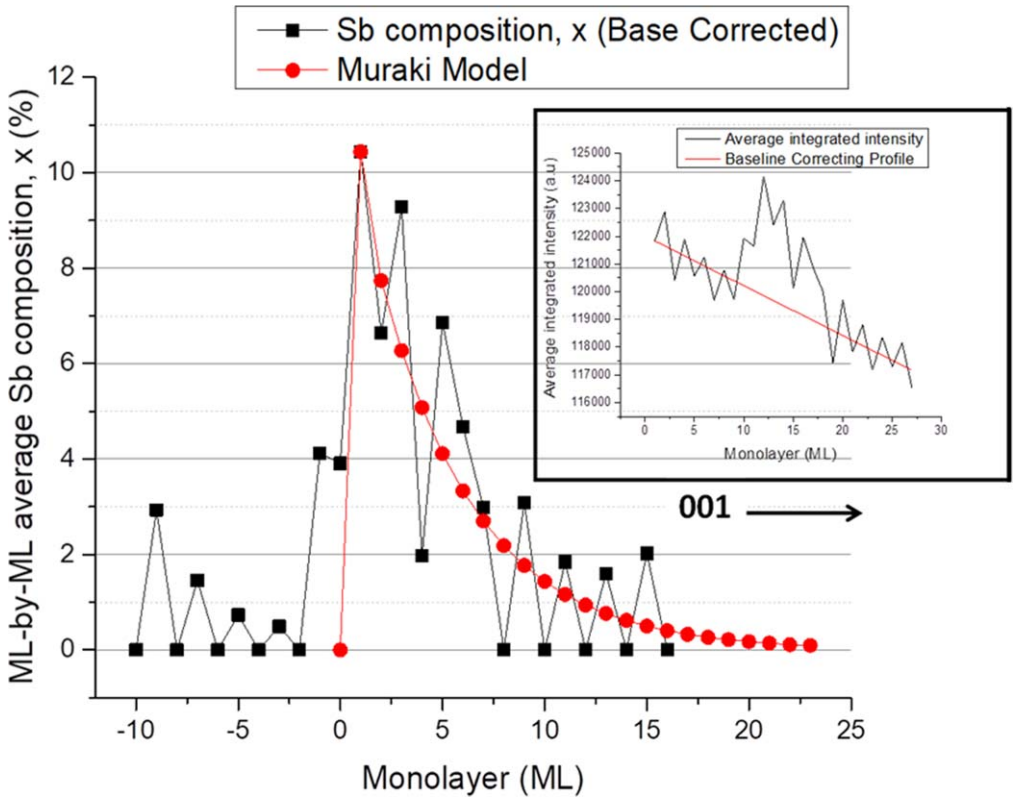

Figure 3. ML-by-ML average Sb composition (%) profile in black along [001] growth direction associated to the HAADF-STEM image in figure 2(a) with Sb segregation profile in red as per Muraki model with a segregation coefficient R of 0.81. The inset represents the subtraction process of the specimen thickness variation induced signal from the HAADF-STEM intensity profile.

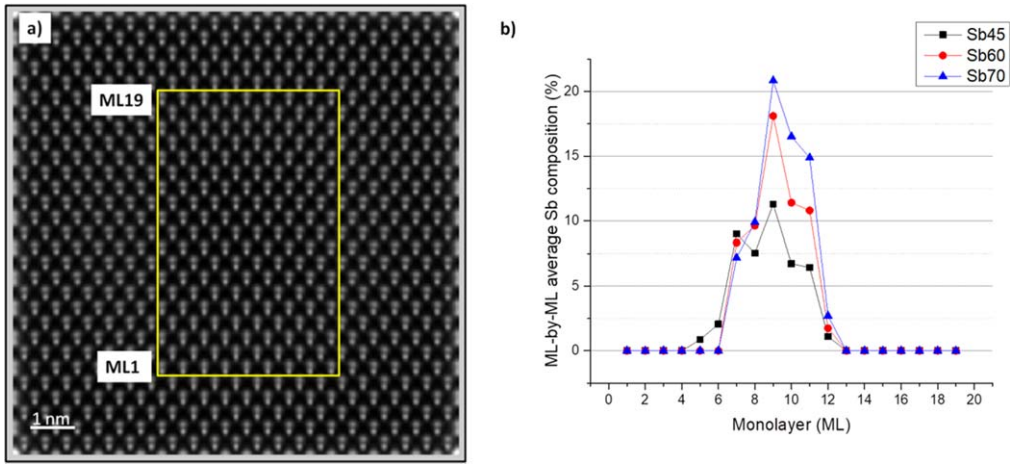

Figure 4. (a) Atomic column resolved simulated HAADF-STEM image of a 35 nm thick InAs structure where a 5 nm InSbAs agglomerate with Sb composition 45% is embedded. The yellow rectangle represents Sb composition quantification area. (b) ML-by-ML average Sb compositions calculated within the yellow rectangle in figure 4(a), where the profiles associated to 45%, 60% and 70% Sb have been represented by black, red and blue lines, respectively.

structure used in the simulated images, we have made some rough calculations. The intensity in HAADF-STEM images can be calculated as $I = k^{*}Z^{n}$, where Z is the average atomic number of the material, $n \sim 2$ and k is a constant. The simulated HAADF-STEM intensity in figure 2(b) associated to $InSb_{0.1}As_{0.9}$ layer (with average Z of 41.9) can be used to obtain an estimation of the constant k. With this constant and assuming that the experimental HAADF-STEM intensity in the region of the InSbAs agglomerates could be approximated to the sum of the intensity due to the InSbAs agglomerate plus the intensity corresponding to the WL in front and behind it (with 5% Sb as observed experimentally), we have obtained a rough estimation of 58% Sb associated to the average Z in the InSbAs agglomerate. Analogous calculations have been

carried out considering the equations that govern the 002 DF image formation, obtaining similar results. Thus, we have computed simulated images containing InSbAs agglomerates with 45%, 60% and 70% Sb. A corresponding cross-sectional HAADF-STEM simulated image has been demonstrated in figure 4(a) which contains the agglomerate inside with 45% Sb composition. Figure 4(b) represents ML-by-ML averaged line profiles of Sb compositions (45%, 60% and 70%) calculated within the yellow rectangle in figure 4(a) using the same methodology as used above for the experimental images. It should be pointed out that spatial incoherence has been considered in the simulations in order to obtain more realistic images, and this deviates the obtained composition profiles from ideal ones. As it can be observed, the Sb composition measured in the simulated HAADF-STEM images is smaller than the corresponding to the InSbAs clusters, as expected. In particular, it can be seen that a single agglomeration with 45% Sb (represented by the black profile) generates average Sb composition of ∼10%, which is close to the experimental value obtain in our study. This means that the analyzed material may contain InSbAs agglomerates with Sb content much larger than the corresponding to the InSbAs wetting layer. A more precise analysis would require including the WL with low 5% Sb composition in our simulations (which is expected to increase the measured Sb composition), and also considering the effect of placing the agglomerates in different positions regarding the specimen thickness (in the simulations above, the agglomerates are right in the center of the specimen), although this is out of the scope of our study. On the other hand, it is worth mentioning that we have found a small density of agglomerates in the layer, therefore the authors think that due to the small specimen thickness, the probability of having more than one cluster overlapped in each of the regions where the average Sb content is measured as 10% is very small. If there were more than one cluster in some of the regions, then the Sb content in the agglomerates would be smaller than the values obtained in figure 4(b).

Our results have shown a clear deviation of the obtained Sb distribution in the SML InSb/InAs layers with respect to the heterostructure design. Thus, a low density of Sb-rich InSbAs agglomerates in a thick $InSb_{0.05}As_{0.95}$ WL layer has been found, with a Sb vertical profile in good agreement with a segregation process. Segregation is considered as the exchange of surface atomic species with subsurface segregant atoms, producing a floating layer at the growth surface that has been observed experimentally for a number of III–V semiconductors [55–57]. This floating layer strongly affects the growth dynamics in semiconductor alloys. For example, it has been reported that in a GaSb/GaAs heterostructure during GaAs capping Sb containing floating layer is generated due to Sb segregation that forms a discontinuous layer with low volume GaAsSb nanostructures [28]. The thermodynamic treatment to account for segregation include the balance of the surface and bulk chemical potentials of the atoms involved [58]. Thus, if the movement of one atom from the bulk to the surface yields a positive energy, the equilibrium surface concentration will be higher than the concentration of the bulk material. Simple thermodynamic models of segregation in epitaxial semiconductor layers would only include the entropy term and the chemical energy as the contributions to the free energy, plus a term corresponding to the pseudomorphic elastic energy [59]. However, these models would predict an increase of segregation when decreasing the growth temperature, which is the opposite behavior as that observed experimentally [52, 60]. The reason for this is that the growth of semiconductor heterostructures is often carried out under non-equilibrium conditions, where additional parameters affect the final composition distribution. Thus, it has been shown that for relatively low growth temperatures (400 °C), the epitaxial growth of GaInAs/GaAs using large growth rates (1 Ml s^{-1}) imposes kinetic limitations to the segregation process, with clear deviations from the composition profiles obtained using only thermodynamic considerations [61]. Because of this, kinetic models have been developed [61–63], including terms such as the incorporation rate of new atoms in the epitaxial growth, which depends on the impinging flux—desorption rate. Other authors have included the surface diffusion in the kinetic model [64], demonstrating that only including this phenomena the theoretical model agrees with experimental results of Si/SiGe layers. Additionally, it is worth noting that these atoms movement at the surface of a growing semiconductor material may be affected by surface relaxations/reconstructions which are not generally taken into account.

Regarding Sb, calculated exchange energies of $E_{Sb/As}^{bulk->surface} = 1.68$ eV and $E_{Sb/As}{}^{surface->bulk} = 1.75$ eV [65] in InAs agree with the strong tendency of segregation observed experimentally [28, 37]. However, fitting experimental data of segregated Sb composition profiles in III-Sb complex heterostructures often requires the use of some of the kinetic models mentioned above [66], in some cases including parameters such as surface diffusion [67]. A kinetic model predicting anion incorporation in InAsSb has been reported, including the effects of As desorption, Sb segregation, and Sb displacement by As [62]. In that work, it is discussed that as the desorption rates for As and Sb are slow (typically less than the arrival rate of In), these terms have a negligible impact in the calculations. Additionally, surface reconstructions have been reported to have a strong impact in the Sb final distribution. Compositional grading at InAs-on-GaInSb heterojunctions caused by Sb segregation have shown to be quantitatively linked with the anion stoichiometry of the GaInSb surface reconstructions that serve as the templates for interface formation [53]. Calculated *ab initio* surface reconstruction phase diagrams of As-exposed InSb(001) show that three main configurations stabilized by subsurface As occupy the majority of chemical potential space, providing evidence of a thermodynamic driving force for Sb-As intermixing and Sb-segregation [68].

Growing good quality InSb QDs is challenging due (among others) to the low bond-energy of In-Sb [69, 70]. In spite of this, coherent InSb QDs with higher dot density have been obtained by MEE [42]. In MEE, the atoms lateral movement on the growing surface has been reported to be

improved over CE because the migrating materials have atomic form rather than III–V molecules-like structures [13]. In InSb/InAs, this atomic form of Sb has been reported to allow an effective As/Sb exchange during the Sb exposure of the InAs surface [15], enhancing the attachment of Sb to the growing surface. Thus, RHEED experiments [71] have shown that the exposure of an InAs surface to a Sb flux produces, after a short delay time, the substitution of As atoms by Sb, forming a thin InSb layer. After this, the behavior of the RHEED signal suggests the self-formation of extremely small InSb islands driven by the presence of high elastic strains, according to the Volmer–Weber mechanism. Since there is no incident Sb flux, partial re-evaporation of a significant fraction of Sb atoms in the InSb layer is also expected. In our work, it seems that kinetical limitations (mainly the short time available until the In shutter is opened) prevented this 3D transformation from happening to a large extent, leaving a fraction of the Sb atoms distributed along the surface. The subsequent growth of the InAs cap layer on the Sb distribution initially formed gives place to a strong Sb segregation, producing the relatively thick InSbAs layer observed in our study. Sb segregation has shown to have a large influence in the final morphology and composition distribution of a wide variety of Sb-containing nanostructures, including important deviations from the expected design [72, 73] such as those found in our study. More importantly, remarkable unexpected electronic consequences of Sb segregation [74] have been revealed using pseudopotential calculations. Because of this and in order to improve the QDs characteristics to further improve the PL emission of the material analyzed in the present work, the growth conditions of these SML InSb/InAs QDs still need to be optimized. A reduction in the segregation coefficient of almost 20% has been found when reducing the SML InSb/InAs growth temperature from 500 °C to 410 °C [24]. The PL emission efficiency of InGaSb/GaAs has been reported to dramatically improve for samples where the GaAs cap growth temperature is reduced [75]. Inspired by this finding, we have performed similar analyses to form InSb/InAs SML QDs with reduced InAs growth temperatures and the corresponding outcomes would be published elsewhere.

Conclusions

The structural properties of a SML InSb/InAs heterostructure grown by MEE have been analyzed by TEM techniques. We have found that the active layer consists of a $InSb_{0.05}As_{0.95}$ layer with thickness in the range ~2.6–3.7 (±0.2) nm that contains Sb- rich InSbAs agglomerates. We have measured a Sb segregation coefficient of 0.81 using the Muraki model, in good agreement with previous measurements at the same growth temperature. Our results show that despite MEE is a promising technique for the growth of WL-free, small QDs for improved carriers confinement, the growth conditions can still be improved in order to obtain optimized InSb QDs.

Acknowledgments

This work was supported by European Union (UE) (post graduate research on dilute metamorphic nanostructures and metamaterials in semiconductor photonics (PROMIS) Horizon 2020 initial training network (ITN) project with Grant agreement No. 641899), Spanish MINECO (projects TEC2014–53727-C2-2-R and TEC2017-86102-C2-2-R) and the Junta de Andalucía (PAI research groups TEP-946 INNANOMAT and TIC-145). Co-financing from UE-FEDER is also acknowledged.

ORCID iDs

Atif A Khan https://orcid.org/0000-0002-0322-5024
M Herrera https://orcid.org/0000-0002-2325-5941
N Fernández-Delgado https://orcid.org/0000-0002-6295-2475
D F Reyes https://orcid.org/0000-0002-3101-5251
J Pizarro https://orcid.org/0000-0002-4295-6743
E Repiso https://orcid.org/0000-0003-1895-7444
A Krier https://orcid.org/0000-0003-4098-5206
S I Molina https://orcid.org/0000-0002-5221-2852

References

[1] Caroff P, Wagner J B, Dick K A, Nilsson H A, Jeppsson M, Deppert K, Samuelson L, Wallenberg L R and Wernersson L E 2008 High-quality InAs/InSb nanowire heterostructures grown by metal-organic vapor-phase epitaxy *Small* **4** 878–82
[2] Wang Y, Chi J, Banerjee K, Grützmacher D, Schäpers T and Lu J G 2011 Field effect transistor based on single crystalline InSb nanowire *J. Mater. Chem.* **21** 2459–62
[3] Nilsson H A, Deng M T, Caroff P, Thelander C, Samuelson L, Wernersson L E and Xu H Q 2011 InSb nanowire field-effect transistors and quantum-dot devices *IEEE J. Sel. Top. Quant. Electron.* **17** 907–14
[4] Moiseev K D, Parkhomenko Y A, Ankudinov A V, Gushchina E V, Mikhaĭlova M P, Titkov A N and Yakovlev Y P 2007 InSb/InAs quantum dots grown by liquid phase epitaxy *Tech. Phys. Lett.* **33** 295–8
[5] Bomphrey J J, Ashwin M J and Jones T S 2015 The formation of high number density InSb quantum dots, resulting from direct InSb/GaSb (001) heteroepitaxy *J. Cryst. Growth* **420** 1–5
[6] Tenev T G *et al* 2009 Energy level spectroscopy of InSb quantum wells using quantum-well LED emission *Phys. Rev.* B **79** 085301
[7] Namazi L, Ghalamestani S G, Lehmann S, Zamani R R and Dick K A 2017 Direct nucleation, morphology and compositional tuning of $InAs_{1-x}Sb_x$ nanowires on InAs (111) B substrates *Nanotechnology* **28** 165601
[8] Welzenis R G V and Ridley B K 1984 On the properties of InSb quantum wells *Solid-State Electron.* **27** 113–20
[9] Bert N A, Nevedomskiy V N and Sokura L A 2015 Features of microstructure of InSb quantum dots on InAs substrate *J. Phys.:Conf. Ser.* **586** 012004
[10] Krier A, Huang X L and Hammiche A 2001 Liquid phase epitaxial growth and morphology of InSb quantum dots *J. Phys. D: Appl. Phys.* **34** 874–8

[11] Karim A, Gustafsson O, Hussain L, Wang Q, Noharet B, Hammar M, Anderson J and Song J 2012 Characterization of InSb QDs grown on InAs (100) substrate by MBE and MOVPE *Proc. SPIE* **8439** 84391J

[12] Matthews D R, Summers H D, Smowton P M and Hopkinson M 2002 Experimental investigation of the effect of the wetting-layer states on the gain-current characteristic of quantum-dot lasers *Appl. Phys. Lett.* **81** 4904–6

[13] Horikoshi Y, Kawashima M and Yamaguchi H 1986 Low-temperature growth of GaAs and AlAs-GaAs quantum well layers by modified molecular beam epitaxy *Japan. J. Appl. Phys.* **25** L868–70

[14] Horikoshi Y 1999 Advanced epitaxial growth techniques: atomic layer epitaxy and migration-enhanced epitaxy *J. Cryst. Growth* **201/202** 150–8

[15] Zhuang Q, Carrington P J and Krier A 2008 Growth optimization of self-organized InSb/InAs quantum dots *J. Phys. D: Appl. Phys.* **41** 232003

[16] Solov'ev V A, Lyublinskaya O G, Semenov A N, Mel'tser B Y, Solnyshkov D D, Terent'ev Y V, Prokopova L A, Toropov A A, Ivanov S V and Kop'ev P S 2005 Room-temperature 3.9–4.3 μm photoluminescence from InSb submonolayers grown by molecular beam epitaxy in an InAs matrix *Appl. Phys. Lett.* **86** 011109

[17] Terent'ev Y V, Toropov A A, Solov'ev V A, Mel'tser B Y, Moiseeva M M, Ivanov S V, Magnusson B, Monemar B and Kop'ev P S 2000 Photoluminescence and atomic force microscopy studies of InAs/InSb nanostructures grown by MBE *Proc. 25th ICPS* pp 401–2

[18] Lyublinskaya O G, Solov'ev V A, Semenov A N, Mel'tser B Y, Terent'ev Y V, Prokopova L A, Toropov A A, Sitnikova A A, Rykhova O V and Ivanov S V 2006 Temperature-dependent photoluminescence from type-II InSb/InAs quantum dots *J. Appl. Phys.* **99** 093517

[19] Mikhrin S S *et al* 2000 0.94 μm diode lasers base on Stranski–Krastanow and sub-monolayer quantum dots *Semicond. Sci. Technol.* **15** 1061–4

[20] Kim Y, Kim J O and Lee S J 2018 Submonolayer quantum dots for optoelectronic devices *J. Korean Phys. Soc.* **73** 833–40

[21] Solov'ev V A, Sedova I V, Lyublinskaya O G, Semenov A N, Mel'tser B Y, Sorokin S V, Terent'ev Y V and Ivanov S V 2005 Midinfrared injection-pumped laser based on a III–V/II–VI hybrid heterostructure with submonolayer InSb insets *Tech. Phys. Lett.* **31** 235–7

[22] Ivanov S V *et al* 2005 Molecular beam epitaxy of type II InSb/InAs nanostructures with InSb sub-monolayers *J. Cryst. Growth.* **278** 72–7

[23] Carrington P J, Solov'ev V A, Zhuang Q, Ivanov S V and Krier A 2008 Type II InSb/InAs quantum dot structures grown by molecular beam epitaxy using Sb_2 and As_2 fluxes *Proc. SPIE* **6900** 6900I

[24] Semenov A, Lyublinskaya O G, Solov'ev V A, Mel'tser B Y and Ivanov S V 2007 Surface segregation of Sb atoms during molecular-beam epitaxy of InSb quantum dots in an In(As)Sb matrix *J. Cryst. Growth.* **301–302** 58–61

[25] Ngo C Y, Yoon S F, Fan W J and Chua S J 2006 Effects of size and shape on electronic states of quantum dots *Phys. Rev.* B **74** 245331

[26] Wang T, Vaxenburg R, Liu W, Rupich S M, Lifshitz E, Efros A L, Talapin D V and Sibener S J 2015 Size-dependent energy levels of InSb quantum dots measured by scanning tunneling sepectroscopy *ACS Nano* **9** 725–32

[27] Pennycook S J, Rafferty B and Nellist P D 2000 Z-contrast imaging in an aberration-corrected scanning transmission electron microscope *Microsc. Microanal.* **6** 343–52

[28] Molina S I, Beltrán A M, Ben T, Galindo P L, Guerrero E, Taboada A G, Ripalda J M and Chisholm M F 2009 High resolution electron microscopy of GaAs capped GaSb nanostructures *Appl. Phys. Lett.* **94** 043114

[29] Molina S I, Sánchez A M, Beltrán A M, Sales D L and Ben T 2007 Incorporation of Sb in InAs/GaAs quantum dots *Appl. Phys. Lett.* **91** 263105

[30] Hernández-Maldonado D *et al* 2011 Compositional analysis with atomic column spatial resolution by 5th-order aberration-corrected scanning transmission electron microscopy *Microsc. Microanal.* **17** 578–81

[31] Malis T, Cheng S C and Egerton R F 1988 EELS log-ratio technique for specimen-thickness measurement in the TEM *J. Electron. Microsc. Tech.* **8** 193–200

[32] Khan A A, Herrera M, Pizarro J, Galindo P L, Carrington P J, Fujita H, Krier A and Molina S I 2019 Modified qHAADF method for atomic column-by-column compositional quantification of semiconductor heterostructures *J. Mater. Sci.* **54** 3230–41

[33] Pizarro J, Galindo P L, Guerrero E, Yañez A, Guerrero M P, Rosenauer A, Sales D L and Molina S I 2008 Simulation of high angle anular dark field scanning transmission electron microscopy images of large nanostructures *Appl. Phys. Lett.* **93** 153107

[34] Molina S I, Guerrero M P, Galindo P L, Sales D L, Varela M and Pennycook S J 2011 Calculation of integrated intensities of in aberration-corrected *Z*-contrast images *J. Electron. Microsc.* **60** 29–33

[35] Amelinckx S 1972 The geometry and interfaces due to ordering and their observation in transmission electron microscopy and electron diffraction *Surf. Sci.* **31** 296–354

[36] Sanchez A M, Beltran A M, Beanland R, Ben T, Gass M H, Peña F, Walls M, Taboada A G, Ripalda J M and Molina S I 2010 Blocking of indium incorporation by antimony in III–V-Sb nanostructures *Nanotechnology* **21** 145606

[37] Lu J, Luna E, Aoki T, Steenbergen E H, Zhang Y H and Smith D J 2016 Evaluation of antimony segregation in $InAs/InAs_{1-x}Sbx$ type-II superlattices grown by molecular beam epitaxy *J. Appl. Phys.* **119** 095702

[38] Beanland R 2005 Dark field transmission electron microscope images of III–V quantum dot structures *Ultramic* **102** 115–25

[39] Wei S H and Zunger A 1995 InAsSb/InAs: a type-I or a type-II band alignment *Phys. Rev.* B **52** 12039–44

[40] Jang Y D, Badcock T J, Mowbray D J, Skolnick M S, Park J, Lee D, Liu H Y, Steer M J and Hopkinson M 2008 Carrier lifetimes in type-II InAs quantum dots capped with a GaAsSb strain reducing layer *Appl. Phys. Lett.* **92** 251905

[41] Cirlin G, Petrov V and Dubrovskii V 1997 Direct formation of InGaAs/GaAs quantum dots during submonolayer epitaxies from molecular beams *Czech. J. Phys.* **47** 379–84

[42] Ivanov S V, Semenov A N, Lyublinskaya O G, Mel'tser B Y, Solov'ev V A, Terent'ev Y V, Sitnikova A A and Kop'ev P S 2005 InSb/InAs type II quantum dot structures for mid-IR laser applications *Proc. 12th Intl. Conf. on Narr. Gap Semicond.* vol 187, pp 83–91

[43] Luna E, Satpati B, Rodriguez J B, Baranov A N, Tournié E and Trampert A 2010 Interfacial intermixing in InAs/GaSb short-period-superlattices grown by molecular beam epitaxy *Appl. Phys. Lett.* **96** 021904

[44] Yurasov D V, Drozdov M N, Murel A V, Shaleev M V, Zakharov N D and Novikov A V 2011 Usage of antimony segregation for selective doping of Si in molecular beam epitaxy *J. Appl. Phys.* **109** 113533

[45] Antonov A V, Drozdov M N, Novikov A V and Yurasov D V 2015 Segregation of Sb in Ge epitaxial layers and its usage for the selective doping of Ge-based structures *Semicond.* **49** 1405–9

[46] Jones L 2016 Quantitative ADF STEM: acquisition, analysis and interpretation *IOP Conf. Ser.: Mater. Sci. Eng.* **109** 012008

[47] Molina S I, Sales D L, Galindo P L, Fuster D, González Y, Alén B, González L, Varela M and Pennycook S J 2009 Column-by-column compositional mapping by *Z*-contrast imaging *Ultramic* **109** 172–6
[48] Reyes D F, González D, Ulloa J M, Sales D L, Dominguez L, Mayoral A and Hierro A 2012 Impact of N on the atomic-scale Sb distribution in quaternary GaAsSbN-capped InAs quantum dots *Nano Res. Lett.* **7** 653
[49] Broek W V D, Rosenauer A, Goris B, Martinez G T, Bals S, Aert S V and Dyck D V 2012 Correction of nonlinear thickness effects in HAADF STEM electron tomography *Ultramic* **116** 8–12
[50] Rosenauer A, Gries K, Müller K, Pretorius A, Schowalter M, Avramescu A, Engl K and Lutgen S 2009 *Ultramic* **109** 1171–82
[51] Hÿtch M J, Snoeck E and Kilaas R 1998 Quantitative measurement of displacement and strain field from HREM micrographs *Ultramic* **74** 131–46
[52] Muraki K, Fukatsu S, Shiraki Y and Ito R 1992 Surface segregation of In atoms during molecular beam epitaxy and its influence on the energy levels in InGaAs/GaAs quantum wells *Appl. Phys. Lett.* **61** 557–9
[53] Steinshnider J, Harper J, Weimer M, Lin C H, Pei S S and Chow D H 2000 Origin of antimony segregation in GaInSb/InAs strained-layer superlattices *Phys. Rev. Lett.* **85** 4562–5
[54] Pelá R R, Teles L K, Marques M and Martini S 2013 Theoretical study of the indium incorporation into III–V compounds revisited: the role of indium segregation and desorption *J. Appl. Phys.* **113** 033515
[55] Martini S, Quivy A A, Lamas T E, Da Silva M J, Da Silva E C F and Leite J R 2003 Influence of indium segregation on the RHEED oscillations during the growth of InGaAs layers on a GaAs (001) surface *J. Cryst. Growth.* **251** 101–5
[56] Kaspi R 1999 Compositional abruptness at the InAs-on-GaSb interface: optimizing growth by using the Sb desorption signature *J. Cryst. Growth.* **201–202** 864–7
[57] Kaspi R and Evans K R 1997 Sb-surface segregation and the control of compositional abruptness at the GaAsSb/GaAs interface *J. Cryst. Growth.* **175–176** 838–43
[58] McLean D 1957 *Grain Boundaries in Metals* (Oxford: Oxford University Press)
[59] Moison J M, Guille C, Houzay F, Barthey F and Rompay M V 1989 Surface segregation of third-column atoms in group III–V arsenide compounds: ternary alloys and heterostructures *Phys. Rev.* B **40** 6149–62
[60] Karpov S Y and Makarov Y N 2000 A quantitative model of surface segregation in III–V ternary compounds *Mater. Res. Soc. Symp. Proc.* **618** 185–91
[61] Dehaese O, Wallart X and Mollot F 1995 Kinetic model of element III segregation during molecular beam epitaxy of III-III'-V semiconductor compounds *Appl. Phys. Lett.* **66** 52–4
[62] Millunchick J M, Anderson E M, Pearson C, Sarney W L and Svensson S P 2013 Incorporation kinetics in mixed anion compound semiconductor alloys *J. Appl. Phys.* **114** 234907
[63] Fukatsu S, Fujita K, Yaguchi H, Shiraki Y and Ito R 1991 Self-limitation in the surface segregation of Ge atoms during Si molecular beam epitaxal growth *Appl. Phys. Lett.* **59** 2103–5
[64] Godbey D J and Ancona M G 1997 Modeling of Ge segregation in the limits of zero and infinite surface diffusion *J. Vac. Sci. Technol.* A **15** 976–80
[65] Magri R and Zunger A 2002 Effects of interfacial atomic segregation and intermixing on the electronic properties of InAs/GaSb superlattices *Phys. Rev.* B **65** 165302
[66] Haxha V, Drouzas I, Ulloa J M, Bozkurt M, Koenraad P M, Mowbray D J, Liu H Y, Steer M J, Hopkinson M and Migliorato M A 2009 Role of segregation in InAs/GaAs quantum dot structures capped with a GaAsSb strain-reduction layer *Phys. Rev.* B **80** 165334
[67] Reyes D F, Braza V, Gonzalo A, Utrilla A D, Ulloa J M, Ben T and González D 2018 Modelling of the Sb and N distribution in type II GaAsSb/GaAsN superlattices for solar cell applications *Appl. Surf. Sci.* **442** 664–72
[68] Anderson E M and Millunchick J M 2018 The atomistic mechanism for Sb segregation and As displacement of Sb in InSb(001) surfaces *Surf. Sci.* **667** 45–53
[69] Hatami F, Kim S M, Yuen H B and Harris J S 2006 InSb and InSb:N multiple quantum dots *Appl. Phys. Lett.* **89** 133115
[70] Tasco V, Deguffroy N, Baranov A N, Tournié E, Satpati B, Trampert A, Dunaevskii M S and Titkov A 2006 High-density, uniform InSb/GaSb quantum dots emitting in the midinfrared region *Appl. Phys. Lett.* **89** 263118
[71] Semenov A N, Lyublinskaya O G, Solov'ev V A, Mel'tser B Y and Ivanov S V 2008 *In situ* study of the formation of the kinetics of InSb quantum dots grown in an InAs(Sb) matrix *Semicond.* **42** 74–9
[72] Abramkin D S, Barakov A K, Putyato M A, Emelyanov E A, Kolotovkina D A, Gutakovskii A K and Shamirzaev T S 2017 Fomation of low-dimensional structures in the InSb/AlAs heterosystem *Semicond.* **51** 1233–9
[73] Timm R, Lenz A, Eisele H, Ivanova L, Dähne M, Balakrishnan G, Huffaker D L, Farrer I and Ritchie D A 2008 Quantum ring formation and antimony segregation in GaSb/GaAs nanostructures *J. Vac. Sci. Technol.* B **26** 1492–503
[74] Magri R and Zunger A 2002 Segregation effects on the optical properties of (InAs)/(GaSb) superlattices *Phys.* E **13** 325–8
[75] Hodgson P D, Bentley M, Delli E, Beanland R, Wagener M C, Botha J R and Carrington P J 2018 Optical and structural properties of InGaSb/GaAs quantum dots grown by molecular beam epitaxy *Semicond. Sci. Technol.* **33** 125021

Publication III

Effect of cap layer growth temperature on the Sb distribution in InAs/InSb/InAs sub-monolayer heterostructures for mid-infrared devices

Atif A. Khan, E. Repiso, M. Herrera, P. J. Carrington, M. de la Mata, J. Pizarro, A. Krier, S. I. Molina

Accepted in Nanotechnology 31: 105702 (2020)

Effect of the cap layer growth temperature on the Sb distribution in InAs/InSb/InAs sub-monolayer heterostructures for mid-infrared devices

Atif A Khan[1], E Repiso[2], M Herrera[1], P J Carrington[3], M de la Mata[1], J Pizarro[4], A Krier[2], S I Molina[1]

[1] Department of Material Science, Metallurgical Chemistry and Inorganic Chemistry, IMEYMAT, University of Cádiz, 11510 Puerto Real, Spain.

[2] Physics Department, Lancaster University, Lancaster, LA1 4YB, UK

[3] Engineering Department, Lancaster University, Lancaster, LA1 4YW, UK

[4] Department of Computer Engineering, ESI, University of Cádiz, 11510 Puerto Real, Spain.

Abstract

Sub-monolayer (SML) deposition of InSb within InAs matrix by migration enhanced epitaxy (MEE) tends to form type II SML nanostructures offering efficient light emission within the mid-infrared (MIR) range between 3-5 µm. In this work, we report on the Sb distribution in InSb/InAs SML nanostructures with InAs cap layers grown at temperatures lower than that associated with the under-grown InSb active layer. Analysis by transmission electron microscopy (TEM) in 002 dark field (DF) conditions shows that the reduction in the growth temperature of the InAs cap layer increases the amount of Sb deposited in the layers, in good agreement with the X-ray diffraction (XRD) results. TEM micrographs also show that the layers are formed by random InSbAs agglomerates, where the lower cap temperature leads to a more continuous InSb layer. Quantitative atomic column resolved high angle annular dark field (HAADF)-scanning (S)TEM analyses also reveal atomic columns with larger composition of Sb for the structure with the lowest InAs cap layer temperature. The dependence of the Sb distribution on InAs cap growth temperature allows tuning the corresponding emission wavelength in the MIR range, as shown by the photoluminescence (PL) emission spectra.

Keywords: InSb/InAs sub-monolayer nanostructures, 002 Dark Field analysis, Atomic column HAADF-(S)TEM, Sb segregation, Composition analysis

Introduction

Previous reports on the epitaxial growth of sub-monolayer (SML) quantum dots (QDs) indicate increased dot density, quantum confinement and size uniformity with smaller base diameter [1,2] than its Stranski-Krastanow (SK) [3] counterpart which is the typical III-V epitaxial QD formation method [4]. III-V SML QDs are formed due to SML, i.e., ~ 1 ML epitaxial deposition of a III-V binary in solo or in stacks into another type of III-V barrier material(s) [5-12]. The deposition of these SML insertions into the barrier layers is often carried out using the migration enhanced epitaxy (MEE) technique [7, 13, 14], where the atomic species of the III-V sub-lattices are alternatively supplied to the surface instead of the simultaneous deposition of the conventional epitaxy (CE) growth mode. It is claimed that such deposition technique could avoid the formation of the wetting layer (WL) intrinsic to the SK growth mode. In this case, no carrier scattering would occur between the WL and the QDs leading to the enhancement of the

associated modulation bandwidth (BW) and maximum gain [12]. SML QDs have been used to design various kinds of optoelectronic devices, such as- lasers [15, 16], virtual-cavity surface-emitting lasers (VCSELs) [17], photo-detectors (PDs) [18], solar cells (SCs) [19], etc.

In particular, SML heterostructures based on InSb/InAs are an attractive option for achieving efficient mid-infrared (MIR) emission in the 2 or 3-5 μm spectral region used for light emitting diodes (LEDs) [6, 20] and lasers [5, 7]. The type II broken gap band alignment leads to strong hole localization within the InSb SML whilst electrons are loosely confined within the InAs matrix. This leads to a reduction in non-radiative Auger recombination leading to an increase in the radiative efficiency. Therefore, InSb/InAs SML insertions have been reported to exhibit intense MIR photoluminescence (PL) up to room temperature [6]. The emission wavelength of these heterostructures can be tuned by modifying the nominal thickness of the InSb insertions, through the control of the growth temperature [5]. In this sense, growth temperatures of the InSb insertions in the range 400ºC-485ºC have been found to provide emission in the MIR regime [5].

However, recently we have demonstrated by TEM techniques that the growth of InSb/InAs SML heterostructures by MEE at 430ºC forms an inhomogeneous InSbAs layer with a thickness of ~ 3 nm that contains InSbAs agglomerates with low Sb composition (~5-10%) [21]. The formation of this relatively thick layer is somewhat compatible with the strong tendency of Sb to segregate upwards during growth [22], supported by the corresponding large segregation coefficient measured from the composition profile. In GaSb/GaAs quantum rings, the strong Sb segregation observed has been related to an extensive group-V atomic exchange, in this case As/Sb exchange, during the growth of the capping layer on the nanostructures [23]. These group V exchange reactions can even modify significantly the morphology of InGaSb/GaAs QDs grown by MEE [24]. In this instance, it has been found that reducing the growth temperature of the GaAs cap (known as cold capping technique) helps to preserve the QD morphology during MEE growth [24]. For conventional InSb/InAs SK QDs grown by MEE, Zhuang *et. al.* [25] reported that a reduction of the InAs barrier layer growth temperature (regarding the InSb temperature) dramatically improved the emission efficiency, associated with a reduction in the As/Sb exchange. Inspired by this outcome, in this work we investigate the formation of InSb/InAs SML QDs heterostructures with InAs cap layers grown at temperatures lower than that used to obtain the InSb SML insertions (380ºC and 310ºC for the InAs capping layers, 430ºC for the InSb). The effect of the cap temperature on the Sb distribution and on the PL emission is discussed.

Materials and methods

Two InSb/InAs heterostructures have been grown by MEE on n-InAs substrates with different InAs cap temperatures. Each sample has three InSb layers. Initially, a 500 nm InAs buffer layer is grown on the InAs substrate at 470ºC. Then, 20 nm of InAs is deposited at a growth temperature of 430ºC. For the deposition of each InSb layer, the InAs surface is exposed to an Sb_2 flux for 20s, then pure In for 5s and again Sb_2 for 6s while maintaining a growth temperature of 430ºC. Afterwards, the growth is interrupted and the temperature lowered to the desired cap temperature under a Sb_2 flux. The InSb SMLs are capped with 13 nm of InAs, at temperatures of 380ºC and 310ºC for the two samples considered. Due to the lower growth temperature for the InAs cap, they are called cold caps (CCs). The temperature is then increased to 470ºC to grow a 33 nm InAs layer, followed by another 20 nm of InAs layer grown at 430ºC, and then the next InSb layer is grown with a similar procedure. This implies that the active layer

periodicity of the CC samples is ~ 66 nm. Finally, an InAs layer of 100 nm is grown at 470ºC. An additional sample where the InAs cap layer is grown at the same growth temperature of the InAs layers (which is the conventional procedure) although containing 10 InSb layers instead of 3 with active layer periodicity of ~ 20 nm is also considered for comparison. The growth of the layers was monitored using *in situ* reflection high energy electron diffraction (RHEED) and the corresponding growth temperature T_s was measured by calibrated thermocouple.

Low temperature (4K) photoluminescence (PL) has been performed on the samples using a single mode laser diode with an emission wavelength of 785 nm and a $1mm^2$ spot size that leads to a power density of $20W/cm^2$. For XRD analyses, ω-2θ symmetric scans were performed using a Bede QC200 double crystal machine. The nominal thickness of the InSb layer and corresponding structural period was obtained from the XRD simulation using RADS Mercury software.

A combination of mechanical thinning and precision ion polishing system (PIPS) associated Ar^+ ion milling was used to prepare the electron transparent specimens for the TEM analyses. The diffraction contrast analysis was carried out using a JEOL JEM 2100 microscope at an operating voltage of 200 kV. A double aberration corrected FEI Titan Cubed Themis microscope was used for atomic column resolved high angle annular dark field (HAADF)-scanning TEM ((S)TEM) analysis of the specimens at 200 kV. The imaging parameters used to acquire corresponding HAADF-(S)TEM images are: C_s = 1 µm, C_5 = 5 mm, HAADF detector inner angle = 63.8 mrad, convergence angle = 16.04 mrad and camera length = 91 mm. The HAADF-(S)TEM images were taken from regions of the specimens that possess an average relative log-ratio value of t/λ ~ 0.41 and 0.47 for specimens with 380ºC and 310ºC CCs, respectively, measured using zero-loss peak electron energy loss spectroscopy (EELS). Here, 't' represents the thickness of a region, while 'λ' denotes the corresponding electron mean free path (MFP). The MFP with the value of ~ 62.14 nm was found in both cases, calculated using the method by Malis *et. al.* [26].

Results and discussion

Figure 1 shows the low temperature (4K) normalized PL profiles in red and green associated with the samples of InAs CC grown at 380ºC and 310ºC, respectively. The PL profile of the structure with the InAs cap grown at 430ºC has also been included for comparison (in black). As it can be observed, the InAs peak is located at a wavelength of ~ 3 µm in all samples, similar to the InAs induced PL responses observed in refs. [5-7, 25]. There is a small shifting between the InAs peaks from 380ºC and 310ºC/430ºC samples. The InAs PL emission originates from near band edge states including shallow donors and acceptors. The origin of the small shift observed could be related to the 380ºC sample containing more of these impurities or being of lower crystalline perfection (since linewidth is also a bit larger). Lower PL powers have been also used to look for excitons but none could be identified. On the other hand, it can be observed that although the InAs intensity is reduced in the 430ºC sample, the linewidth of the InAs related PL remains narrow, which indicates good crystalline quality. This lower intensity from the InAs most probably originates from non-radiative (surface) recombination in the upper 100nm InAs upper layer or the InAs buffer. To clarify how much the emission levels of InSb and InAs vary in a sample, we have included the corresponding non-normalized PL spectra of each sample as an inset in the normalized PL spectra in Figure 1. However, we must note that it is unreliable to compare absolute PL intensities due to alignment factors, etc. The non-normalized PL intensity of the InSb grown at 430ºC is the highest consistent with good crystalline quality in these nanostructures. It should also be noted that the PL

intensity dips at ~ 4.2 μm in all samples are due to the presence of CO_2 absorption from the atmosphere during PL measurements [6]. In addition, the feature around 2.75 μm in the PL spectrum is due to an instrumental artifact arising from imperfect cancellation of the background in the Fourier-transform infrared (FTIR) spectrometer. This happens at this wavelength due to the atmospheric water vapor absorption near 2.7 μm.

Regarding the normalized InSb signal, it can be seen that the sample with CC grown at the conventional growth temperature of 430ºC (black line) exhibits one PL peak, at a wavelength of ~ 4 μm. When the InAs CC growth temperature is reduced to 380º C (red line), the PL emission changes, and two InSb peaks at 3.7 μm and 4.6 μm, respectively, are found. The reasons behind the differences observed in the PL spectra are likely related to a difference in the Sb distribution in the material. The two InSb peaks at different wavelengths observed in the sample with 380ºC InAs CC could be due to the formation of two distinct quantum structures within the InSb layer regions. Semenov *et al.* [27] demonstrated two InSb PL peaks originated by high excitation power density at 110K in InSb/InAs SML nanostructures, claiming that these peaks appear due to the presence of both InSb QDs and a InAsSb WL in the material. In our case, the peaks observed could be related to regions of the InSb layer with different morphology and/or Sb content. In comparison to the sample with InAs cap grown at 430ºC, the PL peaks observed appear one at longer wavelength and one at a shorter wavelength than the ~ 4 μm peak of the sample 430ºC. This suggests that upon reducing the InAs CC growth temperature, some regions of the InSb layer become richer in Sb, leaving other regions with less Sb content. This could point to the formation of initial Sb clusters or QDs with a density significant enough to produce a remarkable variation in the PL emission. When further reducing the InAs CC growth temperature to 310ºC, Fig. 1 shows that only one PL peak at the longer wavelength of 4.6 μm is observed. It is well known that the incorporation of Sb in III-V semiconductors reduces the corresponding bandgap energy and hence, induces a red shift in wavelength [28, 29], where a higher Sb composition imposes a larger red shift [6]. This suggests the existence of one type of quantum structure with a larger Sb content in this heterostructure. In order to investigate the aforementioned assumptions, post-growth X-ray diffraction (XRD) measurements and 002 dark field (DF) TEM analyses of these samples have been performed.

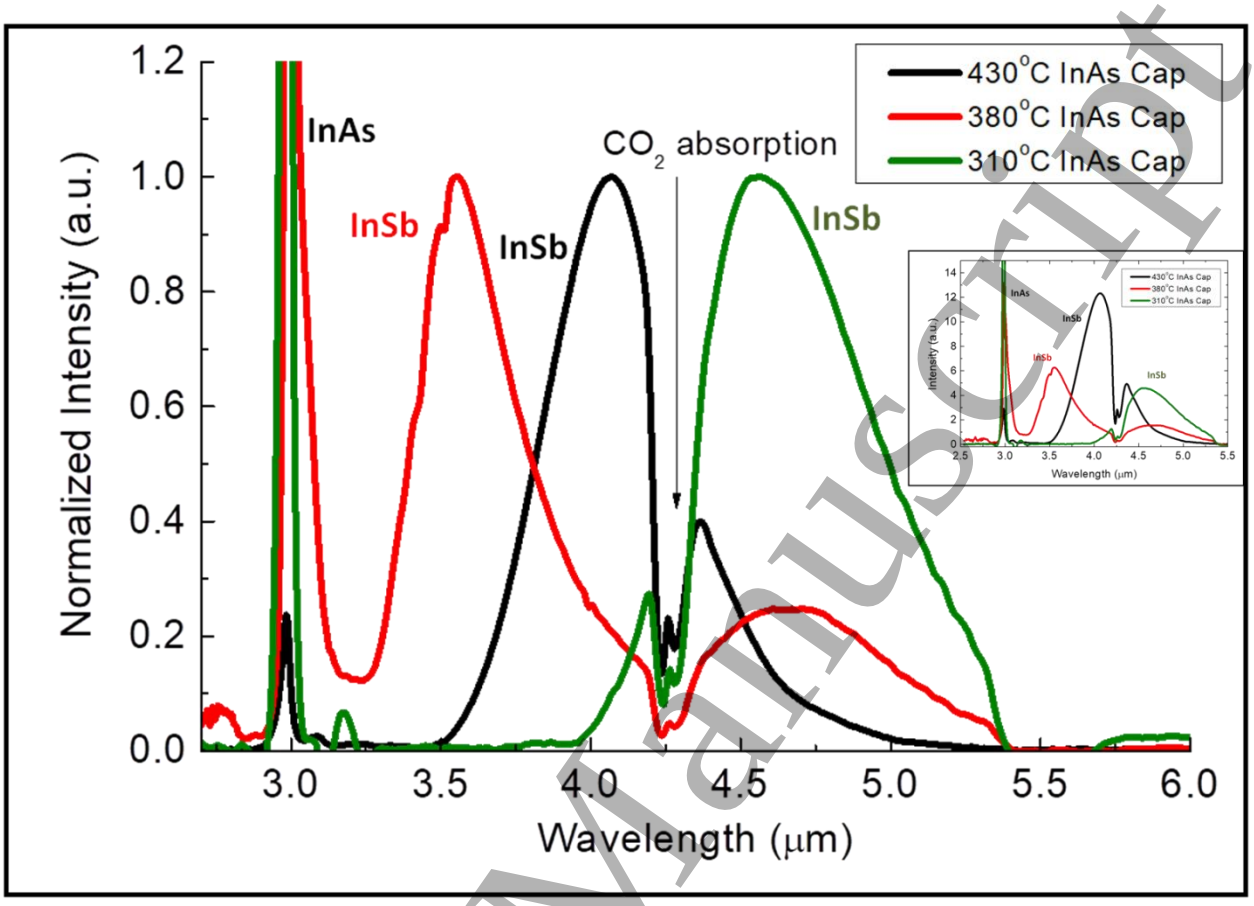

Figure 1: Normalized PL response (4K) associated with 430ºC, 380ºC and 310ºC InAs cap samples in black, red and green, respectively. The inset represents the non-normalized version of the PL spectra.

Figure 2a shows the post-growth XRD profiles obtained from the samples with InAs CCs grown at 380ºC (black line) and at 310ºC (red line), respectively. The XRD profile of the structure with the InAs cap layer grown at 430ºC has also been included for comparison (blue line). In each profile, the highest peak represents the Bragg diffraction from the InAs substrate and the satellite peaks specify the corresponding Bragg diffractions associated with the overgrown InSb layers. It should be noted that the active layer periodicity of the reference sample is different from the CC samples, as mentioned before. In the insets, sample-specific individual experimental XRD spectra together with the corresponding simulated XRD curves are included. It should be highlighted that some disagreements regarding the active layer periodicity between the XRD simulations and the experimental growth structure is observed. This disagreement could be due to the limited modeling capability of XRD, which does not take into account the sticking coefficients of In and As_2, possible Sb segregation, group V atomic exchange, graded InSbAs barriers, change in growth rate over the associated temperature range, etc. It is not easy to determine the exact reason from the discrepancy as there may be a wide variety of parameters involved. As it can be observed in Figure 2a, the satellite peaks corresponding to the 430ºC InAs cap sample (in blue) appear at a larger distance from one another compared to the satellite peaks obtained from 380ºC (in black) and 310ºC (in red) InAs CC samples. These last two samples have only a slight shift between some satellite peaks, where one of these shifts is indicated by a blue arrow in Figure 2a. However, it must be noted that in thicker layers, thickness variations between layers provide smaller differences in the XRD profiles that

in thin layers. Assuming flat layers of pure InSb composition, a higher separation between two consecutive satellite peaks (in Figure 2a), induced by active region periodicity denotes a lower overgrown InSb layer thickness and vice versa (a nice review on XRD can be found in ref. [30]). Therefore, the observed XRD profiles indicate that the growth temperature of the InAs caps in these structures may affect the thickness and/or the morphology of the InSb layers. With the abovementioned assumptions, thicknesses of 0.65 ML, 0.86 ML and 1.02 ML have been calculated for InAs cap growth temperatures of 430ºC, 380ºC and 310ºC, respectively. This suggests an increase in the incorporation of Sb for reduced InAs CCs growth temperatures. The XRD results are consistent with the PL results which showed a larger emission wavelength associated with a larger Sb composition in the 310ºC sample. However, it should be noted that different Sb distributions could also account for the XRD results obtained, as 3D In(As)Sb complex nanostructures are likely to have formed during the growth. In order to obtain direct compositional information on the Sb distribution in the material, the samples have been analyzed using TEM techniques.

Figures 2c and 2d show diffraction contrast images of the samples with InAs CCs grown at 380ºC and 310ºC, respectively, obtained in 002 DF conditions. For comparison, Figure 2b includes an image of the sample with the InAs cap grown at 430ºC, where the conventional approach of growing both InSb and InAs cap layers at the same temperature was followed. All 002 DF images in Figure 2b-2d are shown in temperature color grade to induce better graphical representations as per chemical contrast based intensity variations in arbitrary units (a.u.). In each image there is a central low intensity area in green/blue that corresponds to the InSb region, sandwiched between high intensity InAs cap and barrier layers. It should be noted that some intensity variability is observed in the homogeneous InAs barrier layers, due to small specimen thickness fluctuations related to the TEM specimen thinning process to electron-transparency. A comparison of Figures 2b, 2c and 2d reveals that the Sb containing layer is thicker and has smaller intensity for reduced InAs CC growth temperature. This is consistent with a larger incorporation of Sb in the material for reduced temperatures (380ºC and 310ºC), supporting the XRD results obtained above. In InAs/InAsSb type-II superlattices (SLs) grown on GaSb by MBE, an increase in the Sb incorporation in the InAsSb layers has been reported when the SL growth temperature is reduced [22, 31]. The authors attribute their finding to the preferential incorporation of Sb in InAsSb at lower temperature. Our results suggest that not only the growth conditions of the Sb-containing layer have a strong impact on Sb incorporation, but also the parameters used for capping such active layers.

A detailed observation of the 002 DF images obtained shows that the InSb distribution in the layers is not regular, forming random nucleated regions (in blue) along the layers. These Sb agglomerations do not show shapes that could be clearly identified as any common QD shape reported in the literature (cuboid, cylindrical, pyramidal, etc. [32]). Some agglomerates with height clearly larger than the layer beside them can be observed in the sample with the InAs cap grown at 430ºC, as shown by the white arrows in Figure 2b. This holds true for the structure with InAs CC grown at 380ºC, where a clear agglomeration is marked by the white arrow in Figure 2c, although in this case it seems to be embedded into the InSbAs layer. However, in the InSb/InAs heterostructure with InAs CC grown at 310ºC in Figure 2d, there seems to be a thicker and more continuous layer, rather than isolated agglomerates. In this sense, the red-shift observed in the PL emission of these samples when the InAs CC growth temperature is reduced can be justified by the increase in the Sb content derived from the 002 DF images. The PL spectra for the sample with InAs CC at 380ºC show two peaks at different wavelengths. This means that two different quantum structures with statistical significance should be present in the material, although these quantum structures

are not obvious from the corresponding TEM image in Figure 2c. TEM analyses allow studying small regions of the material of interest, normally of several tens of nm. On the other hand, PL analysis provides information related to comparatively larger regions, up to several hundreds of nm. Because of this, sometimes a direct correlation between the results obtained by these techniques is difficult to carry out. On the other hand, the single peak observed at longer wavelength in the sample with InAs CC at 310ºC could be associated with the Sb-rich continuous layer observed (or bigger Sb agglomerates). The single PL peak observed for the sample with the InAs cap obtained at 430ºC could be related to the small agglomerations found in 002 DF. In order to obtain further information on the Sb distribution in the materials with higher spatial resolution and to quantify the Sb content in the layers, the samples were analyzed by aberration corrected atomic column HAADF-(S)TEM.

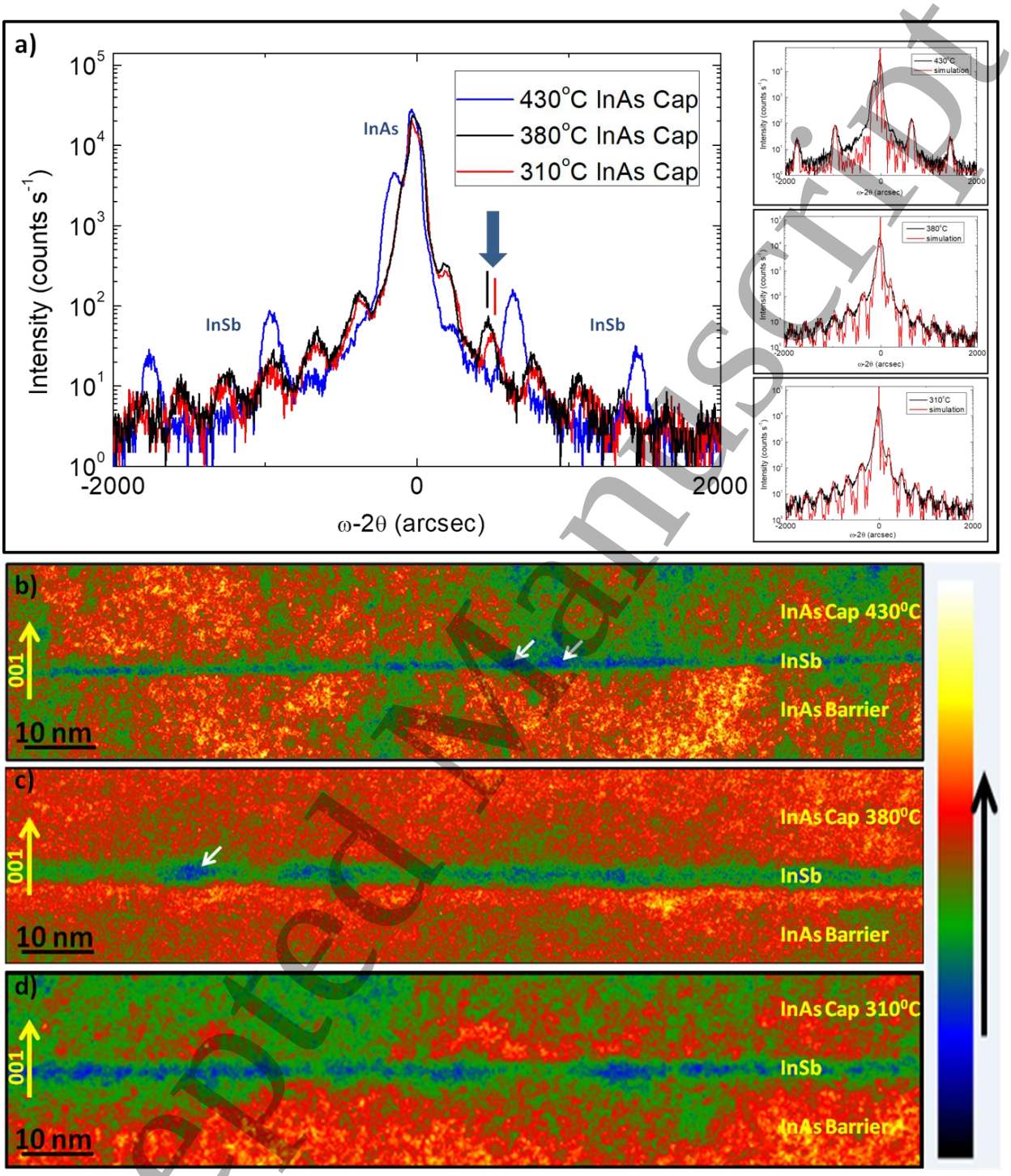

Figure 2: (a) XRD spectra from the three InSb/InAs samples which contain InAs caps grown at 430ºC, 380ºC and 310ºC, denoted by blue, black and red lines, respectively. The insets represent sample-specific individual experimental XRD spectra from Figure 2a and their corresponding simulated XRD curves. Temperature graded 002 DF TEM images of single InAs/InSb/InAs layers taken from samples with InAs cap growth temperatures of (b) 430ºC, (c) 380ºC and (d) 310ºC, illustrating intensity variations within the heterostructures. The color scale demonstrates increase in intensity from black to white (in a.u).

Figures 3a and 3b exhibit HAADF-(S)TEM images showing a single InAs/InSb/InAs layer of the samples with 380ºC and 310ºC InAs CC, respectively. In these images, microscope induced vacuum signal has been subtracted using the approach illustrated in ref. [33], as it is a requirement for precise quantitative HAADF-(S)TEM analysis.In both samples a layer where the HAADF-(S)TEM intensity is larger than the region above and below it can be observed at the center of the image. As in HAADF-(S)TEM images the intensity is roughly proportional to the square of the average atomic number in the material ($Z^{\sim 1.7\text{-}2}$), the observed layers can be associated with the Sb-containing layers. These high intensity dumbbells appear to be forming single thin layers in each image, along with few agglomerates. In order to obtain a clearer picture of the Sb distribution in each heterostructure, we have quantified the Sb composition with atomic column resolution. For this, initially we used the quantitative HAADF (qHAADF) tool, developed by Molina *et. al.* [34]. This tool compares atomic column-by-column intensities from a region of interest (ROI) with the average atomic column intensity from a homogeneous material region (reference) in a single HAADF-(S)TEM image and reveals atomic column-by-column normalized integrated intensity, R' on the ROI. Afterwards, these R' values are converted to atomic column-by-column Sb composition (in %) using the method by Maldonado *et. al.* [35]. However, it should be mentioned that the HAADF-(S)TEM intensity is not only related to the average Z number in the material, as the thickness of the specimen (thin foils) used for the analysis also have an important effect. As shown in ref [36], a precise estimation of the composition from HAADF-(S)TEM images using the method explained above requires that both ROI and reference regions have the same thickness. Because of that, simultaneous zero-loss peak EELS analysis was performed during the acquisition of each HAADF-(S)TEM image in order to measure specimen thickness. This analysis revealed an average thickness variation between ROI and reference regions in either image to be < 1 nm. Although this average thickness variation is quite low, its compensation allows more precise Sb induced R' values to be obtained. According to the simulated images induced R' vs ROI-reference specimen thickness variation profiles in ref. [36], we have introduced an additional parameter of $\pm\ 0.02*\Delta t$, where Δt represents specimen thickness variation between ROI and reference regions in nm, to the qHAADF formula in ref. [34] that allows calculating the corrected R' values. The composition values obtained with these corrected R' values using the approach by Maldonado *et. al.* [35] are illustrated in the insets of Figure 3a and 3b as color maps. In particular, those maps correspond to the Sb agglomerates within a yellow rectangle in the respective image (ROI areas) whereas the reference areas are located in the InAs barrier layers, marked with green rectangles. These Sb composition color maps demonstrate that Sb is distributed within few atomic columns in the agglomerates. No uniform and defined shape has been found among the different agglomerates analyzed. In order to evaluate possible differences in the Sb content in these structures with InAs CC grown at different temperatures, we performed a statistical analysis on the atomic column composition using several images from either sample and represented the corresponding data in a histogram illustrated in Figure 3c. In this Figure, the black and red bars correspond to the results obtained for the 380ºC and 310ºC CC samples, respectively. It should be noted that the region of the material analyzed when a sample is studied by atomic column (S)TEM techniques is very small, typically several tens of nms, so care should be taken in the quantitative interpretation of statistical data , because the data may vary slightly when moving to another region of the material. The sample with the 310ºC InAs CC has a larger number of atomic columns with Sb composition in the range 21-30% Sb, whereas the structure with the 380º InAs CC has them in the range 11-20 %. In a previous paper [21], we quantified by TEM techniques the Sb content in the structure with an InAs cap layer obtained at 430ºC, and found that the InSb layer had

Sb content of ≤ 10%. Thus, our results show a clear increase in the Sb content in the InSb layer for reduced InAs CC growth temperatures.

The analysis of the sample with the InAs cap layer grown at the same temperature of 430ºC as the undergrown InSb layer in the conventional manner published previously by the authors showed a strong Sb segregation during growth [21]. This segregation could be partly responsible for the differences in the Sb distribution in the samples with different InAs CC growth temperature observed in this work. In order to investigate the Sb segregation for the lower InAs CC growth temperature of 310ºC considered in this work, the ML-by-ML average Sb composition profile (in black) as per the composition map in Figure 3b is shown in Figure 3d., The maximum average Sb composition in a ML within the analyzing region has been found to be 24%, and the composition profile shows asymmetric edges along the growth direction: the interface between the InAs cap layer and the InSb layer is more graded than the interface between the InSb layer and the undergrown InAs barrier. This is the typical profile of an interface with upwards segregation during growth. In order to quantify the Sb segregation coefficient, the theoretical Muraki segregation model [37] has been considered. This model has been successfully implemented to analyze Sb segregation in InAs/$InAs_{1-x}Sb_x$ type-II superlattices [38], GaInSb/InAs strained-layer superlattices [39], etc. To perform Sb segregation analysis in terms of Sb composition in Figure 3d, the maximum Sb compositions must be positioned at ML1 and so on and so forth in either case as per model requirement. The formulation used for this quantification is as follows:

$$x = x_0 (1 - R^N) R^{z-N}, \text{ for } z \geq N$$

Here, x is the average ML-by-ML Sb composition, x_0 is the nominal InSb composition, z is the number of analyzing MLs at ML≥0, R is the segregation coefficient and N is the nominal thickness of the InSb layer.

The Muraki model fit obtained is demonstrated by a red profile (in %) in Figure 3. Local deviations of the composition values in the experimental profile regarding the theoretical model can be observed. These local fluctuations are unavoidable when composition values obtained with very high spatial resolution and from a very small region of the material are considered. In this case, due to the small size of the clusters, averaging the data over larger areas is not possible. Despite this, the authors believe the fitting of the experimental data to the theoretical model is reasonably good enough to obtain an estimation of the segregation coefficient in the material. The best Muraki fit has been obtained with an R of 0.61 for a nominal InSb deposition thickness of 1.09 ML which is in good agreement with the deposition thickness of 1.02 ML obtained in the XRD analysis. Semenov *et. at.* [27] estimated by RHEED the Sb segregation coefficient in InSb/InAs SML insertions for different InSb growth temperatures in the range 410ºC-500ºC, finding a linear reduction of this coefficient with temperature. If their data is extrapolated to the growth temperature of 310ºC, a value of R of 0.59 is obtained, which is in a good agreement with the value obtained in the present work. This segregation coefficient is smaller than the segregation coefficient of 0.81 obtained using the same procedure by the authors in the sample with InAs cap growth temperature of 430ºC in a previous paper [21], indicating that the reduction in the InAs CC growth temperature has a direct effect on the Sb segregation during growth.

The results obtained by XRD and (S)TEM in the present work have shown an increase in the Sb content in SML InSb/InAs heterostructures when the growth temperature of the InAs cap layer is reduced. In relation to this, in superlattices of Sb MLs in (InGaAl)As grown by MEE, an increase in the amount of Sb incorporated in the material when decreasing the superlattice growth temperature has been found by XRD

[40]. In particular, for Sb MLs in InAs, this has been found to occur in the temperature range 465-400ºC, and it is observed that the growth temperature should be less than 420 °C to achieve a complete ML of InSb per period. The authors claim that their results are consistent with Sb evaporation at higher temperatures, and relate their finding with the congruent sublimation temperature of the binaries (400 °C for InSb). Haugan *et. al.* [22] found that in InAs/InAsSb superlattices, the Sb content increased by 14% as the growth temperature decreased from 440 to 400 ºC, and attributed their finding to Sb surface segregation during InAsSb growth through the As-Sb exchange process. The effect of the InAs cap growth temperature on the Sb incorporation in InAs reported in the present work is in line with the effect of the InSb SL growth temperature, as the reduction of both seems to improve the Sb incorporation. Here, it has been possible to introduce a complete InSb ML in InAs at high growth temperatures (430ºC), by reducing the InAs CC temperature to 310ºC. Thus, our results highlight the importance of the cap layer growth conditions on the characteristics of the InSb layers obtained. The increase in the Sb content in the InSb layers analyzed could be due to two different phenomena. On the one side, our results have shown a clear decrease in the Sb segregation coefficient when reducing the CC growth temperature. In relation to this, the success of the MEE technique for the growth of InSb SML nanostructures is attributed to a very efficient Sb/As anion exchange reaction that occurs upon exposure of the InAs surface to the Sb flux [7], also observed in the GaSb/GaAs system [41]. However, the reverse group-V exchange reaction (As/Sb exchange), i.e., Sb segregation, also takes place upon capping of the Sb-containing layer [42-44]. The reduction in the CC growth temperature is likely to reduce in the As/Sb exchange between the corresponding InSb and InAs cap layer consequently reducing the segregation in the material. However, if segregation was the only phenomenon responsible for the Sb distribution observed, a thinner and Sb-rich layer would be expected in the sample with the InAs CC grown at the lowest temperature (310ºC). Instead, our 002 DF images show that the InSb layer in this structure is clearly thicker than those obtained with InAs caps grown at higher temperatures. Because of this, the authors think that Sb evaporation at higher temperatures should also be taking place, similarly to that proposed by Bennet *et. al* [40]. Thus, the decrease in the InAs CC growth temperature would produce a decrease in both the Sb segregation and the Sb evaporation during growth, leading from a layer with Sb-rich clusters to a more continuous InSb-rich layer. These changes in the InSb distribution in the material have shown to affect the PL emission of the material, exhibiting a clear red-shift due to the increase in the Sb content. A further reduction in the InAs CC growth temperature may help to increase the Sb incorporation in the layer, although care should be taken to maintain a high quality of the epitaxial growth to avoid possible structural imperfections observed at low growth temperatures [45]. Although the present work constitutes a step forward in the understanding of the growth process of SML InSb QDs, further work is needed to fully control the structural and functional properties of these promising nanostructures.

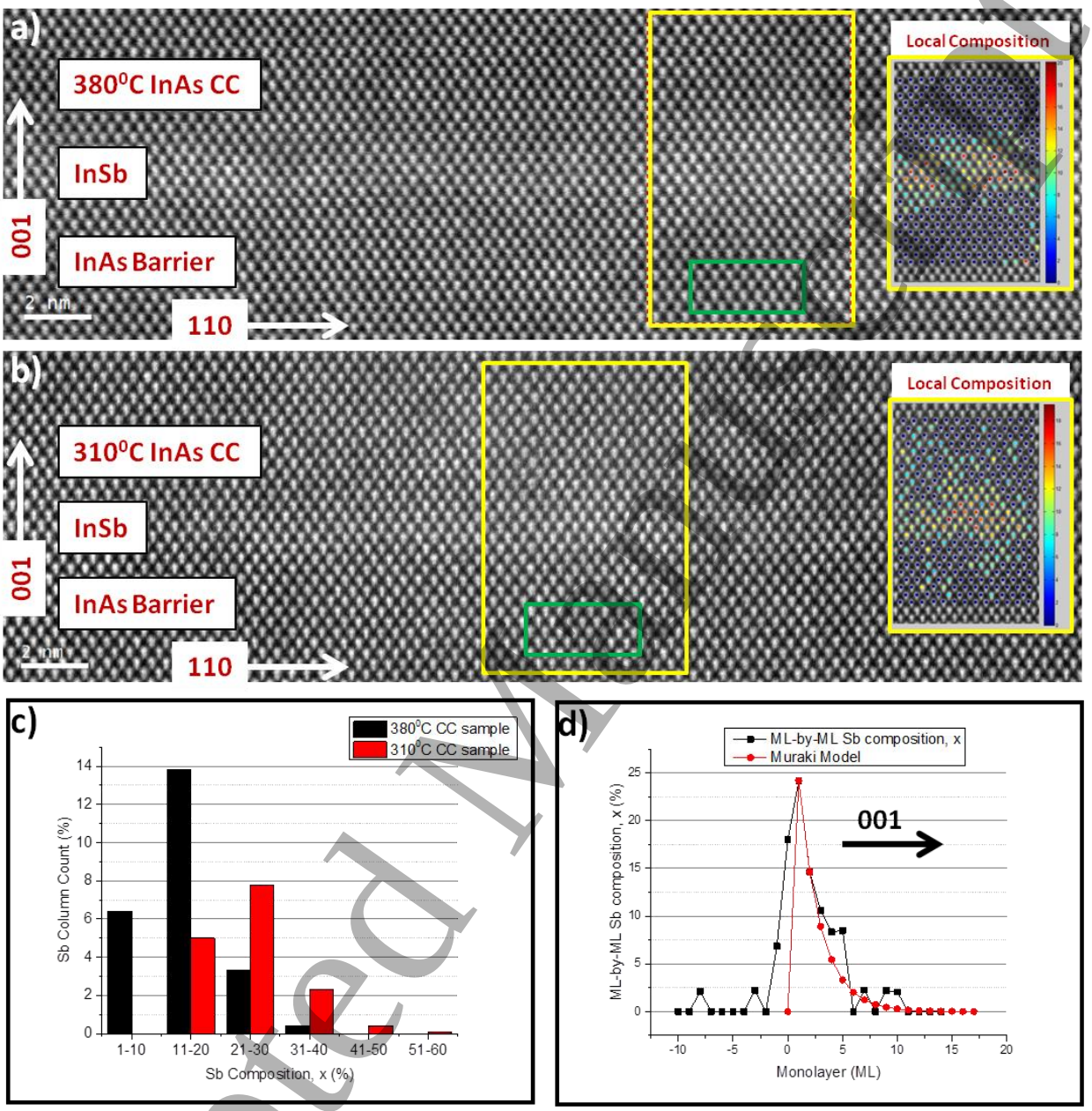

Figure 3: HAADF-(S)TEM images of single InAs/InSb/InAs layer associated with (a) 380ºC and (b) 310ºC InAs CC samples. The insets represent atomic column-by-column colored Sb composition maps (in %) generated within the respective yellow rectangles in those images. (c) A histogram exhibiting cumulative Sb atomic column counts (in %) for different Sb composition ranges in both CC samples. (d) ML-by-ML Sb average Sb composition (in black) along the [001] growth direction calculated from the Sb composition map in Figure 3b; the red curve represents the Muraki fit of the experimental data.

Conclusions

In summary, we have investigated the effect of including InAs CC grown at 380ºC and 310ºC in the SML deposition of InSb within InSb/InAs heterostructures grown by MEE. Our results by XRD and TEM have demonstrated that reducing the InAs cap growth temperature is an effective tool to increase the Sb

incorporation in SML InSb/InAs heterostructures during the epitaxial growth of the material. 002 DF images reveal random InSb agglomerates in the layers, that lead to a more continuous layer for the lower InAs CC growth temperature of 310ºC. The quantitative atomic column resolved HAADF-(S)TEM analysis reveals atomic columns with larger Sb composition when the InAs CC growth temperature is reduced. Our results show that the introduction of InAs CC is a plausible approach to control the Sb distribution by reducing As/Sb exchange and Sb evaporation in SML InSb/InAs heterostructures.

Acknowledgements

This work was supported by European Union (UE) (post graduate research on dilute metamorphic nanostructures and metamaterials in semiconductor photonics (PROMIS) Horizon 2020 initial training network (ITN) project with Grant agreement no. 641899), Spanish MINECO (projects TEC2014-53727-C2-2-R and TEC2017-86102-C2-2-R) and the Junta de Andalucía (PAI research groups TEP-946 INNANOMAT and TIC-145). Co-financing from UE-FEDER is also acknowledged.

ORCID iDs

A A Khan: 0000-0002-0322-5024
E Repiso: 0000-0003-1895-7444
M Herrera: 0000-0002-2325-5941
P Carrington: 0000-0003-2107-5602
M de la Mata: 0000-0002-1581-4838
J Pizarro: 0000-0002-4295-6743
A Krier: 0000-0003-4098-5206
S I Molina: 0000-0002-5221-2852

References:

1. Kim Y, Kim J O and Lee S J 2018 Submonolayer quantum dots for optoelectronic devices *J. Korean Phys. Soc.* **73** 833-40
2. Xu Z, Birkedal D, Hvam J M, Zhao Z, Liu Y, Yang K, Kanjilal A and Sadowsky J (2003) Structure and optical anisotropy of vertically correlated submonolayer InAs/GaAs quantum dots *Appl. Phys. Lett.* **82** 3859
3. Stranski I N and Krastanow L 1938 Zur Theorie der orientierten Ausscheidung von Ionenkristallen aufeinander Abhandlungen der Mathematisch-Naturwissenschaftlichen Klasse IIb. *Akademie der Wissenschaften Wien* **146** 797-810
4. Asahi H 1997 Self-organized quantum wires and dots in III-V semiconductors *Adv. Mat.* **9** 1019-1026
5. Ivanov S V, Semenov A N, Solov'ev V A, Lyublinskaya O G, Terent'ev Y V, Mel'tser B Y, Prokopova L G, Sitnikova A A, Usikova A A, Toropov A A and Kop'ev P S 2005 Molecular beam epitaxy of type II InSb/InAs nanostructures with InSb sub-monolayers *J. Cryst. Grwth.* **278** 72-77
6. Carrington P J, Solov'ev V A, Zhuang Q, Ivanov S V and Krier A 2008 Type II InSb/InAs quantum dot structures grown by molecular beam epitaxy using Sb_2 and As_2 fluxes *Proc. of SPIE* **6900:** Quant. Sens. Nanophot. Dev. V 6900I
7. Solov'ev V A, Lyublinskaya O G, Semenov A N, Mel'tser B Y, Solnyshkov D D, Terent'ev Y V, Prokopova L A, Toropov A A, Ivanov S V and Kop'ev P S 2005 Room-temperature 3.9-4.3 μm

photoluminescence from InSb submonolayers grown by molecular beam epitaxy in an InAs matrix *Appl. Phys. Lett.* **86** 011109

8. Solov'ev V A, Sedova I V, Lyublinskaya O G, Semenov A N, Mel'tser B Y, Sorokin S V, Terent'ev Y V and Ivanov S V 2005 Midinfrared injection-pumped laser based on a III-V/II-VI hybrid heterostructure with submonolayer InSb insets *Tech. Phys. Lett.* **31** 235-37
9. Lyublinskaya O G, Solov'ev V A, Semenov A N, Mel'tser B Y, Terent'ev Y V, Prokopova L A, Toropov A A, Sitnikova A A, Rykhova O V and Ivanov S V 2006 Temperature-dependent photoluminescence from type-II InSb/InAs quantum dots *J. Appl. Phys.* **99** 093517
10. Mikhrin S S, Zhukov A E, Kovsh A R, Maleev N A, Ustinov V M, Shernyakov Y M, Soshnikov I P, Livshits D A, Tarasov I S, Bedarev D A, Volovik B V, Maximov M V, Tsatsul'nikov A F, Ledentsov N N, Kop'ev P S, Bimberg D and Alferov Z I 2000 0.94 μm diode lasers base on Stranski-Krastanow and sub-monolayer quantum dots *Semicond. Sci. Technol.* **15** 1061-64
11. Kim J O, Sengupta S, Barve A V, Sharma Y D and Adhikary S 2013 Multi-stack InAs/InGaAs sub-monolayer quantum dots infrared photodetectors *Appl. Phys. Lett.* **102** 011131
12. Hopfer F, Mutig A, Fiol G, Kuntz M, Shchukin V A, Haisler V A, Warming T, Stock E, Mikhrin S S, Krestnikov I L, Livshits D A, Kovsh A R, Bornholdt C, Lenz A, Eiesel H, Dähne M, Ledentsov N N and Bimberg D 2007 20 Gb/s 85^0C error-free operation of VCSELs based on submonolayer deposition of quantum dots *IEEE J. Top. Quant. Elect.* **13** 1302-08
13. Cirlin G, Petrov V and Dubrovskii V 1997 Direct formation of InGaAs/GaAs quantum dots during submonolayer epitaxies from molecular beams *Czech. J. Phys.* **47** 379-84
14. Horikoshi Y, Kawashima M and Yamaguchi H 1986 Low-temperature growth of GaAs and AlAs-GaAs quantum well layers by modified molecular beam epitaxy *Jap. J. Appl. Phys.* **25** L868-70
15. Germann T D, Strittmatter A, Pohl J, Pohl U W, Bimberg D, Rautiainen J, Guina M and Okhotnikov O G 2008 High-power semiconductor disk laser based on InAs/GaAs submonolayer quantum dots *Appl. Phys. Lett.* **92** 101123
16. Bressler-Hill V, Lorke A, Varma S, Petroff P M, Pond K and Weinberg W H 1994 Initial stages of InAs epitaxy on vicinal GaAs(001)-(2X4) *Phys. Rev. B* **50** 8479-87
17. Hopfer F, Mutig A, Kuntz M, Fiol G, Bimberg D, Ledentsov N N, Shchukin V A, Mikhrin S S, Livshits D L, Krestnikov I L, Kovsh A R, Zakharov N D and Werner P 2006 Single-mode submonolayer quantum-dot-vertical-cavity surface-emitting lasers with high modulation bandwidth *Appl. Phys. Lett.* **89** 141106
18. Sengupta S, Kim J O, Barve A V, Adhikary S, Sharma Y D, Gautam N, Lee S J, Noh S K, Chakrabarti S and Krishna S 2012 Sub-monolayer quantum dots in confinement enhanced dots-in-a-well heterostructure *Appl. Phys. Lett.* **100** 191111
19. Lam P, Wu J, Tang M, Jiang Q, Hatch S, Beanland R, Wilson J, Allison R and Liu H 2014 Submonolayer InGaAs/GaAs quantum dot solar cells *Sol. Ener. Mat. Sol. Cell* **126** 83-87
20. Carrington P J, Solov'ev V A, Zhuang Q, Krier A and Ivanov S V 2008 Room temperature midinfrared electroluminescence from InSb/InAs quantum dot light emitting diodes *Appl. Phys. Lett.* **93** 091101
21. Khan A A, Herrera M, Fernández-Delgado N, Reyes D F, Pizarro J, Repiso E, Krier A, Molina S I 2019 Investigation on Sb distribution for InSb/InAs sub-monolayer heterostructure using TEM techniques *Nanotech.* **31** 025706

22. Haugan H J, Brown G J and Peoples J A 2017 On the study of Sb incorporation in InAs/InAsSb superlattices for infrared sensing *J. Vac. Sci. Technol. B* **35** 02B107
23. Timm R, Lenz A, Eisele H, Ivanova L, Dähne M, Balakrishnan G, Huffaker D L, Farrer I and Ritchie D A 2008 Quantum ring formation and antimony segregation in GaSb/GaAs nanostructures *J. Vac. Sci. Technol. B* **26** 1492-1503
24. Hodgson P D, Bentley M, Delli E, Beanland R, Wagener M C, Botha J R and Carrington P J 2018 Optical and structural properties of InGaSb/GaAs quantum dots grown by molecular beam epitaxy *Semicond. Sci. Technol.* **33** 125021
25. Zhuang Q, Carrington P J and Krier A 2008 Growth optimization of self-organized InSb/InAs quantum dots *J. Phys. D: Appl. Phys.* **41** 232003
26. Malis T, Cheng S C and Egerton R F 1988 EELS log-ratio technique for specimen-thickness measurement in the TEM *J. Elect. Microsc. Tech.* **8** 193-200
27. Semenov A, Lyublinskaya O G, Solov'ev V A, Mel'tser B Y and Ivanov S V 2007 Surface segregation of Sb atoms during molecular-beam epitaxy of InSb quantum dots in an In(As)Sb matrix *J. Cryst. Grwth.* **301-302** 58-61
28. Ripalda J M, Alonso-Álvarez D, Alén B, Taboada A G, García J M, González Y and González L 2007 Enhancement of the room temperature luminescence of InAs quantum dots by GaSb capping *Appl. Phys. Lett.* **91** 012111
29. Guimard D, Tsukamoto S, Nishioka M and Arakawa Y 2006 1.55 μm emission from InAs/GaAs quantum dots by metal organic chemical vapor deposition via antimony incorporation *Appl. Phys. Lett.* **89** 083116
30. Fewster P F 1993 X-ray diffraction from low-dimensional structures *Semicond. Sci. Technol.* **8** 1915-34
31. Shen X-M, Li H, Liu S, Smith D J and Zhang Y-H 2013 Study of InAs/InAsSb type-II superlattices using high-resolution x-ray diffraction and cross-sectional electron microscopy *J. Cryst. Grwth.* **381** 1-5
32. Ngo C Y, Yoon S F, Fan W J and Chua S J 2006 Effects of size and shape on electronic states of quantum dots *Phys. Rev. B* **74** 245331
33. Jones L 2016 Quantitative ADF STEM: acquisition, analysis and interpretation *IOP Conf. Ser.: Mat. Sci. Engg.* **109** 012008
34. Molina S I, Sales D L, Galindo P L, Fuster D, González Y, Alén B, González L, Varela M and Pennycook S J 2009 Column-by-column compositional mapping by Z-contrast imaging *Ultramic.* **109** 172-76
35. Hernández-Maldonado D, Herrera M, Alonso-González P, González Y, González L, Gazquez J, Varela M, Pennycook S J, Guerrero-Lebrero M P, Pizarro J, Galindo P L and Molina S I 2011 Compositional analysis with atomic column spatial resolution by 5th-order aberration-corrected scanning transmission electron microscopy *Microsc. & Microanal.* **17** 578-81
36. Khan A A, Herrera M, Pizarro J, Galindo P L, Carrington P J, Fujita H, Krier A and Molina S I 2019 Modified qHAADF method for atomic column-by-column compositional quantification of semiconductor heterostructures *J. Mater. Sci.* **54** 3230-41
37. Muraki K, Fukatsu S, Shiraki Y and Ito R 1992 Surface segregation of In atoms during molecular beam epitaxy and its influence on the energy levels in InGaAs/GaAs quantum wells *Appl. Phys. Lett.* **61** 557-59

38. Lu J, Luna E, Aoki T, Steenbergen E H, Zhang Y H and Smith D J 2016 Evaluation of antimony segregation in InAs/InAs1-xSbx type-II superlattices grown by molecular beam epitaxy *J. Appl. Phys.* **119** 095702
39. Steinshnider J, Harper J, Weimer M, Lin C H, Pei S S and Chow D H 2000 Origin of antimony segregation in GaInSb/InAs strained-layer superlattices *Phys. Rev. Lett.* **85** 4562-65
40. Bennett B R, Shanabrook B V and Twigg M E 1999 Anion control in molecular beam epitaxy of mixed As/Sb III-V heterostructures *J. Appl. Phys.* **85** 2157-61
41. Hatami F, Ledentsov N N, Grundmann M, Böhrer J, Heinrichsdorff F, Beer M, Bimberg D, Ruvimov S S, Werner P, Gösele U, Heydenreich J, Richter U, Ivanov S V, Meltser B Y, Kop'ev P S and Alferov Z I 1995 Radiative recombination in type-II GaSb/GaAs quantum dots *Appl. Phys. Lett.* **67** 656-58
42. Xie Q, Nostrand J E V, Brown J L and Stutz C E 1999 Arsenic for antimony exchange on GaSb, its impact on surface morphology, and interface structure *J. Appl. Phys.* **86** 329-37
43. Nosho B Z, Bennett B R, Whitman L J and Goldenberg M 2001 Effects of As2 versus As4 on InAs/GaSb heterostructures: As-for-Sb exchange and film stability *J. Vac. Sci. Technol. B* **19** 1626-30
44. Brown T, Brown A and May G 2002 Anion exchange at the interfaces of mixed anion III-V heterostructures grown by molecular beam epitaxy *J. Vac. Sci. Technol. B* 20 1771-76
45. Ye H, Li L, Hinkey R T, Yang R Q, Mishima T D, Keay J C, Santos M B and Johnson M B 2013 MBE growth optimization on InAs (001) homoepitaxy *J. Vac. Sci. Technol. B* **31** 03C135